On Coherent Structures, Flow-Induced Vibrations, and Migratory Flow In Liquid Metal Nuclear Reactors

Bertocchi, Fulvio

DOI
10.4233/uuid:337bec74-ac1d-4142-b8f2-a2281175c2d4

Publication date
2020

Document Version
Final published version

BERTOCCHI ON COHERENT STRUCTURES, FLOW-INDUCED VIBRATIONS, AND MIGRATORY FLOW

ON COHERENT STRUCTURES, FLOW-INDUCED VIBRATIONS, AND MIGRATORY FLOW

in Liquid Metal Nuclear Reactors

FULVIO BERTOCCHI

With this you are warmly invited to attend the defence of my thesis with title

On
Coherent Structures, Flow-Induced Vibrations, and Migratory Flow

in Liquid Metal Nuclear Reactors

27 January 2020
at 12:30 in the Senatzaal of the TU Delft, Mekelweg 5, Delft.

I will give a presentation before the defence at 12:00.

Fulvio Bertocchi

Propositions

accompanying the dissertation

ON COHERENT STRUCTURES, FLOW-INDUCED VIBRATIONS, AND MIGRATORY FLOW

IN LIQUID METAL NUCLEAR REACTORS

by

Fulvio BERTOCCHI

1. A high speed camera provides the best compromise between accuracy and handiness to measure the frequency of vibration in a rod bundle. (This thesis, Chapter 4)
2. A 7-rod bundle is more difficult to build than larger ones. (This thesis)
3. Calculating the transversal pressure gradient with Equation 5.39 of this thesis is easier than with the Euler equation. (This thesis, Chapter 5)
4. If ionizing radiation would be visible to the naked eye, nuclear energy would be more acceptable to the public.[1]
5. Starting the PhD with a thorough time planning weakens the ability of the student to tackle unexpected setbacks.
6. Financial support to poor African countries will increase migration across the Mediterranean Sea.[2]
7. If one does not appreciate theatre, he/she cannot truly enjoy Caravaggio's art.
8. In cage diving with white sharks, the cage protects the shark from humans, more than the other way around.
9. A good scientist must also be a good reader.
10. A stress reduction course for PhDs should also cover vacation time.

These propositions are regarded as opposable and defendable, and have been approved as such by promotors prof. dr. ir. J. L. Kloosterman and dr. ir. M. Rohde.

[1] *The Psychology of Risk perception*, Harvard Health Publishing, 2011.

[2] M. A. Clemens and H. M. Postel, *Deterring Emigration with Foreign Aid: An Overview of Evidence from Low-Income Countries*, Center for Global Development, 2018.

Stellingen

behorende bij het proefschrift

ON COHERENT STRUCTURES, FLOW-INDUCED VIBRATIONS, AND MIGRATORY FLOW

IN LIQUID METAL NUCLEAR REACTORS

door

Fulvio BERTOCCHI

1. Een hoge-snelheidscamera geeft het beste compromis tussen precisie en gebruiksgemak bij het meten van de vibratiefrequentie in staafbundels.
(Dit proefschrift, Hoofdstuk 4)

2. Een bundel met 7 staven is moeilijker te bouwen dan grotere. (Dit proefschrift)

3. De berekening van de overdwarse drukgradiënt is makkelijker met vergelijking 5.39 in dit proefschrift dan met de Euler vergelijking.
(Dit proefschrift, Hoofdstuk 5)

4. Als ioniserende straling met het blote oog zichtbaar zou zijn, zou kernenergie acceptabeler zijn voor het publiek.[1]

5. De start van een promotietraject met een gedegen tijdsplanning verzwakt het vermogen van de promovendus om met onverwachte tegenslagen om te gaan.

6. Financiële ondersteuning van arme Afrikaanse landen zal leiden tot een toename van migratie over de Middellandse zee.[2]

7. Wie niet van theater houdt, kan niet waarlijk genieten van Caravaggio's kunst.

8. Tijdens kooiduiken met witte haaien beschermt de kooi de haai meer tegen de mens dan andersom.

9. Een goede wetenschapper moet ook een goede lezer zijn.

10. Een cursus stressreductie voor promovendi moet ook de vakantietijd omvatten.

Deze stellingen worden opponeerbaar en verdedigbaar geacht en zijn als zodanig goedgekeurd door de promotoren prof. dr. ir. J. L. Kloosterman en dr. ir. M. Rohde.

[1] *The Psychology of Risk perception*, Harvard Health Publishing, 2011.
[2] M. A. Clemens and H. M. Postel, *Deterring Emigration with Foreign Aid: An Overview of Evidence from Low-Income Countries*, Center for Global Development, 2018.

On Coherent Structures, Flow-Induced Vibrations, and Migratory Flow

in Liquid Metal Nuclear Reactors

On Coherent Structures, Flow-Induced Vibrations, and Migratory Flow

in Liquid Metal Nuclear Reactors

Proefschrift

ter verkrijging van de graad van doctor

aan de Technische Universiteit Delft,

op gezag van de Rector Magnificus Prof. dr. ir. T. H. J. J. van der Hagen,

voorzitter van het College voor Promoties,

in het openbaar te verdedigen op 27 januari om 12:30 uur

door

Fulvio BERTOCCHI

Master of Science in Nuclear Engineering

University of Pisa

geboren te Pisa, Italië

Dit proefschrift is goedgekeurd door de promotoren:
Prof. dr. ir. J. L. Kloosterman
Dr. ir. M. Rohde

Samenstelling promotiecommissie:

Rector Magnificus	voorzitter
Prof. dr. ir. J. L. Kloosterman,	Delft University of Technology, promotor
Dr. ir. M. Rohde,	Delft University of Technology, promotor
Onafhankelijke leden:	
Prof. H. Anglart	Royal Institute of Technology, Stockholm
Prof. dr. H. Clercx	Eindhoven University of Technology
Prof. dr. ir. B. J. Boersma	Delft University of Technology
Prof. dr. F. Scarano	Delft University of Technology
Prof. dr. D. J. E. M. Roekaerts	Delft University of Technology, reservelid
Overig lid:	
Dr. ir. J. Degroote	Ghent University, België

ISBN

Keywords:
Cross-flow, Coherent structures, Fluid-Structure Interactions, Hexagonal bundle, Wire wrapped, Laser Doppler Anemometry, Particle Image Velocimetry

This research was performed in the Reactor Physics and Nuclear Materials (RPNM) section of the Department of Radiation, Science and Technology (RST) of Delft University of Technology (The Netherlands).

Financial support
This project has received funding from the Euratom research and training programme 2014 – 2018 under the grant agreement No. 654935.

"Those who have handled sciences have been
either men of experiment or men of dogmas.
The men of experiment are like the ant,
they only collect and use;
the reasoners resemble spiders,
who make cobwebs out of their own substance.
But the bee takes a middle course:
it gathers its material
from the flowers of the garden and of the field,
but transforms and digests it by a power of its own."

FRANCIS BACON, 1620

Summary

Flows in rod bundles are common to many industrial applications such as heat exchangers or some types of nuclear reactors. The core of many classes of nuclear reactors can be easily sketched as a bundle of rods, the fuel pins, inmmersed in an axial flow of coolant that removes the heat produced by the fission reaction. Coupling this geometry to an axial flow can trigger periodical vortices, known as large coherent structures or gap vortex streets, that move on both sides of the gaps between the rods. By crossing the gap (cross-flow), these vortices may enhance the heat removal mechanism, thus improving the performance of the reactor.
However, coherent structures cause velocity oscillations in the flow that may induce vibrations of the fuel rods, leading to their long term damage. The length (or wavelength) of coherent structures is a key parameter for understanding the interplay between these vortices and the vibrations that may be triggered on the rods. Their wavelength determines the frequency of the velocity oscillations in the fluid, hence of the external force imposed on the rods.

One of the reactor designs belonging to the next generation (Gen-IV) of nuclear reactors is the Liquid Metal Fast Breeder Reactor (LMFBR). This reactor has the fuel rods in the core arranged in a hexagonal matrix. In this design, a wire is helicoidally wrapped around each fuel rod to keep them separated from each other. The presence of the wire diverts part of the more turbulent flow from the bulk towards the gap between the rods, where the flow would be otherwise less turbulent. This enhances the heat exchange and avoids hot spots on the fuel cladding.
A phenomenon known as migratory flow has been observed in rod bundles with wire spacers. In the presence of migratory flow, the fluid is diverted from the gap towards the main subchannel and it bends against the helicoid path of the wire, thus leading to a very complex flow, where part of the fluid follows the wire direction and part moves against it, away from the gap. Although this behaviour was first observed years ago, the governing mechanism is not clear yet. Explaining migratory flow is thus a fundamental step towards a general understanding of the mixing and mass transfer phenomena in rod bundles in the presence of helicoid wires.

This research considers several aspects of the flow inside rod bundle geometries. The aim is to study coherent structures to understand their role in inducing vi-

brations of the rods, and to provide a model that explains migratory flow caused by helicoid wire spacers.

To these purposes, three experimental facilities are designed and built that work in isothermal conditions, ambient pressure and with water as working fluid. The first is a rectangular channel hosting two half-rods whose distance can be adjusted. A second hexagonal bundle containing seven rods has the central rod made of flexible silicone to study vibrations induced by the flow. The third facility is a hexagonal bundle with seven rods, each of them equipped with a wire helicoidally wound around them in order to measure and explain migratory flow.
The measurements are carried out with non intrusive optical systems. Laser Doppler Anemometry (LDA) is used to measure the flow components in the rectangular channel with half-rods and in the hexagonal bundle without wire spacers. For the latter, a high speed camera is also used to measure the amplitude and frequency of the vibrations induced on the flexible rod by the flow. In the hexagonal bundle hosting wire spacers, planar (i.e. two dimensional) Particle Image Velocimetry (PIV) is used to measure the flow near to the wire of the central rod of the bundle. For all the three experiments, optical access is achieved by replacing part of the material of the rods with Fluorinated Ethylene Propylene (FEP), a Refractive Index-Matching (RIM) polymer that nearly matches the refractive index of plain water. In this way, optical distortion of the light rays is greatly reduced.

The measurements of the flow inside the channel hosting two half-rods show that cross-flow of coherent structures across the gap decreases in frequency if the distance between the rods is increased.
This research shows that the wavelength of coherent structures becomes independent of the flow rate above a certain value of the Reynolds number, and that it is affected solely by the geometry of the channel. Performing dimensional analysis of the problem, and supporting the reasoning with experimental evidence, has increased our understanding of what determines the length of the structures. This appears to be a function of only the hydraulic diameter of the gap region close to which they form. This finding is presented in the form of a novel correlation that predicts the length of coherent structures. This correlation is applicable to a number of different geometries, ranging from channels with few rods to full rod bundles.

The flow measurements in the hexagonal bundle (without wire spacers) show that the frequency of passage of coherent structures in the axial direction increases with the Reynolds number. If this frequency becomes equal to twice the first natural frequency of rod, a drastic increase in the amplitude of oscillation is observed, which can be ascribed to the synchronization between the rod and coherent structures carried by the flow.

It is experimentally shown that for hexagonal rod bundles with helicoid wires, the flow very close to the rod follows the helicoid path of the wire.

However, if the measurement region is shifted closer to the main subchannel surrounding the rod, the flow bends towards the wire, against the helicoid path, suggesting the presence of migratory flow. A model to reconstruct the pressure gradient caused by the wire, and responsible for the bending of the flow, is derived from the steady-state, two-dimensional, inviscid Navier-Stokes equations applied to the flow streamlines. Following a theoretical approach, an equation is derived from this model to estimate the bending angle of the flow at any point inside the measured area, based on the time-averaged flow fields. This equation has the form of an integral evaluated along the path followed by a streamline. It shows how the bending of a streamline at an arbitrary point is the result of the interaction between the transversal pressure gradient, trying to bend the fluid, and the inertial forces, trying to straighten it towards the direction of the main flow.
A possible correlation for estimating the bending angle of the flow is obtained with dimensional analysis and with the support of the experimental results. Contrarily to the theoretical model, this correlation relies on macroscopic variables, being the bundle dimensions and the geometry of the subchannel.
Finally, this thesis suggests possible topics of interest for future research.

Samenvatting

Stroming en warmteoverdracht langs bundels van buizen komt veel voor in industriële toepassingen zoals warmtewisselaars en kernreactoren. De kern van de meeste kernreactoren kan eenvoudig beschreven worden als een bundel brandstofstaven die ondergedompeld is in een axiale stroom koelmiddel. De bedoeling is om op deze manier de warmte te verwijderen die wordt geproduceerd door de splijtingsreacties in de reactorkern. Een axiale stroom in een dergelijke bundel van brandstofstaven kan periodieke wervelingen veroorzaken, bekend als "grote coherente structuren", die aan beide zijden van de spleet tussen de brandstofstaven bewegen. Deze wervelingen verbeteren de koeling van de reactorkern, waardoor de prestaties van de reactor worden verbeterd. De coherente structuren veroorzaken snelheidsschommelingen die op hun beurt trillingen van de brandstofstaven kunnen veroorzaken. Degelijke trillingen kan leiden tot schade op de lange termijn. De lengte (of golflengte) van coherente structuren is een belangrijke parameter voor het begrijpen van de wisselwerking tussen deze wervelingen en de trillingen van de brandstofstaven. De golflengte van de coherente structuren bepaalt namelijk de frequentie van de snelheidsschommelingen in de vloeistof, en daarmee de frequentie en kracht die op de staven wordt uitgeoefend.

Eén van de reactorontwerpen van de volgende generatie (Gen-IV) van kernreactoren is de Liquid Metal Cooled Fast Breeder Reactor (LMFBR). Deze reactor heeft de brandstofstaven in de kern gerangschikt in een hexagonale matrix. In dit ontwerp is een draad als een helix rond elke brandstofstaaf gewikkeld om ze van elkaar gescheiden te houden. De aanwezigheid van deze zogenaamde "spacer" leidt een deel van de turbulente stroming in de bulk naar de nauwe opening tussen de staven, waardoor op deze plek een betere warmteoverdracht plaatsvindt en waardoor hotspots in deze opening vermeden kunnen worden. Een fenomeen dat bekend staat als migratiestroom is waargenomen in reactorbundels waar dergelijke helixvormige draden aangebracht zijn. Door deze migratiestroom wordt de vloeistof vlakbij het oppervlak van de brandstofstaaf van de opening naar de bulkstroming geleid, maar buigt deze vlak boven de draad in tegen de richting van de draad. Hoewel dit gedrag jaren geleden al werd waargenomen, is het mechanisme achter deze complexe stroming nog niet goed bekend. Het verklaren van deze migratiestromen is daarom een belangrijke stap op weg naar een beter begrip van de warmte- en stofoverdracht in staafbundels waarbij helixvormige spacers worden gebruikt.

In dit onderzoek worden beide bovengenoemde aspecten bestudeerd. Het doel is om de invloed van coherente structuren op het trillen van de brandstofstaven én de migratiestroom veroorzaakt door de helixvormige spacers beter te begrijpen.

Ten behoeve van deze doeleinden zijn drie experimentele faciliteiten ontworpen en gebouwd die werken onder isotherme omstandigheden, bij omgevingsdruk en met water als vloeistof. De eerste faciliteit bestaat uit een rechthoekig kanaal met twee halve staven waarvan de onderlinge afstand kan worden aangepast. De tweede faciliteit is een zeshoekige bundel met zeven staven waarvan de centrale staaf van flexibel siliconenmateriaal is gemaakt om de trillingen te kunnen bestuderen die worden veroorzaakt door de stroming. De derde faciliteit bestaat uit een zeshoekige bundel met zeven staven, elk uitgerust met een helixvormige spacer om de migratiestroom te kunnen bestuderen. De metingen van het snelheidsveld worden uitgevoerd met niet-intrusieve optische systemen. Laser Doppler-anemometrie (LDA) wordt gebruikt om de snelheidscomponenten in het rechthoekige kanaal met halve staven en in de zeshoekige bundel zonder spacers te meten. In deze zeshoekige bundel wordt tevens een hogesnelheidscamera gebruikt om de amplitude en frequentie van de trillingen te kunnen meten die door de stroming op de flexibele staaf worden uitgeoefend. In de hexagonale bundel met spacers wordt planar (d.w.z. tweedimensionale) Particle Image Velocimetry (PIV) gebruikt om de snelheidscomponenten nabij de spacer van de centrale staaf van de bundel te meten. Voor alle drie de experimenten wordt optische toegang verkregen door een deel van het materiaal van de staven te vervangen door Fluorinated Ethylene Propylene (FEP). FEP is een brekingsindex-matching (RIM) polymeer dat een brekingsindex heeft die bijna overeenkomt met die van gewoon water. Op deze manier worden optische vervormingen sterk verminderd.

De metingen van de stroming in het kanaal met twee halve staven tonen aan dat de frequentie van dwarsstroming (“cross flow”) door de coherente structuren afneemt als de afstand tussen de staven wordt vergroot. Dit onderzoek toont aan dat de golflengte van coherente structuren onafhankelijk wordt van de stroomsnelheid boven een bepaalde waarde van het Reynoldsgetal, en dat deze alleen wordt beïnvloed door de geometrie van het kanaal. Het uitvoeren van een dimensieanalyse van het probleem, welke ondersteund is door experimentele gegevens, heeft het begrip van wat de lengte van de structuren bepaalt vergroot. Deze lengte lijkt namelijk alleen een functie te zijn van de hydraulische diameter van de spleet tussen de staven. Deze bevinding kan worden beschreven in de vorm van een nieuwe correlatie die de lengte van coherente structuren voorspelt. Deze correlatie is van toepassing op een aantal verschillende geometrieën, variërend van kanalen met weinig staven tot volledige staafbundels.

De metingen in de zeshoekige bundel (zonder spacers) laten zien dat de frequentie van coherente structuren in de axiale richting toeneemt met het Reynoldsgetal. Als deze frequentie gelijk wordt aan tweemaal de natuurlijke frequentie van staaf, wordt een drastische toename in de amplitude van de trillingen waargenomen.

Deze toename kan worden toegeschreven aan de synchronisatie tussen de staaf en coherente structuren.

Het is experimenteel aangetoond dat voor hexagonale staafbundels met helixvormige spacers de stroming dichtbij de staaf het helixvormige pad van de spacer volgt. Verder weg van de staaf buigt de stroom tegen de richting in van de spacer, hetgeen de aanwezigheid van migratiestroom aantoont. Een model voor de door de draad veroorzaakte drukgradiënt, die verantwoordelijk is voor het buigen van de stroom, is afgeleid uit de tweedimensionale, stationaire Euler-vergelijkingen die op de stroomlijnen worden toegepast. Vervolgens is uit dit model een vergelijking afgeleid om de buigingshoek van de stroming op elk punt in het gemeten gebied te kunnen schatten. Deze vergelijking heeft de vorm van een integraal langs een stroomlijn en laat zien hoe het buigen van een stroomlijn op een willekeurig punt het resultaat is van de interactie tussen de transversale drukgradiënt, verantwoordelijk voor het ombuigen van de stroming, en de traagheidskrachten. Een correlatie voor het schatten van de buigingshoek van de stroming kan worden verkregen door middel van dimensieanalyse en experimentele resultaten. In tegenstelling tot het theoretische model berust deze correlatie op macroscopische variabelen, zijnde de bundeldimensies en de geometrie van het subkanaal.
Ten slotte worden in dit proefschrift mogelijke onderwerpen gesuggereerd die van belang kunnen zijn voor toekomstig onderzoek.

(Dutch translation provided by Martin Rohde.)

Table of Contents

Chapter 1

Introduction

1.1 Motivation of this research

As a result of the development of the developing countries, and the associated growth of the population, the electricity demand is expected to increase drastically in the next decades. The projections [1] of the International Atomic Energy Agency (IAEA) foresee an increase of the worldwide capacity of nuclear-generated electricity by 42% (reaching $554\,\mathrm{GW_e}$) within 2030, and doubling the actual capacity by 2050. However, relying on more conservative projections, the capacity might remain constant at nowadays' levels. There is a big deal of uncertainty in the figures because it is yet not clear whether the nuclear power plants scheduled for decommissioning are going to be replaced by new nuclear capacity.
With the goal of pursuing safer and more sustainable nuclear energy, in the year 2000, the Generation IV International Forum identified six innovative designs of nuclear reactors planned to be commercially available by 2040. These reactors feature larger safety margins, pose an obstacle to nuclear proliferation, or are capable of using nuclear waste generated by conventional reactors as fuel. This generation of reactors could, thus, be part of a structured and long-term strategy for reducing emissions, which is currently a rather far-fetched vision in Europe [3, 4]. The underlying goal is to keep the average global temperature increase below the value agreed at the Paris Agreement of $2\,^{\circ}\mathrm{C}$.
One of the proposed designs is the Liquid Metal Fast Breeder Reactor (LMFBR). The heat removed by the coolant, being sodium, lead, or an eutectic mixture of lead and bismuth (LBE) converts water into steam that, in turn, generates electricity through a spinning turbine (Figure 1.1). The core of a LMFBR typically contains a large number of fuel assemblies, each consisting of a bundle of rods hosting the fuel (fuel pins) arranged in a hexagonal lattice through which the liquid metal coolant flows, parallel to the fuel pins (Figure 1.2a). The lattice is characterised by the P/D ratio (ratio between the pin pitch and pin diameter). Due to the tight assembly, one solution for keeping the rods from touching each other during normal operation is to wrap an helicoid wire spacer around each of them (Figure 1.2b). The coupling between an axial flow of fluid and such a geometry gives origin to a

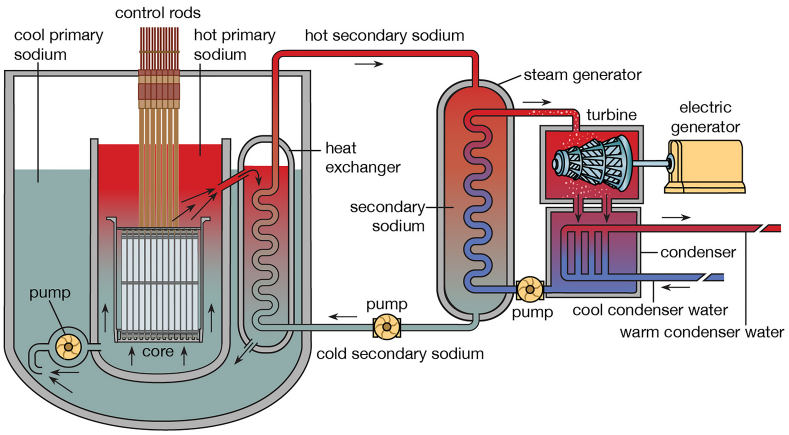

Figure 1.1: Schematic of the Liquid Metal Fast Breeder Reactor. Adopted from [2].

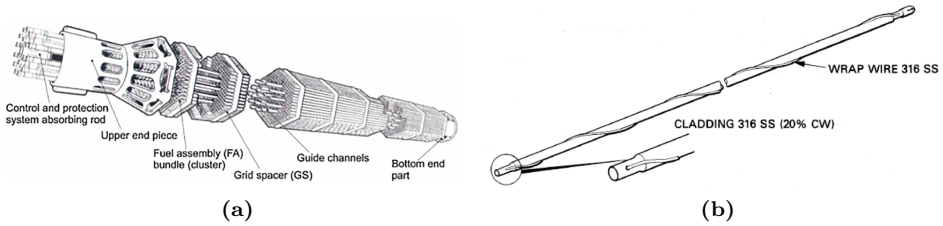

(a) **(b)**

Figure 1.2: a) Sketch of one of the many hexagonal fuel assemblies hosted inside the core. Adopted from [5]. b) Fuel rod with helicoid wrapped-wire. Public domain, US DOE.

number of phenomena that need to be studied for the sake of a safe operation of the reactor.

Streaks of relatively large periodical vortices may occur that, on one hand, are beneficial for the safe operation of the core because they can enhance the mixing, hence lowering the temperature of the fuel cladding. On the other hand, they can induce vibrations of the fuel rods leading to damage by fretting and, eventually, fatigue.

Moreover, the presence of the helicoid wire makes the flow even more complex to understand and to model due to the additional motion of fluid across the gaps between the rods.

This experimental work aims at studying large coherent structures and their role in inducing vibrations in rod bundles, as well as the effect of helicoid wires on the flow.

1.2 Vortex streets in a rod bundle geometry

Rod bundle flows occur in industrial applications, such as heat exchangers or LWR and Generation IV (Gen-IV) nuclear reactors. When geometries such as the core of a nuclear reactor are coupled with an axial flow we refer to it as rod bundle flow.
The presence of an axial flow leads to velocity differences between the low-speed region of the gap between two adjacent rods, and the high-speed region of the main sub-channels. This velocity difference produces a shear layer between the two flow regions, leading to streaks of vortices carried by the current. Generally these vortices (or flow structures) occur on both sides of the gap enclosed by two neighbouring rods, identifying the so-called *gap vortex streets* [6], also known as coherent structures. They look similar to the well-known Von Karman streets shedding in the wake of a bluff body in the presence of a transversal flow (Figure 1.3) immersed in a current of fluid.

Figure 1.3: Photograph of the Von Karman streets; the camera is moving with the main flow speed. Adopted from [7].

The mechanism responsible for their formation inside a rod bundle can be compared to the Kelvin-Helmholtz instability that occurs between two parallel layers of fluid moving with different speeds [8] (Figure 1.4).

Figure 1.4: Kelvin-Helmholtz instability arising from two layers of water with different velocities, being the upper one the fastest. Adopted from [7].

An inflection point in the stream-wise velocity profile is a necessary condition (although not sufficient) to have these coherent structures, as predicted by the Rayleigh's instability criterion [9]. Unlike free mixing layers, gap vortex streets are stable along the flow, hence the adjective *coherent*.
Research has widely covered the topic of coherent structures in rod bundles, both experimentally and numerically. Rowe measured coherent flow structures through

a gap where the P/D was adjustable to 1.125 and 1.250 [10]. Rehme investigated the axial flow of air inside a rectangular channel with four rods [11]. He detected coherent structures in the flow responsible for the lateral mass and momentum transfer across the subchannels that were affected by the P/D ratio. Rehme proposed a static pressure instability mechanism to account for the formation of these structures. Möller conducted experiments in a similar setup to study the formation of coherent structures [12]. Velocity and wall-pressure fluctuations were measured and coherent structures were found to occur near the gap between two rods. He adopted the term *metastable equilibrium* to describe the instantaneous velocity and vorticity difference caused by these structures. Möller also pointed out that vibrations of the fuel elements might occur if the natural frequency of the pins is close to the oscillating pressure field's frequency due to the periodic structures in the flow. Later, Choueiri and Tavoularis made use of flow visualization techniques: the structures formed near to the gap region and the boundary between the low-speed and high-speed fluid oscillated as they moved downstream [13].

A lateral (span-wise) movement of coherent structures across the gap between the rods may also occur, which is often referred to as cross-flow. In a nuclear reactor, cross-flow is the mechanism responsible of enhancing the lateral mixing between subchannels, decreasing the temperature on the fuel rod's outer cladding, and improving the overall safety of the plant. Gosset [14] and Piot [15] investigated such lateral mass transfer across an eccentric annular gap with flow visualization techniques. The instability mechanism responsible for cross-flow was found to be dependent on a critical Reynolds number, strongly affected by the geometry of the gap. Baratto investigated the air flow inside a 5-rod model of a CANDU (CANadian Deuterium Uranium) fuel assembly [16] finding that the frequency of passage of the coherent structures decreases with the gap size, along the circumferential direction around the rod.

Mahmood studied coherent structures and the inter-channel mixing in a square rod bundle over a range of Reynolds numbers [17]. One of his main findings was that the length (or wavelength) of coherent structures does not depend on the Reynolds number for values higher than 2000. The wavelength is affected merely by the geometry of the channel. These findings were consistent with those of Meyer [18] and Guellouz [19]. Later, Choueiri and Tavoularis studied the flow instability through the gap of an eccentric rod inside a circular channel [13, 20]. They found that the velocity fluctuations along the span-wise direction in the centre of the gap were varying in time with a rate twice as low compared to those in the axial direction. This was consistent with the model previously proposed by Meyer [18] of coherent structures regarded as counter-rotating vortices on either side of a gap.

Parallel numerical efforts have been made by Chang and Tavoularis with Unsteady Reynolds-averaged Navier Stokes (URANS) [21] and by Merzari and Ninokata with Large Eddy Simulations (LES) [22] to reproduce the complex flow inside such a geometry. However, the effects that gap geometry, in particular the P/D ratio, has on cross-flow has been debated long since and yet, a generally accepted conclusion is still seeked.

1.3 Fluid-structure interaction

An axial flow inside a rod bundle (typical of a nuclear reactor's core) induces oscillations of the rods due to the action of turbulence. This type of Fluid-Structure Interaction (FSI) is known as flow-induced vibration (FIV) and can be further classified in instability-induced excitations (IIE) or extraneously-induced excitations (EIE), following the Naudascher & Rockwell classification [23]. EIE are caused by pressure or velocity fluctuations in the main flow (not caused by movements of components of the bundle or by flow instabilities). Instability-induced excitations are due to local flow instabilities such as vortex shedding in the wake of a cylinder. There is also a third category termed movement-induced excitations (MIE) caused by the movement of the object itself, which drives the phenomenon (i.e. the fluttering wing of an airplane). Obviously the border between the three classes is not strict, especially between EIE and IIE, since these categories share some common aspects [24].
In order to summarise the behaviour of the rods in the presence of an axial flow, the description provided by De Ridder *et al.* may help [25]. It describes the case of a solitary cylinder placed inside an outer cylindrical channel. For very low flow velocities, the rod stays in the center of the channel. As the velocity increases, the rod exhibits small oscillations induced by the turbulent flow. When the velocity

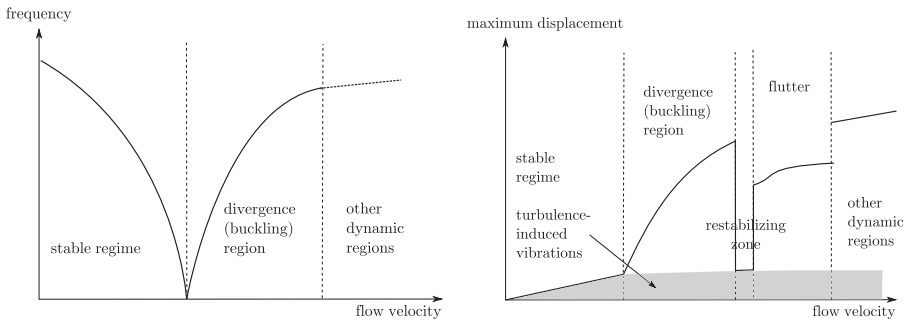

Figure 1.5: Natural frequency and maximum displacement of a rod inside a concentric channel depending on the flow speed. Adopted from [25].

is increased, the amplitude will also increase and, at a specific *critical* velocity, the rod will buckle to one side. Simultaneously, its natural frequency will drop to zero. For flow velocities lower than the critical value, the observed vibrations are called sub-critical. Beyond the critical point, the system enters the so-called divergence regime: the rod positions itself back at the center of the channel. If the velocity is increased even further, the rod starts to flutter around the central position with much larger oscillations (analogously to a fluttering hose for watering the garden). The aforementioned process is shown in Figure 1.5. The sub-critical vibrations are generally characterised by a narrow frequency spectrum close to the ground mode value of the rod [26].
In a rod bundle the situation is more complex because of the presence of the surrounding rods. Their effect is to confine even more the considered rod, in-

creasing the damping and reducing the rod's natural frequency. FIV have been widely studied [26, 27] and, recently, Paidoussis wrote a two-volumes handbook collecting most of the knowledge and literature on the subject [24, 28]. However, little has been done to address the specific issue of vibrations induced by coherent structures.

When periodical structures occur in the flow, and their frequency (i.e. rate of passage) is close to the natural frequency of the rod, the amplitude of oscillation is expected to increase drastically. If coherent structures have a length comparable in magnitude with the axial dimension of the rod assembly, they may cause resonance in the first and most energetic mode. Conversely, the presence of shorter, multiple coherent structures on either side of the rod could diminish their effect on the most energetic mode (although they might still cause oscillations at higher, less energetic modes of vibration).

Figure 1.6: The bridge over the Tacoma Narrows before its collapse: the frequency of oscillation of the bridge modulated the shedding frequency with which vortices of air were being shed downstream. This led to a self-excitation which eventually led to the collapse of the structure even though the frequency of oscillations did not match the natural frequency of the bridge. Adopted from [29].

When the shedding frequency of vortices (coherent structures in the case of this work) synchronises with the natural frequency of the rod, this flow-induced instability is referred to as lock-in condition, also known as synchronization.
The shedding frequency of vortices can also differ from the natural frequency of the system, and yet the system can still undergo sustained oscillations. In this case the phenomenon can be regarded as a a self-excitation where the periodicity of the external force imposed on the system is modulated by the oscillation itself [30]. An example is the collapse of the Tacoma Narrows bridge: there the shedding frequency of the vortices formed in the downstream was modulated by the oscillation of the bridge (Figure 1.6), even though the latter was far from the natural frequency [30].

1.4 Influence of the helicoid wire wrapper

Due to the tight arrangement of fuel rods inside the core of a LMFBR, either spacing grids positioned at a specified distance or wrapping wires are used to ensure space among the fuel elements. When the latter solution is pursued, a wire is wrapped helicoidally around each rod to prevent the fuel rods from touching each other due to swelling or buckling of the fuel elements during the reactor operation. If the rods come into contact with each other, the flow speed is locally decreased and the heat transfer deteriorates, leading to hot spots and possible damage on the fuel cladding.
Over the years, considerable efforts have been dedicated to investigating wire-wrapped rod bundles to understand how the wire spacers affect the flow of coolant through the core. A comprehensive review of both experiments and numerical studies was provided by Moorthi *et al.* [31]. Sato *et al.* [32] performed Particle Image Velocimetry (PIV) measurements inside a 7-rod, wire-wrapped hexagonal bundle obeserving that the flow follows the wrapping wire's direction. The flow inside a 61-rod, wire-wrapped hexagonal bundle was extensively studied at Texas A&M University for code validation [33], and for studying vortical structures that may occur in the flow [34, 35]. Computational Fluid Dynamics (CFD) has focused on modelling the flow around a single wrapped-wire pin [36, 37], and on simulating the entire bundle for validation purposes [38, 39, 40, 41]. Recent CFD calculations revealed a very complex flow where the main flow follows the helical path of the wire wraps [42, 43].
Although the flow is mostly found to follow the direction of the wrapped wire, Ohtake *et al.* observed a flow bent against the direction of the wire [44]. This was called "migratory flow" and it was found to depend on the position of the wire around the rod. Similar findings were described in the numerical work of Song *et al.* for a 37-rod, wire-wrapped hexagonal bundle [45]. This interesting phenomenon was ascribed to the hydraulic resistance caused by the relative position of the wire inside the subchannel of the bundle. However, a physical explanation of migratory flow was not provided and it is still missing.

1.5 Scope of this work and thesis outline

The main aspects covered by this research are:

1. The effects of Reynolds number and P/D ratio on frequency and size of coherent structures are investigated in a rectangular channel hosting two half-rods whose distance can be adjusted.

2. Predicting the wavelength of the coherent structures occurring in a rod bundle flow is also of primary importance for both designing experiments, and safely operating a nuclear power plant. Therefore, a new correlation for estimating the size of the coherent structures has been derived and validated against the experiments of this work and performed on different geometries available in literature.

3. The role of coherent structures in inducing vibrations of the fuel rods is of primary interest for the safety of the reactor. Hence the role of coherent structures in flow-induced vibrations is studied in a 7-rod hexagonal bundle.

4. The complex, yet unexplained, migratory flow observed in rod bundle with helicoid wire spacer has been investigated and modelled in a 7-rod wire-wrapped, hexagonal bundle with the help of both experiments and a theoretical approach.

The outline of the thesis is as follows:

Chapter 2 describes the experimental study carried out with a setup consisting of two half-rods facing each other inside a rectangular channel. The flow inside the gap between the rods is studied with Laser Doppler Anemometry (LDA) to assess the effects of Reynolds number and gap spacing on the size of coherent structures as well as on cross-flow. Several Reynolds numbers with three P/D ratios are investigated, being 1.07, 1.13, and 1.20, are studied.
Chapter 3 is about the design and the making process of the two hexagonal rod bundles employed for the experiments described in the following chapters of the thesis. Both the bundles have P/D=1.11. One setup hosts a flexible section in the central rod to study FSI, whereas the second has a helicoid wire wrapped around each rod to study migratory flow.
Chapter 4 describes the experimental campaign carried out with LDA to measure the size of coherent structures occurring in the flow in order to validate a newly derived correlation to predict their wavelength. A high speed camera is employed to measure vibrations induced on the central rod of the bundle (i.e. frequency and amplitude) at several Reynolds numbers.
Chapter 5 describes the experiments performed with PIV in a 7-rod, wire-wrapped hexagonal bundle. The bending of the flow due to the action of the wire is measured near the central rod. A model for predicting the pressure gradient induced by the wire and for estimating the bending angle of the flow is derived and validated against the experiments.
Chapter 6 presents the main findings of this work, and provides recommendations for future studies.

1.6 Nomenclature

Symbols	**Description**
P/D	Ratio between the pitch and the diameter of the half rods

Acronyms	**Description**
CANDU	CAnadian Deuterium Uranium
CFD	Computational Fluid Dynamics
DOE	Department Of Energy
EIE	Extraneously-induced excitation
FIV	Flow-induced vibration
FSI	Fluid-structure interaction
Gen-IV	Generation IV
IAEA	International Atomic Energy Agency
IIE	Instability-induced excitation
LBE	Lead-bismuth eutectic
LDA	Laser Doppler Anemometry
LES	Large Eddy Simulations
LMFBR	Liquid Metal Fast Breeder Reactor
LWR	Light Water Reactor
MIE	Movement-induced excitation
PIV	Particle Image Velocimetry
URANS	Unsteady Reynolds-averaged Navier Stokes

Non dimensional groups	**Description**
Re	Reynolds number

Chapter 2

Vortex streets in a two half-rods compound channel

2.1 Introduction and motivation

Rod bundle flows characterise the core of LMFBR, PWR, BWR or CANDU reactors, as well as steam generators employed in the nuclear industry. In the presence of an axial flow of a coolant, this geometry leads to velocity differences between the low-speed region of the gap between two rods and the high-speed region of the main sub-channels. Moreover, a transversal flow of coherent structures across the gap between two rods can also occur. In a nuclear reactor cross-flow is important as it enhances the heat exchange between the nuclear fuel and the coolant. As a result, the fuel temperature decreases improving the safety performance of the reactor. Much research has been done in studying periodic coherent structures and gap instability phenomena in rod bundles resembling the core of LMFBRs, PWRs, BWRs and CANDUs [10, 11, 12, 16, 14, 15]. However, the effects that the gap spacing and the Reynolds number have on coherent structures and cross-flow is still unclear.

Therefore, this chapter presents the experimental work carried out in order to detect coherent structures and cross-flow inside a single gap between two half-rods facing each other. The distance between the rods, defined by the pitch-to-diameter ratio P/D, can be adjusted to three values. Near-wall measurements in water are performed with the non-intrusive Laser Doppler Anemometry (LDA) measurement system. The optical access is achieved by using Fluorinated Ethylene Propylene (FEP), whose refractive index matches the water's in order to minimise distortion of light.

The content of this chapter has been published in *Nuclear Engineering and Design* **326** (2017), pp. 17-30. DOI:10.1016/j.nucengdes.2017.10.023

2.2 Experimental apparatus

The CAMEL experimental loop consists of the test setup and the Laser Doppler Anemometry (LDA) system. The test section is a rectangular channel with two

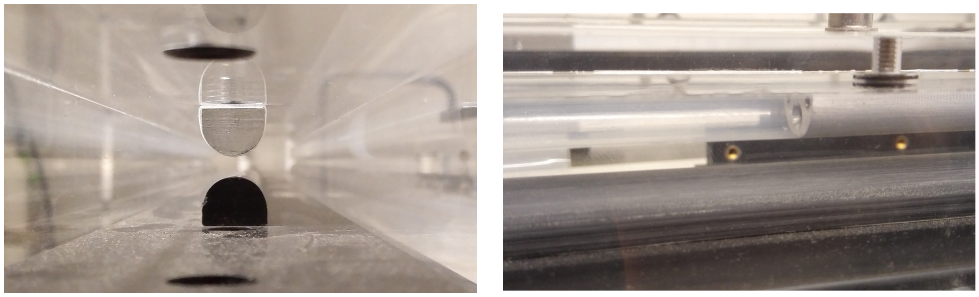

(a) **(b)**

Figure 2.1: a) Main subchannels and central gap defined by the two half-rods. b) Hollow half-rod of FEP seen from the outside of the transparent test section: of the two half-rods the top grey one is the rod hosting the FEP section.

half-rods facing each other (Figure 2.1a), whose distance (P/D) can be adjusted. The water enters the facility from two inlets at the bottom and flows inside the lateral subchannels and through the gap defined by the rods. The flow rate is manually adjusted by two valves at the inlet lines and monitored by two pairs of magnetic flow-meters (Rosemount, USA) for inlet and outlet lines. At the measurement section, one of the two half-rods is made of FEP (Adtech Polymer Engineering), shown in Figure 2.1b, to match the refractive index of the water. A scheme of the loop is sketched in Figure 2.2a. FEP has the same refractive index of water at 20° (η_{FEP}=1.338 [17]; η=1.333 [46] with 532 nm wavelength), so it can be used to minimise the refraction of the laser light when the measurements are performed through the half-rod (Figure 2.2b). To reduce the distortion of light even more, the FEP half-rod is filled with water. The spacing between the rods can be adjusted to P/D ratios of 1.07, 1.13 and 1.20. The measured quantities are the stream-wise and span-wise velocity components and their fluctuations. The dimensions of the test section are given in table 2.1.

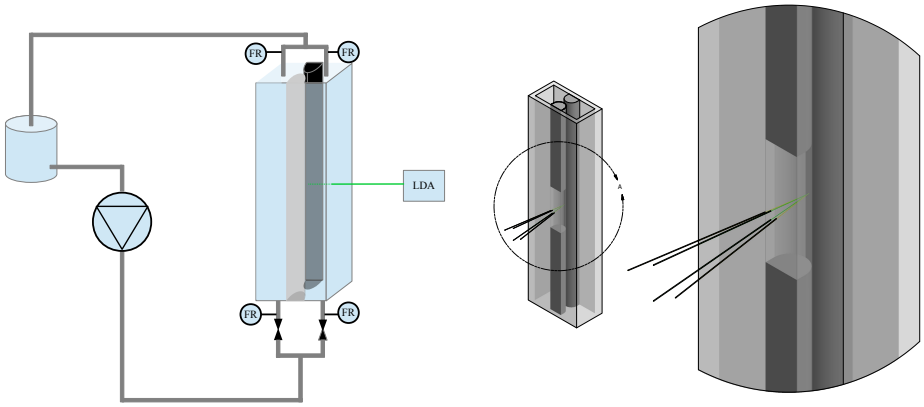

(a) (b)

Figure 2.2: a) CAMEL test loop: a centrifugal pump provides the flow regulated by two valves operated manually at the inlet branches and monitored by 4 magnetic flow-recorders (FR). The water flows out from the top of the test section and it is collected inside a vessel. b) Part of the half-rod is replaced by FEP to let the laser light through during the measurements.

Table 2.1: CAMEL main dimensions. D: half-rod diameter, L: Perspex box long side, H: Perspex box short side, t_{PMMA}: Perspex wall thickness, t_{FEP}: FEP half-rod wall thickness, δ: gap spacing, P/D: pitch-to-diameter ratio.

Parameter	Value	Dimension
D	15	mm
L	58.2	mm
H	26	mm
t_{PMMA}	8	mm
t_{FEP}	0.3	mm
$\delta\,(P/D{=}1.07)$	1	mm
$\delta\,(P/D{=}1.13)$	2	mm
$\delta(P/D{=}1.20)$	3	mm

2.3 Laser Doppler Anemometry system

The measurement system is a 2-components LDA system (DANTEC, Germany): a green laser beam pair (wavelength of 561 nm) measures the stream-wise velocity component and a yellow laser beam pair (wavelength of 532 nm) the lateral component with a maximum power of 300 mW. The measurement settings are chosen through the BSA Flow Software. The flow is seeded with particles to scatter the light and allow their detection inside the measurement volume. Borosilicate glass hollow spheres with an average density of $1.1\,\mathrm{g\,cm^{-3}}$ and a diameter of $9-12\,\mu\mathrm{m}$ are employed. The measurement region is formed by the two overlapping laser beams, forming an ellipsoidal measurement volume (or probe). In this region, the two beams form fringes whose distance $\mathrm{d_f}$ is known through the following relation:

$$\mathrm{d_f}=\frac{\lambda_\mathrm{l}}{2\sin\alpha}, \tag{2.1}$$

where λ_l is the wavelength of the laser light and α is the half-beam angle. If a particle goes through the measurement volume, the light that is scattered back has a different wavelength than the one hitting the particle. This difference depends on the particle's velocity according to the Doppler effect (see Figure 2.3). The reflected light is collected by the receiving optics and converted into an electric current, called Doppler burst. This is a signal oscillating in time with frequency f_D. Finally, the velocity of the particle in a plane perpendicular to plane of the laser beam is calculated as

$$v=\mathrm{d_f}\cdot f_\mathrm{D}. \tag{2.2}$$

A schematic of the LDA system is shown in Figure 2.3. The frequency of the light of one laser per pair is shifted to detect also the direction of motion of the particle. The LDA is moved by a traverse system and, to provide a dark background, the whole apparatus is enclosed by a black curtain.

2.3.1 LDA uncertainty

The uncertainty on the measurements has different expressions for mean velocities and root mean square values. They are defined as [48]

$$\sigma_{\bar{v}}=\frac{\sigma}{\sqrt{\mathrm{N}}}=\sqrt{\frac{1}{\mathrm{N}\,(\mathrm{N}-1)}\sum_{i=1}^{\mathrm{N}}(v_i-\bar{v})^2}\quad \sigma_\mathrm{rms}=\frac{\sigma_{\bar{v}}}{\sqrt{2\mathrm{N}}}, \tag{2.3}$$

where $\sigma_{\bar{v}}$ and σ_rms are the uncertainty on the mean value and on the root mean square of the velocity components, σ is the standard deviation of the measured samples, N is the number of samples, and $\bar{v}$ is the mean velocity value.
Each measurements point is measured for a time window long enough to achieve sufficiently narrow confidence intervals. At high flow rates the recording time is set to 30 s whereas, for low flow rates, the recording time is as long as 120 s. The most critical conditions are encountered at very low Reynolds numbers and in the centre of the gap because the laser beams must pass the FEP half-rod (see "path A", Figure 2.4a). Here, the maximum σ_rms is 1.5%. The lower the Reynolds number,

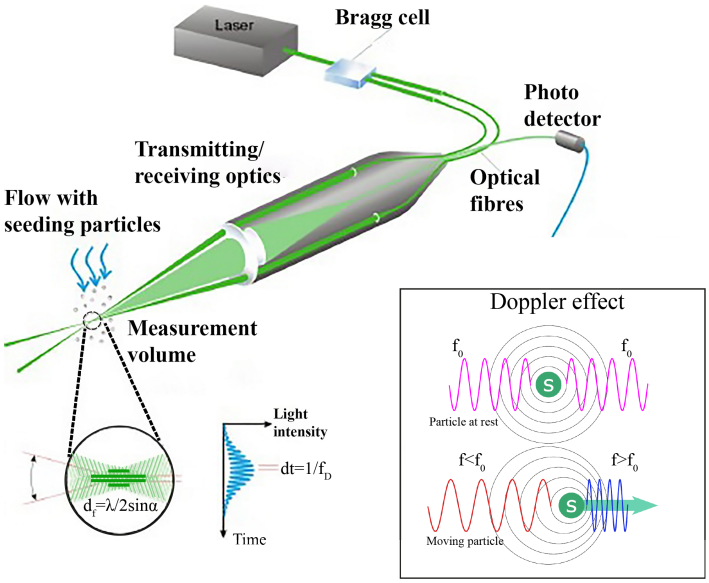

Figure 2.3: Schematic of LDA measurement system. Image modified from [47]. Doppler effect: the frequency of light reflected by a moving particle differs from the one impinging on the target.

the more samples are required and the longer the acquisition time is. With a P/D of 1.20 (i.e. 3 mm gap spacing, see table 2.1), for example, $\sigma_{\bar{v}}$=0.8% for the stream-wise component and becomes $\sigma_{\bar{v}}$=0.5% when measuring from the side (path B). The span-wise velocity exhibits even more significant uncertainties since it is always characterised by near-zero values. $\sigma_{\bar{v}}$ increases when the measurement volume approaches the wall (lower data rate) and if the gap width is reduced (see Figure 2.4a). In the latter case, the issue of the light reflected into the photodetector can be tackled to some extent (see section 2.5.5).

2.3.2 Slotting technique

One of the most common techniques for computing the frequency spectrum of a signal is the Fast Fourier Transform (FFT), which requires regularly-sampled data. However, with LDA measurements, the inter-arrival time (time between two detected particles) is not constant as it depends on when the particle is carried through the measuring laser probe by the flow. This issue can sometimes be overcome by applying the sample-and-hold algorithm to the original velocity signal. This means that the velocity of each sample is kept constant ("hold") until the next particle is detected. The entire signal is then resampled with constant time intervals, and then the FFT is applied.
However the sample-and-hold technique followed by FFT works well only with high data rate. If the data rate is low or if the inter-arrival times differ by much, the effect of the so-called white noise on the spectrum becomes more important

[49]. The longer the "hold" phase, the more the re-sampled signal is biased with respect to the real one.
Alternatively, one can calculate the discretized autocorrelation function of the velocity by means of the Slotting technique [50], and then use the Fourier transform to compute the spectrum. Sample pairs with inter-arrival time falling within a certain time interval (lag time) are allocated into the same time *slot* of width $\Delta\tau$, hence the name of the method. Then the ensemble average of the cross-products falling within each slot is calculated as

$$\rho_{\mathrm{ac}}(k\Delta\tau)=\frac{\sum v_i(t_i)\,v_j(t_j)}{N_{\mathrm{slot}}} \quad k=0,1,2,\ldots M-1, \tag{2.4}$$

where $\rho_{\mathrm{ac}}(k\Delta\tau)$ is the autocorrelation coefficient for the time slot $k\Delta\tau$, $v_i(t_i)\,v_j(t_j)$ are the cross-products whose arrival time differences falls within the considered lag time. In mathematical terms that is

$$\Delta\tau\,(k-1/2)\leq t_i-t_j\leq\Delta\tau\,(k+1/2)\,.$$

The frequency spectrum is then calculated as

$$S=\frac{\Delta\tau}{\pi}\left[\frac{1}{2}\rho_{\mathrm{ac}}(0)+\sum_{k=1}^{M-1}\rho_{\mathrm{ac}}(k\Delta\tau)\cos(2\pi fk\Delta\tau)\right]. \tag{2.5}$$

The randomness of the sampling process increases the variance of the spectrum. This can be reduced by increasing the mean seeding data rate through the probe. However, this is not always possible, especially in regions characterised by low velocity (i.e. the centre of the gap) or with low flow rates. Therefore, the so-called Fuzzy algorithm is implemented in the Slotting technique. Cross-products with inter-arrival time closer to the centre of a slot contribute more to the autocorrelation estimation [51, 52].
Generally the spectrum can also be biased towards higher velocities (i.e. higher frequencies) since the amount of high speed particles going through the measurement probe is larger than for low speed particles [49]. Hence, their contribution to the spectrum would be higher than in reality. The Slotting technique hereby implemented adopts the transit time algorithm to weight the velocity samples by their residence time within the measurement probe to decrease the velocity bias.

2.4 Measurement campaign

The measurements are conducted along two paths: along the symmetry line of the gap, from one sub-channel to the other, and at the centre of the gap along the rod-to-rod direction. For each P/D ratio, different flow rates, hence different Reynolds numbers, are studied. The first series of measurements is done by shooting the laser through the FEP half-rod (Figure 2.4a) and by mapping the symmetry line through the gap.
The second series of experiments is done with the light entering the setup through the short Perspex side (Figure 2.4b), without crossing the FEP. In this case the

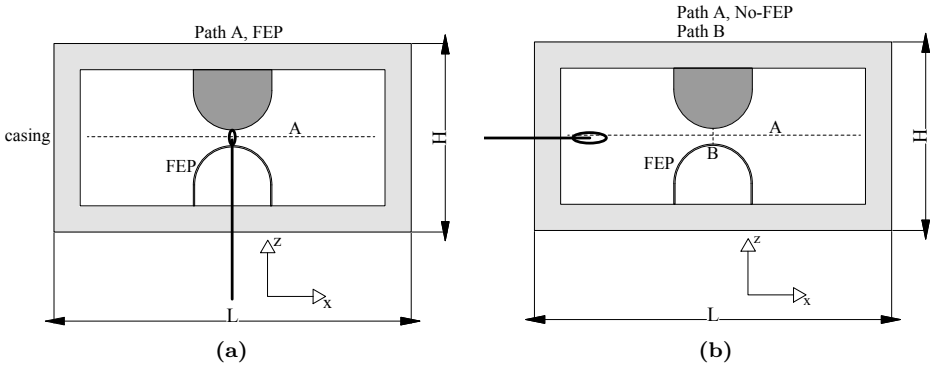

Figure 2.4: a) Top view of the measurement crossing the FEP. The ellipsoidal measurement volume is represented as well; the solid line represents the laser beam (sketch not drawn to scale). b) Top view of the measurement without crossing the FEP. The measurement paths followed by the laser probe are the dashed lines.

measurements are performed along both the symmetry line through the gap and normal to the rods at the centre. The Reynolds number of the bulk flow, Re, is calculated based on the bulk velocity:

$$Re = \frac{\rho \cdot V_\mathrm{b} \cdot D_\mathrm{h}}{\mu}, \tag{2.6}$$

where ρ is the water density, μ is the water dynamic viscosity, V_b is the bulk velocity calculated as $V_\mathrm{b}=Q/A$ where Q is the total flow rate and A is the total flow area, $D_\mathrm{h}\equiv 4A/P_\mathrm{w}$ is the hydraulic diameter of the test section, being P_w the wetted perimeter. The Reynolds number of the gap region, Re_gap, is calculated as

$$Re_\mathrm{gap} = \frac{\rho \cdot v_\mathrm{gap} \cdot D_\mathrm{h}^*}{\mu}, \tag{2.7}$$

where D_h^* is the hydraulic diameter of the gap region defined by the flow area bounded by the two half-rod walls and closed by the gap borders at the rod ends. v_gap is the average stream-wise velocity through the gap region, which is the average of the surface average of the stream-wise velocity $v(x,z)$ measured over the area A shown in Figure 2.5 at discrete locations by moving the laser probe through the measurement section. The average stream-wise gap velocity v_gap is calculated as

$$v_\mathrm{gap} = \frac{1}{A_\mathrm{gap}} \int_{z_1}^{z_2} \int_{x_\mathrm{L}}^{x_\mathrm{R}} v(x,z)\mathrm{d}x\mathrm{d}z, \tag{2.8}$$

where x_L, x_R, z_1, z_2 are the coordinates defining the area A, and $v(x,z)$ is the result of the measurements.
Q, Re, V_b and Re_gap for the three P/D ratios are reported in table 2.2.

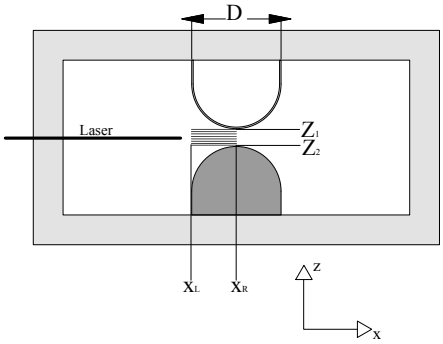

Figure 2.5: Top view of the flow area over which v_{gap} is measured at discrete locations to estimate the gap Reynolds number.

Table 2.2: Q: flow rate; Re: Reynolds number of the main subchannel based on the bulk velocity V_{b}; Re_{gap}: Reynolds number of the gap region estimated for the three P/D ratios.

$Q\,[\text{m}^3\,\text{s}^{-1}]$	Re	$V_{\text{b}}\,[\text{m}\,\text{s}^{-1}]$	Exp. Re_{gap}		
			P/D=1.07	P/D=1.13	P/D=1.20
$9.60e-4$	29 000	0.79	3000	3800	5000
6.80×10^{-4}	20 000	0.56	2160	2750	3400
3.80×10^{-4}	12 000	0.31	1100	1500	1760
2.20×10^{-4}	65 000	0.18	580	880	930
1.20×10^{-4}	3600	0.10	310	400	600
0.80×10^{-4}	2400	0.07	130	200	470
0.40×10^{-4}	1200	0.03	100	100	190
0.20×10^{-4}	600	0.02	30	50	130

2.5 Results and discussion

2.5.1 Stream-wise velocity r.m.s. through the gap

The stream-wise velocity component v and its root mean square v'_{rms} are measured along "path A, No-FEP" (Figure 2.4b). The data are then corrected for the refraction of light due to the Perspex wall (later discussed in section 2.5.6). The main subchannels are located at $|x/D|$=1, where the stream-wise velocity profile reaches the highest value, whereas the gap borders are at $|x/D|$=0.5. The centre of the gap is at x/D=0, where the minimum in the velocity profile is measured. The normalised difference between the velocity in the bulk and in the gap increases if either the Reynolds number or the P/D decrease.
Figure 2.7 compares the results obtained with this geometry and the geometry

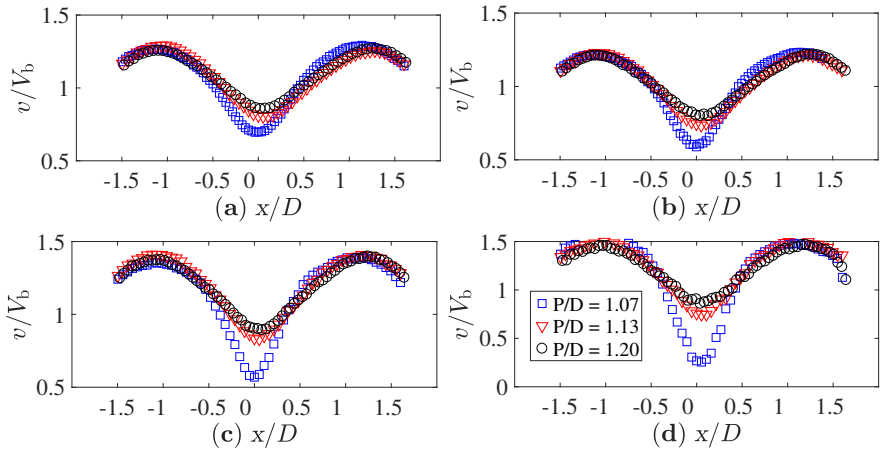

Figure 2.6: Stream-wise velocity component against the normalised horizontal coordinate x/D along the gap. a) Re=29 000, b) Re=12 000, c) Re=6500, d) Re= 2400. The data are normalised by the bulk velocity.

used by Mahmood [17] at similar values of Re. The normalised velocity difference between the bulk region and the gap centre is larger with the two half-rods geometry ($\bigtriangledown$) than with only one half-rod ($\times$); this is more evident with the lower Reynolds number. The effect of the gap size on the normalised velocity difference is further discussed in section 2.5.4 with the aid of Figure 2.17.

The profiles of the stream-wise and span-wise velocity components shown Figure 2.8 , v'_{rms} and u'_{rms} respectively, correspond to P/D=1.07; the horizontal coordinate is normalised by the rod diameter D.

Both profiles of Figure 2.8a have two peaks at the borders of the gap ($|x/D|$=0.5) and a dip region in the centre. As the measurement approaches the walls of the Perspex encasing ($|x/D|$>1) the v'_{rms} increases like in common wall-bounded pipe flows. The water enters the facility via two bent rubber pipes next to each other. The bend causes a non-zero lateral momentum transfer among the subchannels that is responsible for the asymmetry of the v'_{rms} profile at $|x/D|\approx$0.5 (Figure 2.8a). The lower Re case reported in Figure 2.8a exhibits a symmetric v'_{rms} profile with respect to the gap centre. If the P/D ratio is increased to 1.13 and 1.20, the v'_{rms} profile appears symmetric (Figure 2.9). The gap region acts as a damping region for flow oscillations [14], especially with smaller gaps where the confinement of lateral momentum within the sub-channel is more dominant. If the gap size is increased, such transversal components may redistribute more freely among the subchannels, which may explain why the v'_{rms} profile is more symmetric with larger gaps.

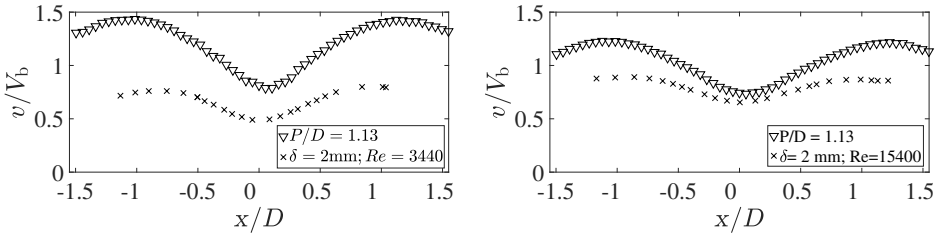

Figure 2.7: Comparison between the stream-wise velocity profile with P/D=1.13 and experiments from Mahmood [17]. a) Stream-wise velocity normalised by the bulk velocity at Re=3600 compared with data obtained at Re=3440. b) Stream-wise velocity normalised by the bulk velocity at Re=12 000 compared with data obtained at Re=15 400. Data from [17] are obtained from a similar geometry consisting of one half-rod.

2.5.2 Stream-wise velocity r.m.s. from rod to rod

The v'_{rms} is measured for each P/D ratio and flow rate at the centre of the gap, from rod to rod. The results for each Re value are plotted against the rod-to-rod coordinate z, normalized by the gap spacing δ. The flow shows some analogy with common wall-bounded flows in that it features two near-wall peaks where the viscous stresses equal the Reynolds shear stresses [53] and the turbulent production is the highest. A dip occurs in the centre for Re=29 000, Re=20 000 and Re=12 000 (Figure 2.10). v'_{rms} decreases approaching the rod walls due to the viscous sub-layer: velocity fluctuations can still be detected inside this region but they are produced in the outer log-layer region [54]. With Re=12 000 and P/D=1.07, a weak third peak in the v'_{rms} appears between the rod walls. As Re is decreased to 6500, this additional peak becomes clearer and dominant over the near-wall peaks. The v'_{rms} profiles for P/D=1.13 and P/D=1.20 do not display such a peak, although the near-wall peaks become less sharp. The results of the measurements performed with the four lower Reynolds numbers are reported in Figure 2.11. The v'_{rms} profile with Re=3600 increases towards the centre of the gap for P/D=1.07 and P/D=1.13, whereas the case with P/D=1.20 still displays a weak dip. If Re is further decreased to 2400 the P/D ratios have all the same increasing trend towards the centre. With Re=1200 and Re=600, the v'_{rms} profile varies significantly depending on the P/D ratio. The central v'_{rms} peak can be originated by the transport of turbulence from the borders of the gap region (where the production is higher) towards the centre by means of cross-flow. The analysis of the frequency spectrum of the span-wise velocity component can confirm this assumption: the periodical transversal flow would appear as a peak in the frequency spectrum of the measured velocity component [12, 16].

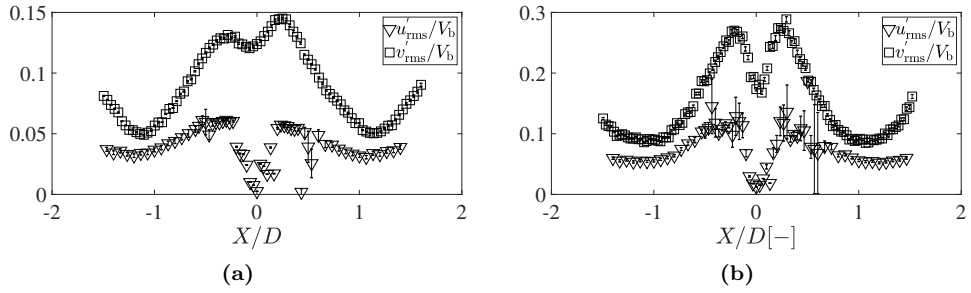

Figure 2.8: a): v'_{rms}/V_b and u'_{rms}/V_b profiles along the gap; P/D=1.07, Re=29 000. The asymmetry in the stream-wise v'_{rms}/V_b is due to the lateral momentum component of the flow in the main sub-channels. b): v'_{rms}/V_b and u'_{rms}/V_b profiles along the gap; P/D=1.07, Re=3600.

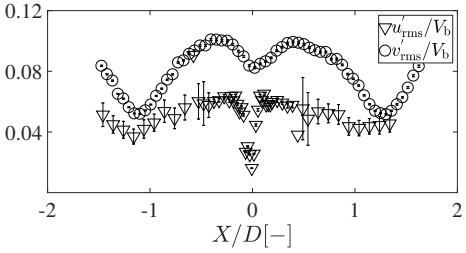

Figure 2.9: v'_{rms}/V_b and u'_{rms}/V_b profiles along the gap; P/D=1.20, Re=29 000.

2.5.3 Cross-flow pulsations through the gap

The study of the autocorrelation function and the frequency spectrum of the span-wise (lateral) velocity component u is a powerful method to detect and characterize periodicities in the flow. The frequency spectrum of u is calculated with the Slotting technique [55, 50, 56]. The span-wise velocity is measured across the FEP half-rod ("path A, FEP"), as shown in Figure 2.4a, at several points between the bulk region of the flow and the centre of the gap; the spectrum is then calculated.

The spectra exhibit a peak at different measurement locations near the centre for $Re \leq 6500$, as shown in Figure 2.12. The peak in the power spectra proves that there is a low-frequency periodic behaviour in the span-wise velocity component of the flow near the centre of the gap. This can be the result of large coherent flow structures forming near the rod edges and periodically crossing the gap. The spectral peaks are fitted with a Gaussian bell so that the mean and the bell's width are estimated. The cross-flow frequency decreases with increasing gap spacing (Figure 2.13a) within the Reynolds number range $2400 - 6500$, as found also by Wu and Trupp [57]. The frequency values are also expressed as a non dimensional

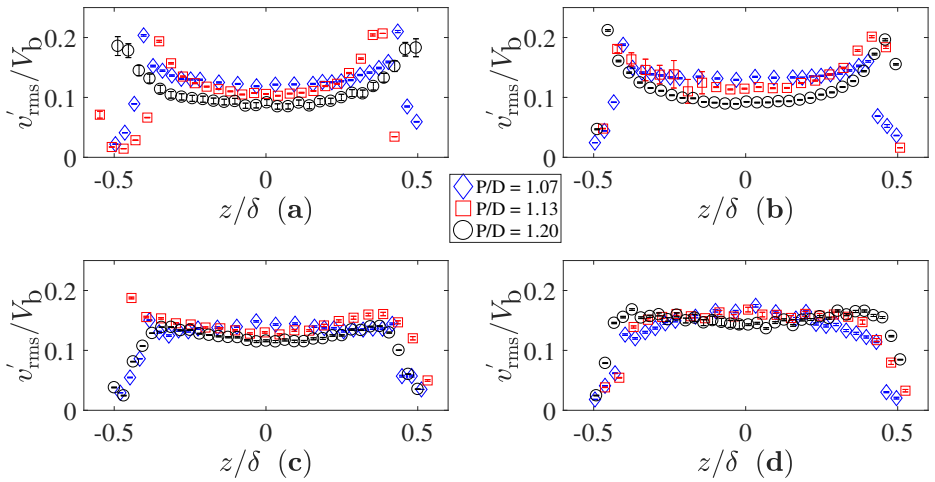

Figure 2.10: v'_{rms}/V_b profile at the centre of the gap (path B; No-FEP), between the half-rod walls. a) Re=29000, b) Re=20000, c) Re=12000, d) Re=6500; P/D= 1.20 (black), P/D=1.13 (red) and P/D=1.07 (blue). As Re decreases, a weak peak appears first with P/D=1.07 (Re=12000), which is also found with P/D=1.13 and Re=6500.

quantity via the Strouhal number (Figure 2.13b), defined as

$$Str = \frac{f_x \sqrt{D\delta}}{v_{in}}, \tag{2.9}$$

where f_x is the average frequency at which the structures cross the gap, D is the half-rod diameter, δ is the gap spacing (hence depending upon the P/D ratio) and v_{in} is the value of v estimated at the inflection point ($\partial^2 v/\partial x^2$=0) of the velocity profile measured along path A ("path A, No-FEP" Figure 2.4b): here the velocity gradient is the largest [58]. The rod diameter D and the gap spacing δ are important parameters in experiments with rod bundles. The characteristic length scale of the Strouhal number includes both, following the definition of Meyer [59]. The following fit is proposed:

$$1/Str = 31.2 \cdot P/D - 24.6. \tag{2.10}$$

Equation 2.10 describes the overall trend of the experimental points measured for three P/D values in the range $2400 \leq Re \leq 6500$. Note that, on top of Equation 2.10, the Strouhal number depends in turn on the P/D ratio through the δ term (see Equation 2.9). It has to be pointed out that this correlation is an estimation of the global trend. However, if the data series corresponding to the three P/D ratios are considered separately, the dependence between $1/Str$ and P/D may not be necessarily linear.

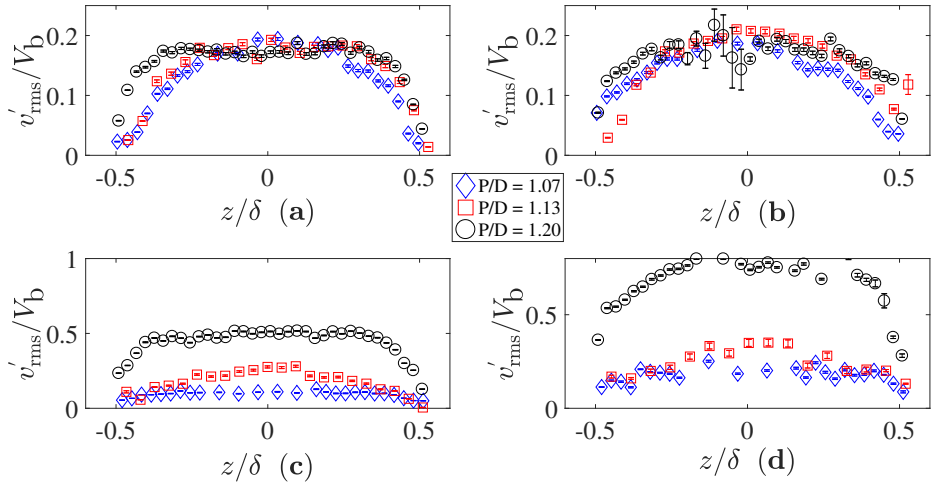

Figure 2.11: v'_{rms}/V_b profile at the centre of the gap (path B; No-FEP), between the half-rod walls. a) Re=3600, b) Re=2400, c) Re=1200, d) Re=600; P/D ratio of 1.2 (black), 1.13 (red) and 1.07 (blue). As the Re is further decreased, the P/D=1.20 also leads to an increase of turbulence between the rod walls, in the centre of the gap.

The lateral frequency of the structures seems to be independent of the Reynolds number and to be affected only by the geometry of the channel, for $Re \geq 2400$ (Figure 2.14a). However, at low Reynolds numbers, Str decreases with the Reynolds number. These results and those of Möller [12] are compared in Figure 2.14b. He defined the Strouhal number in a different way, being

$$Str_\tau = \frac{f_x \cdot D}{u_\tau}, \tag{2.11}$$

where u_τ is the friction velocity defined as

$$u_\tau = \sqrt{\frac{\mu}{\rho}\left(\frac{\partial v}{\partial z}\right)_{wall}}, \tag{2.12}$$

where $\left(\frac{\partial v}{\partial z}\right)_{wall}$ is the velocity gradient near the wall of the rod.

2.5.4 Gap vortex streets

The stream-wise velocity component v measured in the left part of the gap ("path A, No-FEP" Figure 2.4b) is used to calculate the frequency spectrum. The average frequency of the spectral peak f_y is plotted at the location where the coherent structures are detected within the gap (Figure 2.15). This represents the spatial distributions of the coherent structures depending on the considered Reynolds

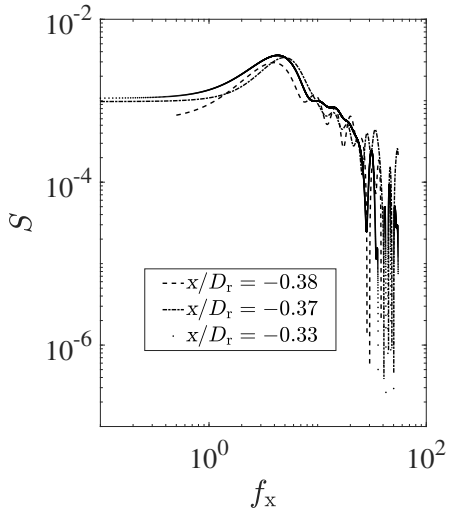

Figure 2.12: Frequency spectrum of the span-wise velocity component u for Re=6500 and P/D=1.07; three locations near the centre of the gap are shown. A peak is evident near 3.8 Hz. The fit with a Gaussian bell yields a mean standard deviation of 1.47 Hz.

number. Peaks in the frequency sectrum are found for all the P/D ratios at different locations within the gap and inside the main sub-channel close to the gap borders, suggesting gap vortex streets moving along with the stream. The case with P/D= 1.07 (Figure 2.15a) shows that f_y increases with Re. For Re=600 the flow structures extend well within the main sub-channel whereas, as the Reynolds increases, the structures are localised within the gap and at the gap border. The case with P/D=1.13 (Figure 2.15b) shows once more that the frequency increases with Re. However, the spatial distribution is more scattered at high Reynolds.
This result indicates that the structures tend to move closer to the gap centre as the Reynolds increases. Taylor's hypothesis (coherent structures in the flow are regarded as frozen entities moving with the stream at velocity v_{in}) enables to estimate the average length of the vortices. Although this assumption may become inaccurate with very long structures [60], experiments in bundles show that these vortices move with a convection velocity which is independent of the position inside the gap [8]. The structure length is calculated as

$$\lambda = \frac{v_{in}}{f_y}, \tag{2.13}$$

where v_{in} is the stream-wise convection velocity measured at the inflection point of the velocity profile through the gap ("path A, No-FEP" Figure 2.4b). The spectral peak is fitted with a Gaussian bell to retrieve the mean frequency value and the bell's width σ_y. This gives a frequency interval $f_y \pm \sigma_y$ to estimate also the lower and upper limit around the mean structure length λ:

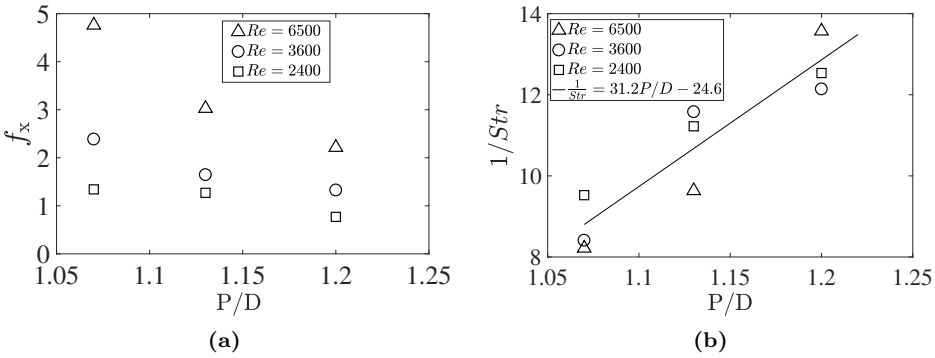

Figure 2.13: a) Average span-wise frequency against P/D for three values of Re. b) $1/Str$ against P/D: experimental results and proposed correlation.

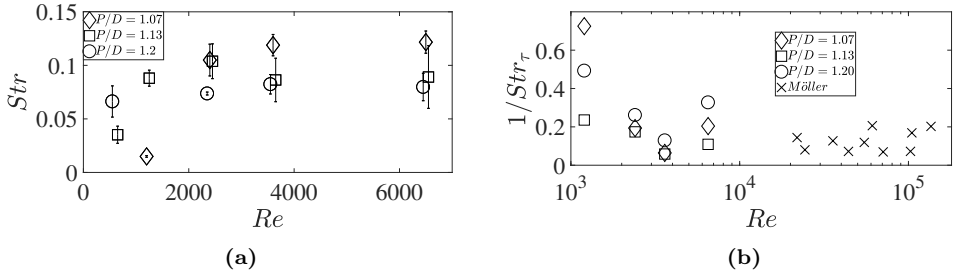

Figure 2.14: a) Average non-dimensional span-wise frequency versus Re for three P/D ratios. b) $1/Str_\tau$ against the Reynolds number for the three P/D values compared with [12].

$$\lambda_{\min} = \frac{v_{\text{in}}}{f_y + \sigma_y} \quad \lambda_{\text{Max}} = \frac{v_{\text{in}}}{f_y - \sigma_y} \tag{2.14}$$

The mean wavelength of the structures is shown in Figure 2.16 as a function of Re. Coherent structures become longer with $Re \leq 2400$ consistently with results presented in [17, 61] for compound channels. With increasing Re, λ tends to reach the asymptotic value of

$$\frac{\lambda}{D_h^*} \approx 14, \tag{2.15}$$

as observed in [14].

From Figure 2.16a it appears that with $Re \geq 2400$ the length of the periodical structures is merely affected by geometrical parameters such as the gap spacing, confirming, thus, one of the findings reported in [18, 19].

The velocity difference between the bulk flow and the centre of the gap, normalised by the bulk velocity, is plotted in Figure 2.17 for the three gap sizes. Its

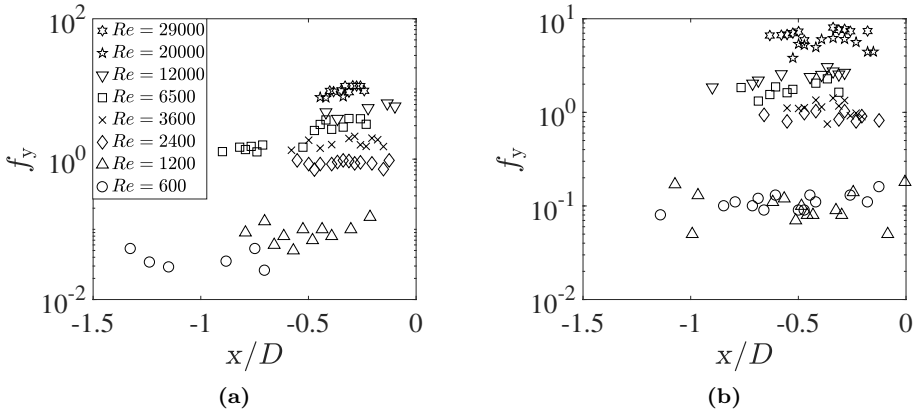

Figure 2.15: Stream-wise frequency of the structures f_y as a function of the position where it is measured for a) P/D=1.07 and b) P/D=1.13.

trend versus the Reynolds number is similar to the what is observed with the wavelength of the structures. For Re>6500 the velocity difference becomes almost constant for increasing values of Reynolds, whereas for $Re\leq$6500 it increases as the Reynolds number decreases. Moreover, it is evident from the figure that a smaller gap induces a higher velocity differences between the gap region and the main subchannel.
Since the driving force of coherent structures is the velocity difference between the bulk flow and the centre of the gap, the almost-constant profile that this assumes for high Reynolds numbers could be related the constant length of coherent structures in the same range of Reynolds. However, for $Re\leq$2400 the Reynolds number has a strong influence on the stream-wise structure size (Figure 2.16a). The lengthening of the structures at low flow rates, and the widening of the region where they are found (Figures 2.15a, 2.15b) seem to indicate that these structures grow both in length and in width as the Reynolds decreases, as hypotesized in [62].

An almost-constant wavelength of the coherent structures allows to compare the turbulent dissipation rate of the flow at different Reynolds numbers, as explained below.
According to Kolmogorov's length scale, the ratio between the largest and smallest vortices occurring in the flow, d_{Max} and d_{min} respectively, is proportional to $Re^{3/4}$ [63]:

$$\frac{d_{\mathrm{Max}}}{d_{\mathrm{min}}} \approx Re^{3/4}. \tag{2.16}$$

Assuming that the largest eddies occurring in the flow correspond to the measured coherent structures, that is $d_{\mathrm{Max}} \equiv \lambda$, the previous expression becomes

$$\frac{\lambda}{d_{\mathrm{min}}} \approx Re^{3/4}. \tag{2.17}$$

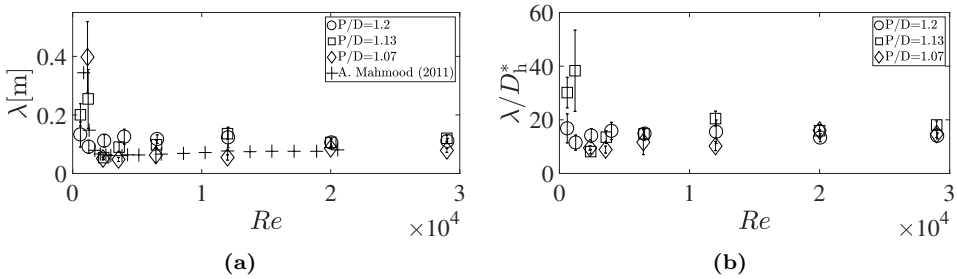

Figure 2.16: a) Absolute and b) normalised stream-wise coherent structures size as a function of Re for three P/D ratios. The experiments are compared with data from [17]. The normalised data are scaled with the hydraulic diameter of the gap region.

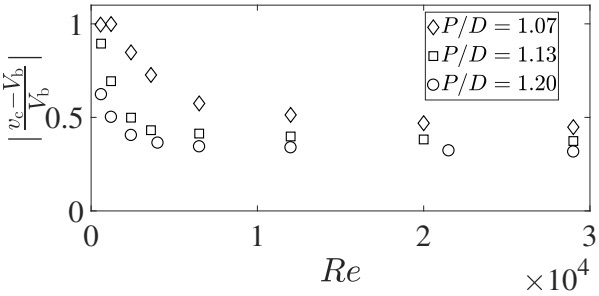

Figure 2.17: Normalised velocity difference between the bulk of the flow and the centre of the gap for three P/D ratios.

The wavelength λ can be expressed as

$$\lambda \approx d_{\min} Re^{3/4}. \tag{2.18}$$

From the experiments it follows that, for $Re \geq 2400$, λ is weakly dependent on the Reynolds number (Figure 2.16a), so the following approximation is done (accurate within 15% of the mean value):

$$[\lambda]_{Re=2400} \approx [\lambda]_{Re=29\,000}. \tag{2.19}$$

From Equation 2.18 follows that

$$\left[d_{\min} \cdot Re^{3/4}\right]_{Re=2400} \approx \left[d_{\min} \cdot Re^{3/4}\right]_{Re=29\,000}. \tag{2.20}$$

$d_{\min}$ is defined by the Kolmogorov microscale as $d_{\min} = \nu^{3/4} \varepsilon_{\mathrm{d}}^{-1/4}$ where ν is the kinematic viscosity and ε_{d} is the energy dissipation rate. Substituting this expression into the previous equation leads to

$$\left[\nu^{3/4} \varepsilon_{\mathrm{d}}^{-1/4} Re^{3/4}\right]_{Re=2400} \approx \left[\nu^{3/4} \varepsilon_{\mathrm{d}}^{-1/4} Re^{3/4}\right]_{Re=29\,000}. \tag{2.21}$$

Since ν is constant, the equation is simplified into

$$\left[\varepsilon_{\mathrm{d}}^{-1/4} Re^{3/4}\right]_{Re=2400} \approx \left[\varepsilon_{\mathrm{d}}{}^{-1/4} Re^{3/4}\right]_{Re=29\,000}. \tag{2.22}$$

This relation states that the quantity $Re^3/\varepsilon_{\mathrm{d}}$ is conserved if the wavelength of coherent structures does not change within the considered range of the Reynolds number:

$$\frac{Re^3}{\varepsilon_{\mathrm{d}}} \approx \mathscr{K}_1, \tag{2.23}$$

where $\mathscr{K}_1$ is a constant and $Re \in [2400; 29\,000]$. This equation is useful to compare the turbulent dissipation rate ε_{d} measured at two different Reynolds numbers. Equation 2.23 can be applied to the cases with Re=2400 and Re=29 000:

$$\left[\frac{Re^3}{\varepsilon_{\mathrm{d}}}\right]_{Re=2400} = \left[\frac{Re^3}{\varepsilon_{\mathrm{d}}}\right]_{Re=29\,000}, \tag{2.24}$$

which yields

$$\frac{[\varepsilon_{\mathrm{d}}]_{Re=29\,000}}{[\varepsilon_{\mathrm{d}}]_{Re=2400}} = \left(\frac{29\,000}{2400}\right)^3 \approx 1780. \tag{2.25}$$

An almost-constant wavelength of coherent structures implies that the dissipation rate with Re=29 000 is approximately three orders of magnitude larger than with Re=2400.

The remainder of the chapter compares the v'_{rms} measured along path A for the "FEP" and "No-FEP" cases (see Figures 2.4a and 2.4b) to assess the effects of the refraction and reflection of light.

2.5.5 Light reflection effects

When measuring along "path A, FEP" (see Figure 2.4a) the measurement is disturbed by the light reflected from the second rod behind the ellipsoidal laser probe. As the probe is moved further towards the centre of the gap the reflection becomes increasingly stronger, especially with P/D=1.07. This issue is tackled by filtering out the near-zero velocity samples caused by the reflective surface. This improves the results as long as the ellipsoidal volume fits the gap and the flow speed is not too close to zero. The cases where the filter is successfully applied are shown in Figure 2.18. Although the filtered v'_{rms} shows yet some dispersion close to the left border of the gap (x/D=−0.5 in Figure 2.18a), it decreases the overall scattering of the experimental values. As the probe approaches the FEP borders, the signal drops because these are the regions where the light attenuation is the highest.

2.5.6 Light refraction effects

In one case (Figure 2.4a) the refraction occurs when the laser crosses the FEP rod and in the other case (Figure 2.4b) refraction is caused by the Perspex wall as the probe volume moves further inside the test section. The results of the measurements for both cases are corrected to compensate for this issue. Referring

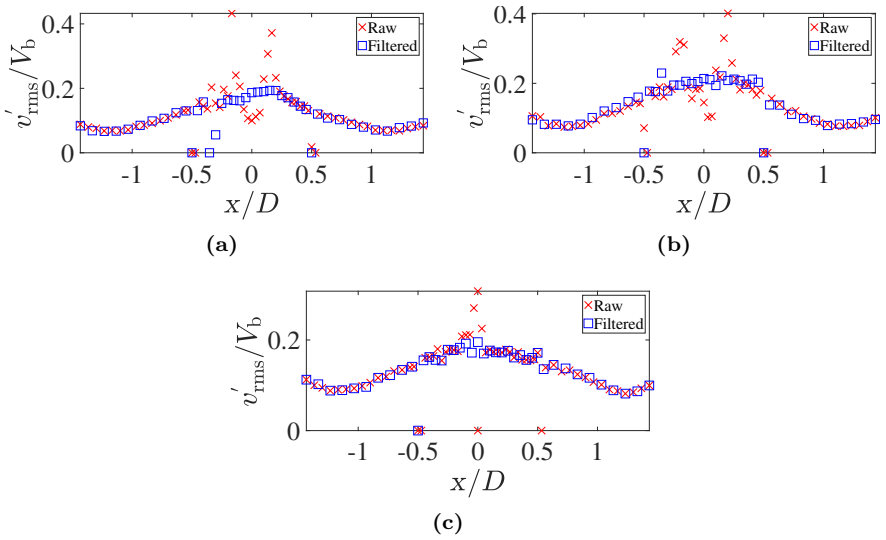

Figure 2.18: Comparison between the v'_{rms}/V_b affected by light reflection from the wall (red) and filtered (blue). a) P/D=1.13 a) Re=6500, b) Re=3600. c) P/D=1.20, Re=3600.

to Figure 2.20a, the horizontal distortion of the light ray due to FEP is estimated as follows:

$$\Delta x = \overline{AB} \sin(\alpha_1 - \alpha_3). \tag{2.26}$$

For a complete derivation of the previous equation, the reader is directed to Appendix A.

The refraction of the laser beam through the Perspex wall is discussed with the aid of Figure 2.20b. The position of the probe volume inside the setup, corrected by the refraction due to the Perspex wall, is given by

$$\Delta x = t_{PMMA} - X_0 + \frac{X_0 \tan\alpha_5 - t_{PMMA} \tan\alpha_6}{\tan\alpha_7}, \tag{2.27}$$

where t_{PMMA} is the Perspex wall thickness, X_0 is the position of the probe volume without refraction and α_5=5.711° is the half-beam aperture of the laser; α_6 and α_7 are calculated through the Snell's law. The v'_{rms} measured through the FEP half-rod ("path A, FEP") and from the short side ("path A, No-FEP") are shown in Figure 2.19. The two v'_{rms} profiles are yet slightly shifted with respect to each other after the refraction correction is applied: Equations 2.26 and 2.27 depend on t_{PMMA}, t_{FEP} and on $R_{i,FEP}$ which vary due to the dimensional tolerance of the material. This introduces a source of uncertainty in the refraction calculation. Moreover, when the laser reaches the FEP borders ($|x/D|$=0.5), the light is not transmitted anymore and the signal drops to zero.

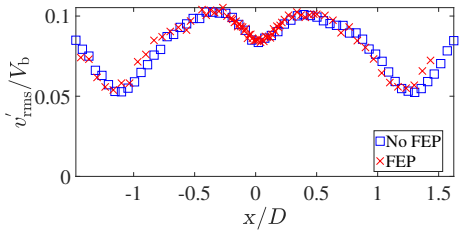

Figure 2.19: v'_{rms}/V_b measured along "path A, FEP" and "path A, No-FEP" against the position along the gap normalized by the half-rod diameter. P/D=1.20, Re=29 000.

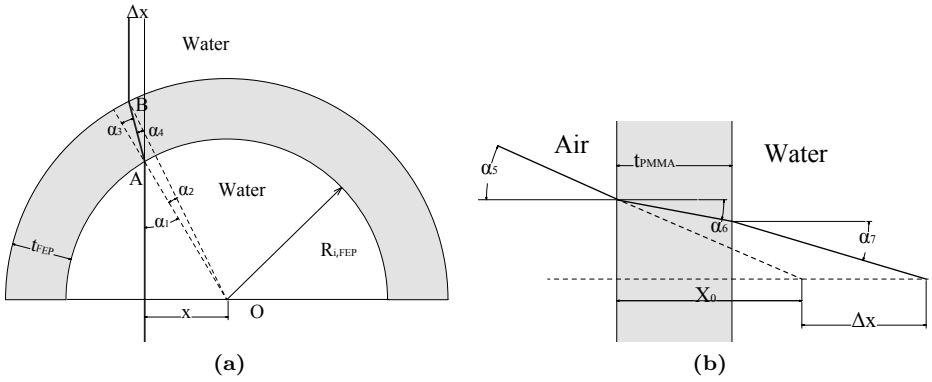

Figure 2.20: a) Top view of the refraction of the green laser beam pair due to FEP: the light ray goes through the FEP half-rod, filled with water, and it is refracted as it crosses its wall. b) Refraction of the laser beam as it crosses the FEP half-rod.

2.5.7 Laser probe size effects

The refraction of the laser beam pair affects the size of the probe volume as well [64]. The length of its long axis, in air, is calculated as

$$l_{p,a} = \frac{d_0}{\sin \alpha_5} = 0.9\,\text{mm}, \tag{2.28}$$

where d_0 is the laser beam diameter at the focal point [65]. Applying the same relation to the laser beam in water yields a longer probe whose length is

$$l_{p,w} = \frac{d_0}{\sin \alpha_7} = 1.2\,\text{mm}, \tag{2.29}$$

where α_7 is the half-beam angle of the laser in water (see Figure 2.20b). If the measurement is performed along "path A, FEP" (Figure 2.4a), the ellipsoidal probe volume is oriented with the longest axis normal to the rods. The longer probe is

more difficult to fit in the centre of the gap with P/D=1.07, where δ=1 mm. This also implies an increased reflection of light from the rod wall. The v'_{rms} measured with the laser light going through the FEP and from the free side of the setup are compared to assess the influence of a longer probe. Figure 2.21 shows that the v'_{rms}

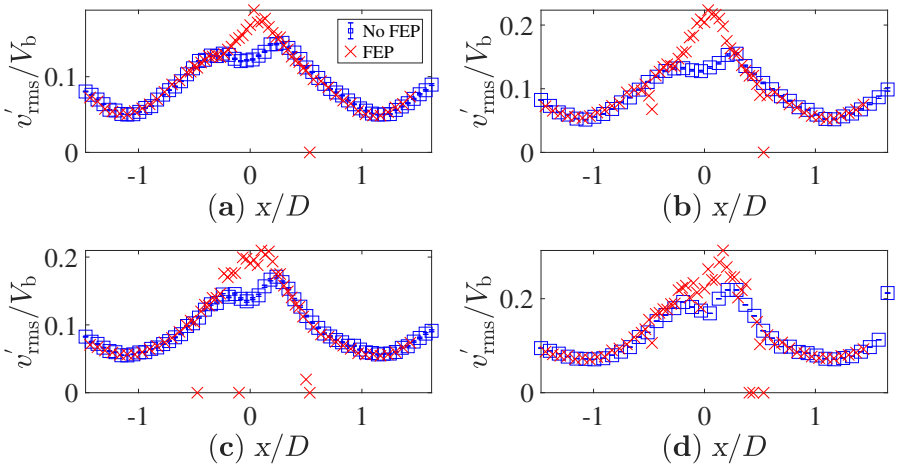

Figure 2.21: v'_{rms}/V_b along "path A, FEP" (×) and along "path A, No-FEP" from the second side (□). a) Re=29 000, b) Re=20 000, c) Re=12 000, d) Re=6500; P/D=1.07.

measured through the FEP rod has a peak at the centre of the gap (×). The light reflected by the rod behind the probe is regarded by the software as particles with near-zero velocity, which increase the deviation around the mean value (the root mean square). The v'_{rms} profiles measured at lower flow rates are shown in Figure 2.22. In these cases the v'_{rms} profile does not show the central peak found at higher Reynolds numbers. Although the light reflection and the elongated probe volume still contribute with near-zero velocity signals, the v'_{rms} is not peaked because the flow velocity closer to zero reduces the statistical deviation from the mean value. With a larger gap (Figure 2.23), reflections are weaker and the probe fits better inside the gap, improving the results.

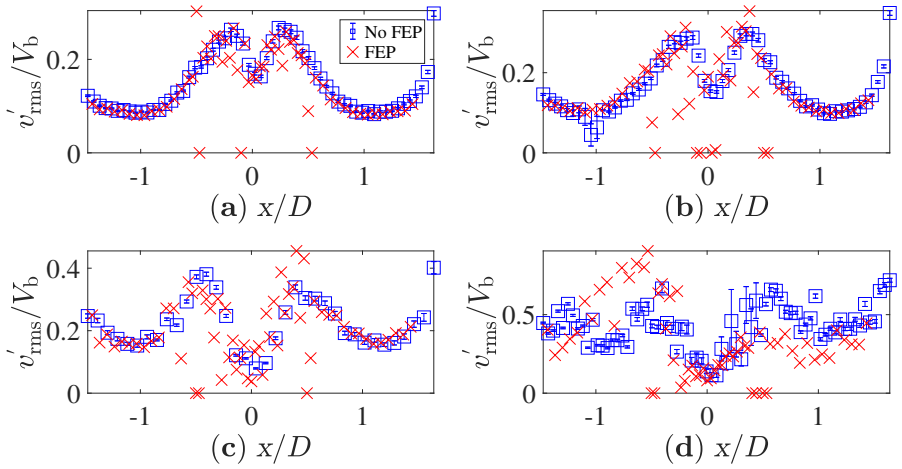

Figure 2.22: v'_{rms}/V_b along "path A, FEP" (×) and along "path A, No-FEP" from the second side (□). a) Re=3600, b) Re=2400, c) Re=1200, d) Re=600; P/D=1.07.

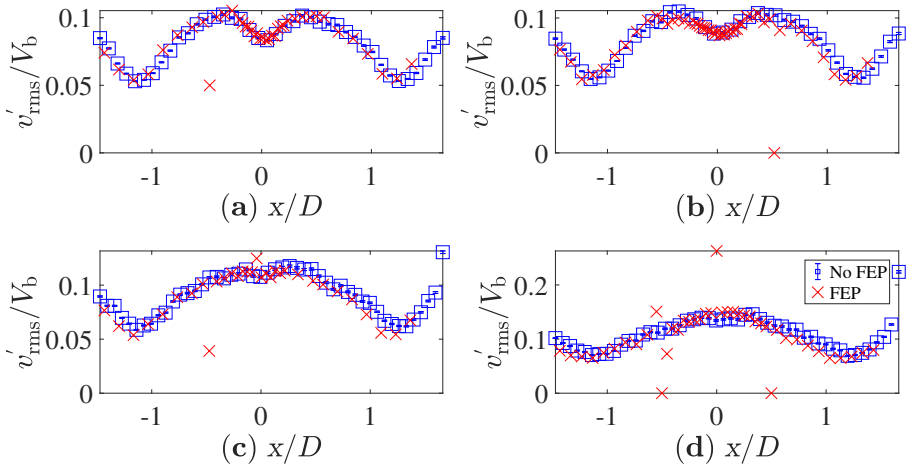

Figure 2.23: v'_{rms}/V_b along "path A, FEP" (×) and along "path A, No-FEP" from the second side (□). a) Re=29000, b) Re=20000, c) Re=12000, d) Re=6500; P/D=1.20.

2.6 Summary

The flow between two half-rods in a square channel was measured by Laser Doppler Anemometry with three P/D ratios and at several Reynolds numbers, ranging from 600 to 29 000. As the flow rate decreased, an additional peak in the root mean square of the stream-wise velocity was found at the centre of the gap. It became clearer and occurred at higher Reynolds values as the gap spacing was reduced. This peak can be ascribed to coherent structures moving through the gap that enhance cross-flow. The power spectrum of the span-wise velocity, measured through the FEP hal-rod, exhibited a peak near the gap centre revealing the presence of such periodical structures in the transversal direction.
The study of the stream-wise velocity component found coherent structures near the gap border whose wavelength is affected by the geometry, and by the Reynolds only when this reaches low values due to the increased velocity difference between the bulk of the flow and the gap region. Moreover, as the Reynolds was decreased, these structures were found also further away from the border inside the main sub-channel, suggesting that coherent structures may grow not only in length, but also in width.
The refraction of the laser beam pairs in water led to an elongation of the laser probe that intensified the light reflection when measuring through the FEP normal to the rods, especially in the middle of the gap. With P/D of 1.20 and 1.13 reflections could be filtered out. However, a P/D of 1.07 led to biased measurements in the centre since the measurement probe came in contact with the rod walls. Nevertheless, the central region of the gap could be properly studied by measuring through the short side of the Perspex casing ("path A-B, No-FEP").

2.7 Nomenclature

Symbols	Description	Units
A	Flow area	m^2
A_{gap}	Flow area considered to estimate the gap Reynolds	m^2
D	Diameter of the half rods	m
D_h	Hydraulic diameter of the channel	m
D_h^*	Hydraulic diameter of the gap region	m
d_f	Fringe distance	nm
d_{Max}, d_{min}	Characteristic length scale of the largest and smallest vortices based on Kolmogorov theory	m
d_0	Laser beam diameter	mm
f_x, f_y	Span-wise (transversal) and stream-wise (vertical) frequency of coherent structures in the flow	Hz
f_D	Frequency of the Doppler burst	Hz
H, L	Dimension of the rectangular channel	m
$l_{p,a}$, $l_{p,w}$	Length of the laser probe volume in air and water, respectively	mm
N	Number of collected samples per LDA measurement point	–
N_{slot}	Number of cross-product allocated within each slot of the autocorrelation function	–
P/D	Ratio between the pitch and the diameter of the half rods	–
P_w	Wetted perimeter	m
Q	Volumetric flow rate	$m^3 s^{-1}$
$R_{i,FEP}$	Inner radius of FEP half-rod	mm
S	Spectrum of the measured time-dependent velocity signal, based on the autocorrelation function	s
t_{FEP}, t_{PMMA}	Thickness of FEP and Perspex wall, respectively	m
u	Span-wise (transversal) velocity component	$m s^{-1}$
u'_{rms}	Root mean square of the span-wise (horizontal) velocity component	$m s^{-1}$
u_τ	Friction velocity	$m s^{-1}$
v	Stream-wise (Vertical) velocity component	$m s^{-1}$
$v_i(t_i)$, $v_j(t_j)$	Velocity samples used in the Slotting technique	$m s^{-1}$
V_b	Bulk velocity	$m s^{-1}$
v_c	Stream-wise (vertical) velocity component in the centre of the gap	$m s^{-1}$
v_{gap}	Stream-wise (vertical) velocity component in the gap region	$m s^{-1}$
v_{in}	Value at the inflection point in the profile of the stream-wise (vertical) velocity component	$m s^{-1}$
v'_{rms}	Root mean square of the stream-wise (vertical) velocity component	$m s^{-1}$
x, y, z	Span-wise (transversal), stream-wise (vertical), and normal directions	m

x_L, x_R	Borders of the flow area where the gap Reynolds is evaluated, along the span-wise (transversal) direction	m
Δx	Lateral refraction of the laser beam	m
X_0	Position of the laser probe volume without refraction	m
z_1, z_2	Borders of the flow area where the gap Reynolds is evaluated, along the normal direction	m

Greek letters	**Description**	**Units**
α_1, α_2, α_3, α_4, α_5, α_6, α_7	Main angles for estimating the refraction of the laser	$^\circ$
δ	Gap width between the half-rods	mm
ε_d	Dissipation rate based on Kolmogorov theory	$m^2\,s^{-3}$
η_{FEP}, η_{PMMA}, η	Refractive indices of FEP, Perspex, and water	–
λ	Average stream-wise (vertical) wavelength of coherent structures	m
λ_{Max}, λ_{min}	Maximum and minimum estimated stream-wise wavelength of coherent structures	m
λ_l	Wavelength of the laser	nm
μ	Dynamic viscosity of water	Pa s
ν	Kinematic viscosity	$m^2\,s^{-1}$
ρ_{ac}	Autocorrelation coefficient	–
ρ	Density of water	$kg\,m^{-3}$
$\sigma_{\bar{v}}$	95% confidence interval of the mean velocity	$m\,s^{-1}$
σ_{rms}	95% confidence interval of the root mean square velocity	$m\,s^{-1}$
σ_y	Width of the Gaussian bell fitting the frequency spectra	Hz
$\Delta\tau$	Time slot of the Slotting technique	s
$\left(\frac{\partial v}{\partial z}\right)_{wall}$	Velocity gradient near the half-rod surface	s^{-1}

Acronyms	**Description**
BWR	Boiling Water Reactor
CANDU	CAnadian Deuterium Uranium
FEP	Fluorinated Ethylene Propylene
FFT	Fast Fourier Transform
LDA	Laser Doppler Anemometry
LMFBR	Liquid Metal Fast Breeder Reactor
PWR	Pressurized Water Reactor

Non dimensional groups	**Description**
Re	Reynolds number
Re_{gap}	Reynolds number of the gap region
Str	Strouhal
Str_{τ}	Strouhal defined as in [12]

Chapter 3

Rod bundle designs and fabrication

3.1 Introduction and motivation

Chapter 2 focuses on a rectangular channel with two half-rods as a preliminary study. The next step, covered by this chapter, is to design an experimental setup resembling more closely the hexagonal rod bundle geometry of the core of a LMFBR. The core of conventional and Gen-IV LMFB reactors consists of a bundle of fuel rods immersed in an axial flow of coolant removing the generated heat. Depending on how tight the coupling of the rods is, such a geometry leads to a velocity difference, and thus to a shear layer between the fluid in the gap and in the main subchannels of the bundle, causing coherent structures in the flow (vortex streets). As mentioned in the introduction to this thesis, these large coherent structures can lead to vibrations of the internal components, especially the rods, due to the pressure fluctuations they cause. These vibrations can damage the rods by fretting [66] and fatigue. This phenomenon is of even higher importance in a LMFBR whose fuel rods are more tightly packed than those of a conventional light water reactor. SEEDS-1 (SEven rods Experiments in Delft for Sesame) will serve as the experimental facility dedicated to study large coherent structures and the related vibrations that they may induce inside a hexagonal rod bundle. The optical measurement techniques used in the SEEDS-1 experiment will be LDA for the flow measurements and a high-speed camera for the vibrations of the rods. A second point of concern in an LMFBR is that the fuel rods do not obstruct the flow locally by touching each other by bending. This is achieved by winding a wire spacer around each rod following a helicoid path. On top of the the spacer function, the wire partially leads the coolant through the gaps between the fuel pins, enhancing the mixing. In this way hot spots can be avoided on the cladding of the fuel pins, improving the safety of the reactor. The flow between neighbouring subchannels strongly depends on the position of the wire, as shown in [32]. Although the main effect of the wire is to direct the flow towards the gaps, a transversal flow

moving against the wrapping path can also occur, which is known as *migratory flow* [44]. The physics of such a flow behaviour is not yet fully understood. Therefore, a second facility, SEEDS-2, will be dedicated to optical measurements of the flow inside a wrapped-wire hexagonal bundle by means of PIV. Although the two facilities serve different functions, the two designs have, to some extent, similar requirements. Both bundles consist of seven rods and water is the working fluid since it is cheap and transparent to light. The P/D ratio should be small enough to cause enough shear between the gap and the subchannel regions to have coherent structures to occur in the flow. The flow of both the facilities should also reach a fully developed, turbulent condition before entering the measurement section, so sufficient development length has to be taken into account. The measurements will be carried out with LDA, a high-speed camera, and PIV, which are optical measurement techniques. The location of the measurements has also to be optically accessible and the light refraction due to the different media should be minimised as much as possible. The next sections of this chapter will discuss the main aspects of the SEEDS experimental designs, detailing the technical expedients adopted to overcome possible issues during the fabrication of some key components, such as the optical window and the wire.

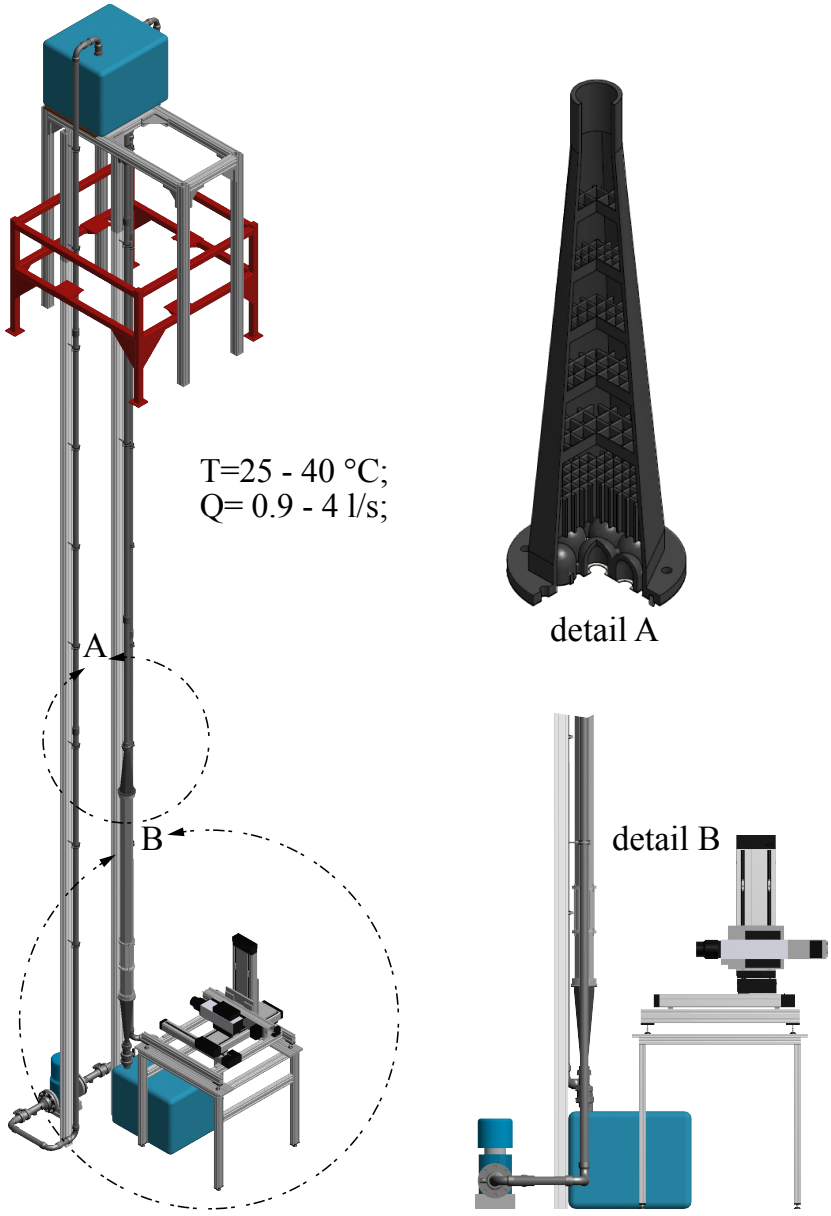

Figure 3.1: SEEDS experimental loop: the water flows from the upper vessel, enters the hexagonal bundle via a flow distributor (detail A) to reach the measurement location (detail B).

3.2 Design requirements

3.2.1 Pitch-to-diameter ratio

The P/D ratio defines the hexagonal lattice of the bundle and dictates the shape of the velocity profile throughout the gap region which, in turn, characterises the coherent structures in the flow. The velocity difference between the low-speed region of the gap and the bulk flow inside one of the main subchannels produces a shear layer that may induce coherent structures along the borders of the gap between the rods [17]. A lower P/D ratio corresponds to a larger velocity difference between the gap and the bulk region, which can trigger coherent structures in the flow. Their interaction with some components of the bundle is the purpose of the SEEDS-1 experiment. As the gap between the rods becomes smaller, the wire spacers cover a relatively larger area of the subchannels, affecting the surrounding flow. This is the subject of study for the SEEDS-2 experiment. However, a low P/D means a more tight lattice, making the optical access for the measurements more difficult inside the inner subchannels. The low value of the P/D ratio is, thus, a trade-off between a geometry that fosters coherent structure and the need for optical access inside the setup. CFD has shown that coherent structures are expected to occur inside a hexagonal rod bundle with a P/D of 1.1 [67, 68], so the P/D of both the facilities is set accordingly to 1.11.

3.2.2 Flow development length

Both SEEDS-1 and SEEDS-2 test sections are installed in a loop where water is the working fluid, at ambient pressure. The flow is gravity-driven from an upper vessel to avoid any vibration induced by the pump. The water enters the test section through a 3D-printed flow distributor (Figure 3.1, detail A). This component has a dual function: it distributes the water among the subchannels of the bundle and it breaks the large vortices that may have formed in the downcomer pipe by means of an internal framework of ribs. Flow detachment from the walls of the distributor is avoided adopting a divergent angle of 4° [69]. Reaching fully developed turbulent flow conditions requires some development length between the flow distributor and the measurement section of the bundle. This length is evaluated considering the hydraulic diameter of a near wall subchannel (edge subchannel) since this, of all the three types of subchannel, has the largest hydraulic diameter. The development length is estimated as [70]

$$\mathrm{L_{dev}} = 4.4 D_{\mathrm{h,e}} {Re_{\mathrm{e}}}^{1/6} \approx 0.3\,\mathrm{m} \tag{3.1}$$

where $Re_{\mathrm{e}}=40\,000$ and $D_{\mathrm{h,e}}=12.7\,\mathrm{mm}$ is the hydraulic diameter of an edge subchannel, evaluated as $4A/P_{\mathrm{w}}$. On top of fully turbulent conditions, coherent structures also need to develop before reaching the measurement region (Figure 3.1, detail B). Therefore, the development length is increased by a factor five, based on CFD evidence [67], to $\mathrm{L_{dev}}=1.5\,\mathrm{m}$.

3.2.3 Optical access

The employed optical measurement techniques require optical access inside the bundle near the central rod, so the components of the bundle must have the same refractive index as water to minimize distortion of the light. For this purposes the refractive index-matching (RIM) technique is applied. This has become a widely used solution for performing optical measurements in rod bundles. Dominguez followed such a method for his measurements inside a 3×3 and 5×5 square rod bundle [71, 72]. More recently experiments performed at Texas University made use of the RIM technique with a larger 61-pins hexagonal bundle [35, 34]. Two possible applications of such a technique are investigated. The first has the rods of the bundle made of Perspex and the water's refractive index is adjusted to the Perspex's by adding some salt (F2S for conciseness [73]). This option was discarded as too much salt should be added, leading to corrosion of the metal parts of the loop such as the pump. The study leading to this conclusion is provided in Appendix B. Other chemical compounds can also be employed to adjust the refractive index of water, such as para-cymene (1-methyl-4-(propan-2-yl)benzene) [72, 74] to match the refractive index of the structural components of the bundle. The second option is to use FEP similarly to what is described in Chapter 2 (S2F for conciseness [73]). Part of the metal of the outer rods is removed and a FEP tube is used instead. FEP is one of the refractive-index matching materials, together with Mexflon-DC employed by Sato [32], commonly used for this kind of applications [75, 76]. The FEP tube is slid over each of the outer rods and heat-shrunk in order to adhere firmly (Figure3.2a). However, FEP would not retain the cylindrical shape during the heat treatment; in fact it would form wrinkles. So, some disposable molds of a water-soluble resin, namely PVA (Polyvinyl alcohol), are placed inside the space left by the metal of the rod (Figure 3.2b) before heating. As a last step, the molds are dissolved by rinsing the inside of the rod with water (Figure 3.2c). The outer radius of the metal rods is reduced by the FEP wall thickness, hence there is no step in the transition between the stainless steel and FEP. The rods are filled with water to further decrease the refraction and to balance the external pressure.

3.2.4 Monitoring systems

The read-out signals of the loop are the temperature of the fluid and the flow rate. An in-house heat exchanger removes the heat generated by the pump (the one that pumps the water from the lower reservoir to the upper reservoir) keeping the water temperature constant. This heat exchanger consists of two concentric tubes in which the water of the loop and of the external cooling system flow separately. The temperature is monitored by a thermocouple (Labfacility, type K) in the upper reservoir. The water falls by gravity and a centrifugal pump (Duijvelaar Pompen, type DPVF 40/1 B) circulates the fluid from the lower to the upper reservoir. The flow rate is read out by three flowmeters: one with a floating element, a magnetic flow meter (ABB MagMaster), and an ultrasonic sensor (B. M. Tecn. Industriali, type TTFM100 NG). The flow is regulated by a valve with linear response (Ebora) placed downstream the upper reservoir. A feedback mechanism implemented in LabVIEW (National Instruments, 2012) adjusts the pump's rotation speed so that

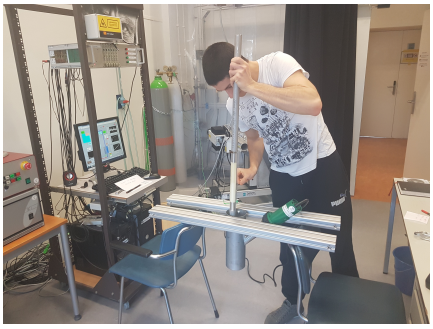

(a)

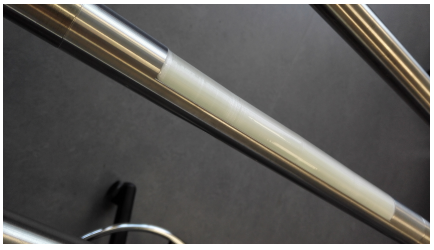

(b)

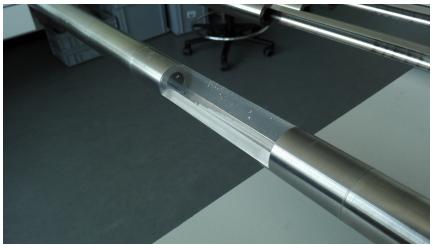

(c)

Figure 3.2: a) Heat-shrinking of FEP: quite often experiments require a generous amount of craftmanship. b) PVA mold to keep the cylindrical shape of the FEP layer upon heat treatment. c) Final product: the PVA mold is dissolved by rinsing the inner rod with water.

the water level is kept constant in the lower vessel.

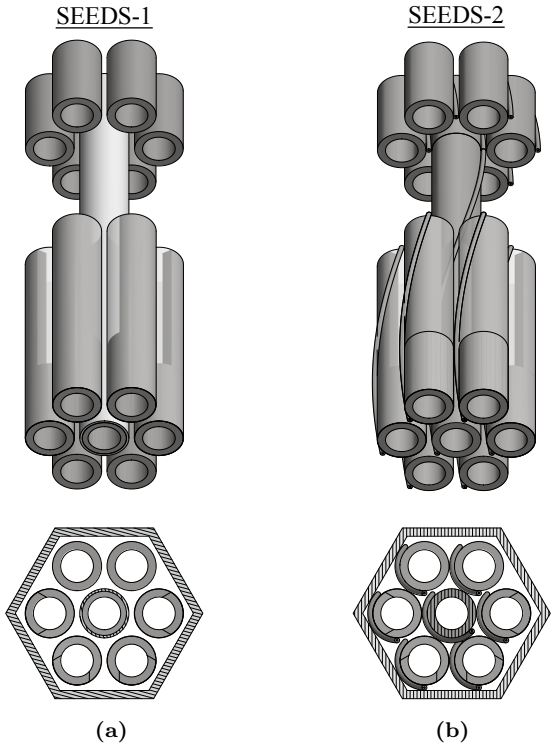

Figure 3.3: Measurement section for SEEDS-1 (a) and SEEDS-2 (b) experiments: four of the outer rods are partly made of FEP to provide optical access around the central rod. For clarity, the outer rods are removed to show the central rod.

3.3 SEEDS-1 rod bundle for FSI experiments

The purpose of SEEDS-1 is to study coherent structures forming in the flow through a tightly-packed hexagonal rod bundle, and to investigate the fluid-structure interaction (FSI) between such periodical structures and the central rod of the bundle. Part of the central rod consists of a cylinder of silicone rubber, fairly common as material in FSI experiments [77, 78], where the interaction between the fluid and the rod is to be studied. Resonance, and its resulting increased vibration amplitude, can be induced if the large vortices occurring in the flow have a size comparable to the dimension of the pin [79]. Hence, the length of the silicone rod has to be comparable with the expected wavelength of coherent structures. CFD has shown that coherent structures with a length of $7\,\mathrm{cm}$ are expected in a rod bundle with the same P/D ratio of SEEDS and a rod diameter of $25\,\mathrm{mm}$[67], so the length of the silicone rod is set to $10\,\mathrm{cm}$. The main geometrical parameters of the bundle are listed in the following table. The measurement section of SEEDS-1 hexagonal bundle is sketched in Figure 3.3a where the outer rods are partially removed to make the central silicone rod visible.

Table 3.1: SEEDS-1 dimensions. D: outer rod diameter, D_{in}: inner rod diameter; P/D: pitch-to-rod diameter ratio, W/D: nearest wall distance-to-rod diameter ratio, $D_{sil,o}$: outer silicone rod diameter, t_{sil}: silicone rod wall thickness, L_{sil}: silicone rod length.

Parameter	Value	Dimension
D	30.0 ± 0.1	mm
P/D	1.11	
W/D	1.11	
D_{in}	20	mm
$D_{sil,o}$	30	mm
t_{sil}	1.5 ± 1.0	mm
L_{sil}	100 ± 5	mm

3.4 SEEDS-2 wrapped-wire rod bundle

The goal of SEEDS-2 is to generate experimental results by means of PIV and to provide an explanation of the flow behaviour near to the wire. SEEDS-2 is a 7-rods hexagonal bundle with helicoid wire spacers wrapped around the rods (Figure 3.3b). The length of the optical Perspex window of FEP is half of the wrapping pitch h: the measurements can cover half of the circumference. At the same time, the FEP window is kept as short as possible to keep the FEP as stiff as possible. The main geometrical parameters of the bundle are listed in the following table.

Table 3.2: SEEDS-2 dimensions. D: outer rod diameter, D_{in}: inner rod diameter; P/D: pitch-to-rod diameter ratio, W/D: nearest wall distance-to-rod diameter ratio, D_w: wire diameter, h: wire wrapping pitch, γ: helicoid pitch angle with the vertical axis.

Parameter	Value	Dimension
D	30.0 ± 0.1	mm
D_{in}	20	mm
P/D	1.11	
W/D	1.11	
D_w	3.0 ± 0.5	mm
h	400	mm
γ	13	$^\circ$

3.4.1 Positioning of the wire

The positioning of the wire is critical for a succesful experiment as any asymmetry in its position would deeply bias the experimental results. The wire is a stainless steel tube with a diameter of 3 mm wound around each of the seven rods of the bundle. There are two issues concerning its positioning: the first is that the wire cannot be glued nor welded along the FEP sleeve of the outer rods because glue will not attach to FEP, and welding will deteriorate it. Secondly, welding the wire along the entire length of the rod would produce large heat-affected zones (HAZ), leading eventually to strong deformations or even rupture of the wire itself. Moreover, the amount of welding beads must be as little as possible to not affect the flow behaviour too much. The adopted solution is to 3D print several cylindrical plastic guides with a notch on the lateral surface that follows the winding path of the wire (Figure 3.4a). These guides are assembled in series and slid over the rod; then the wire is positioned inside the notch and welded at few points along the path (Figure 3.4b). In this way the nominal position of the

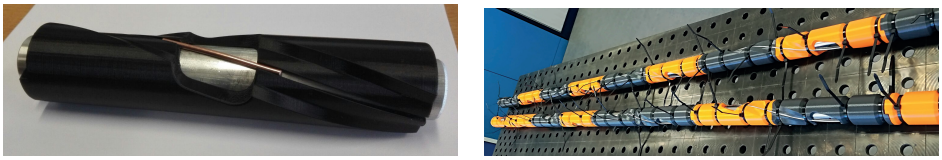

(a) **(b)**

Figure 3.4: a) Sample of a 3D-printed guiding tube with a notch to keep the wire in position during the welding. b) Multiple guides holding in position the wires around two rods.

wire is followed avoiding to weld the whole wire. Since the wire is very thin, it can break rather easily while welding. However, if a hollow wire is used, less heat is required, resulting in a faster welding and smaller HAZ.

3.5 Summary

Two hexagonal rod bundles were designed and assembled, applying the refractive-index matching technique to provide optical access during the measurements. The two bundles are almost identical, but have few differences: SEEDS-1 has a section of the central rod made of flexible silicone rubber to detect flow-induced vibrations, whereas SEEDS-2 has wires wrapped around each rod to more closely mimick the core of a liquid metal reactor and to measure the effect on the surrounding fluid. Both the designs can work within the fluid temperature range $20 - 40\,°\mathrm{C}$ and the maximum achievable Reynolds number (based on the total bundle flow area) is 28 000 (SEEDS-1) and 24 000 (SEEDS-2).
Laser Doppler Anemometry and high speed camera measurements will be performed in SEEDS-1 to study flow structures and vibrations, respectively. Particle Image Velocimetry will be used in SEEDS-2 to study the wire's effect on the flow.

3.6 Nomenclature

Symbols	Description	Units
A	Flow area	m^2
$D_{h,e}$	Hydraulic diameter of the edge subchannel	m
D	Rod diameter	m
D_{in}	Inner rod diameter	m
$D_{sil,o}$	Outer diameter of the silicone rod	m
D_w	Wire diameter	m
h	Helicoid wire pitch	m
L_{dev}	Development length	m
L_{sil}	Silicone rod length	m
P/D	Ratio between the pitch and the diameter of the rods	–
P_w	Wetted perimeter	m
Q	Volumetric flow rate	$m^3\,s^{-1}$
T	Temperature of the water	°C
t_{sil}	Silicone wall thickness	mm
W/D	Nearest wall distance-to-rod diameter ratio	–

Greek letters	Description	Units
γ	helicoid pitch angle with the vertical axis	°
η_{PMMA}, η_{sol}	Refractive indices of Perspex, and of a generic solution	–
$\eta_{sol,L}$	Refractive index of a solution based on Looyenga expression	–
$\eta_{sol,LL}$	Refractive index of a solution based on the Lorentz-Lorenz expression	–
ϕ_i, ϕ_{sol}	Molar volume	$m^3\,mol^{-1}$

Acronyms	Description
CFD	Computational Fluid Dynamics
CsI	Caesium Iodide
CsCl	Caesium Chloride
FEP	Fluorinated Ethylene Propylene
FSI	Fluid-structure interaction
F2S	Matching fluid's to solid's refractive index
Gen-IV	Fourth generation of nuclear reactors
HAZ	Heat-affected zone
KI	Potassium Iodide
KSCN	Potassium Thiocyanate
LDA	Laser Doppler Anemometry
LMFBR	Liquid Metal Fast Breeder Reactor

PIV	Particle Image Velocimetry
PVA	Polyvinyl alcohol
RIM	Refractive Index Matching
SEEDS-1	SEven rods Experiments in Delft for Sesame-1
SEEDS-2	SEven rods Experiments in Delft for Sesame-2
S2F	Matching solid's to fluid's refractive index

Non dimensional groups	**Description**
Re_e	Reynolds number of the edge subchannel

Chapter 4

Fluid-structure interaction in a 7-rods hexagonal bundle

4.1 Introduction and motivation

The rod bundle geometry of the fuel elements forming the core of a LWR or a Gen-IV LMFBR may trigger large coherent structures in the axial flow of coolant [76, 17, 16]. These periodical vortices interact with the surrounding structural components and may cause flow-induced vibrations (FIV) on the fuel rods, by imposing a fluctuating pressure field on these elements. There are reports of FIV-related accidents in nuclear reactors that happened in the past. In his review, Blevins [80] describes the accident occurred to a gas-cooled Magnox reactor in UK where some tubes of the heat exchanger experienced extreme fatigue due to flow-induced vibrations. Another example is the case of the TRIGA (Training Research Isotopes General Atomic) reactor in Korea: vibrations induced on the core by the flowing coolant could even be heard by the operators. A third case that is mentioned regards the sodium-cooled Fermi reactor, where a piece of a conical guide, broken due to vibrations, obstructed the flow into some subchannels leading to a partial meltdown of two fuel elements.
FIV should therefore be avoided because they may lead to damage by fretting and fatigue of the internal components of the reactor core [66]. The fluctuating external force depends on the flow velocity and on the size of these coherent structures. Hence, predicting their wavelength with sufficient accuracy is important for a safer design of the reactor. Currently, there is only one empirical correlation to estimate the stream-wise length λ of these flow structures provided by Guellouz and Tavoularis [19] for a rod inside a rectangular channel and immersed in an axial

The content of this chapter has been published in *Int. J. Heat Fluid Fl.* **79** (2019). DOI:10.1016/j.ijheatfluidflow.2019.108443

flow:

$$\frac{\lambda}{D}=18.7\frac{D+\delta}{D}-16.3, \tag{4.1}$$

where δ is the gap width between the rod and and the outer channel's wall.
However, its applicability to more complex geometries with different shape of the gap region, such as rod bundles, is rather limited.
There is abundance of studies regarding flow-induced vibrations either on solitary cylinders or rod bundles [27, 81, 66, 77], involving a axial or transversal flows. In the latter case, vibrations induced by periodical vortices have also been investigated due to the implications at industrial level [82].
However, an experimental study of the role that coherent structures play in Fluid-Structure Interactions (FSI) inside rod bundles is missing. Furthermore, a correlation for estimating the length of the coherent structures applicable to different geometries would contribute to designing safer components not subject to resonance.
The aim of the work described in this chapter is twofold. It proves a new general correlation to estimate the size of the structures in different channel geometries and it characterises the response frequency of the flexible, central rod of a rod bundle as a function of the frequency of the detected large coherent structures.
The employed measurement systems are Laser Doppler Anemometry (LDA) and a high-speed camera for measuring the flow and the vibrations of the flexible rod, respectively. The experimental setup is SEEDS-1, which is a 7-rod hexagonal bundle where part of the central rod is made of silicone to be flexible. A description of the setup is provided in Chapter 3. LDA measurements of the flow field are done to characterise the vortex streets in the considered geometry, followed by a measurement campaign with the high-speed camera to detect flow-induced vibration of the rod. The small size of this work's bundle allows for an easier optical access around the central rod, which is crucial for measuring vibrations. The optical access around the central rod is achieved through the refractive-index matching technique (RIM): the hexagonal casing is made of Perspex and part of the steel of the rods is replaced with FEP, which matches water's refractive index.

4.2 Theory

Evaluating the natural frequency of the central flexible rod of the bundle is needed for interpreting part of the results of the measurements. This section provides the theoretical background that makes this possible. The second part of the section describes how a new correlation is derived to estimate the wavelength of coherent structures occurring in the flow.

4.2.1 Solitary cylinder case

Estimating the natural frequency of the silicone rod is required to interpret the results of the FSI measurement campaign. The Euler-Bernoulli beam theory for a single cylinder clamped at both ends, immersed in a steady, axial flow, and

surrounded by an outer circular channel, gives the equation originally derived by Paidoussis [27]:

$$\begin{aligned} \mathrm{EI}\frac{\partial^4 x}{\partial y^4} + \mathrm{m_a}\left(v^2\frac{\partial^2 x}{\partial y^2} + \frac{\partial^2 x}{\partial t^2}\right) - \frac{1}{2}C_\mathrm{T}\frac{\mathrm{m_a}v^2}{D}\left(\frac{1}{2}\mathrm{L_{sil}} - y\right)\frac{\partial^2 x}{\partial y^2} + 2\mathrm{m_a}v\frac{\partial^2 x}{\partial y \partial t} + \\ + \frac{1}{2}C_\mathrm{N}\frac{\mathrm{m_a}v}{D_\mathrm{sil,o}}\left(v\frac{\partial x}{\partial y} + \frac{\partial x}{\partial t}\right) + C_\mathrm{V}\frac{\partial x}{\partial t} + \mathrm{m_{sil}}\frac{\partial^2 x}{\partial t^2} = 0 \end{aligned} \tag{4.2}$$

where E=1 MPa is the Young's modulus of the silicone, $\mathrm{I}=\frac{\pi}{4}\left(D_\mathrm{sil,o}^2/4 - D_\mathrm{sil,i}^2/4\right)$ is the moment of inertia of the silicone rod, being $D_\mathrm{sil,o}$ and $D_\mathrm{sil,i}$ the outer and inner diameter of the silicone rod. x is the rod radial displacement, y is the axial coordinate along the rod, $\mathrm{m_a}$ is the added mass accounting for the additional force exerted by the fluid on the rod while it moves, v is the mean axial flow velocity, C_T is the longitudinal viscous force coefficient whose definition is provided by Hoerner [83], $\mathrm{L_{sil}}$ is the rod length, $C_\mathrm{N}=C_\mathrm{T}$ is the lateral drag force coefficient, C_V is the viscous damping coefficient [84], and $\mathrm{m_{sil}}$ is the rod mass.
The added mass $\mathrm{m_a}$ deserves a closer look since it accounts for the confinement effect given by the proximity of other bodies (i.e. walls, rods) around the silicone rod. The added mass is defined as

$$\mathrm{m_a}=C_\mathrm{m}\cdot\rho\pi\frac{D_\mathrm{sil,o}^2}{4}, \tag{4.3}$$

where the C_m is the added mass coefficient which multiplies the weight of the fluid displaced by the rod in the flow. It represents the confinement effect of an outer channel surrounding the single rod [84, 85, 24]. C_m is a function of the outer diameter of the tube D_o that bounds the flow around the rod. The natural frequency $f_\mathrm{sil,n}$ of the rod is calculated by following the method described by Chen [86] and Paidoussis [24]: Equation 4.2 is first rendered non dimensional and then solved through the Galerkin method.

4.2.2 Rod bundle case

Considering a rod bundle, the effect of the rods surroundings the central one is to confine more the flow: displacing the fluid while the rod oscillates becomes more difficult due to the proximity of the surrounding cylinders. This is taken into account by a virtual additional mass that affects the dynamic of the deformation by changing the rod's natural frequencies. The effect of the surrounding rods is to increase the added mass via the added mass coefficient C_m, thereby decreasing the natural frequency. In a rod bundle there are multiple surrounding rods in place of an outer channel, therefore D_o has to be adjusted to account for their effect. D_o is evaluated as the hydraulic diameter of the hexagonal duct whose corners are at a distance P (rod pitch) from the centre:

$$D_\mathrm{o}=\frac{4A}{P_\mathrm{w}}=\frac{3\sqrt{3}P^2-\pi D^2}{\pi D}. \tag{4.4}$$

The added mass coefficient is now evaluated following the expression of Pettigrew [85]

$$C_{\mathrm{m}}=\frac{D_{\mathrm{sil,o}}^2+D_{\mathrm{o}}^2}{D_{\mathrm{sil,o}}^2-D_{\mathrm{o}}^2}. \tag{4.5}$$

The natural frequency of the first mode of vibration of the silicone rod is evaluated based on the hexagonal lattice of SEEDS-1 (see table 3.1); the values are plotted in Figure 4.1 as non dimensional quantities. Frequency and velocity are rendered non dimensional with the following substitution [24]:

$$f_{\mathrm{sil,n}}^{*}=f_{\mathrm{sil,n}}\mathrm{L}_{\mathrm{sil}}^2\sqrt{\frac{\mathrm{m_{sil}}+\mathrm{m_a}}{EI}} \quad v^{*}=v\mathrm{L_{sil}}\sqrt{\frac{\mathrm{m_a}}{\mathrm{EI}}}. \tag{4.6}$$

The non dimensional natural frequency decreases to zero when the flow velocity

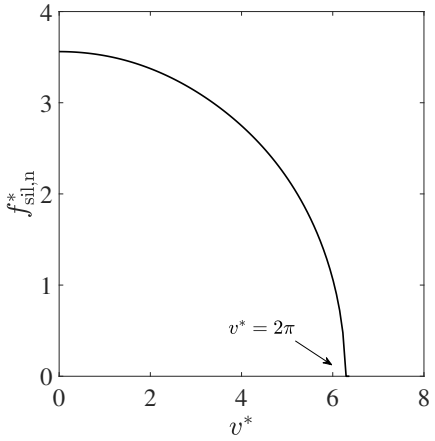

Figure 4.1: Non dimensional 1^{st} mode natural frequency of the silicone rod used for this study as a function of the non dimensional flow velocity. For a clamped-clamped cylinder, the frequency goes to zero at $v^{*}=2\pi$.

reaches the a critical value. For a rod clamped at both ends, as in this work, this happens for $v^{*}=2\pi$.

4.2.3 Empirical correlation derivation

Estimating the wavelength of coherent structures is important for designing experiments that aim at studying specific sizes of flow structures in rod bundles. Ideally, the required correlation should be applicable to as many geometries of the subchannel as possible. Therefore, an empirical correlation for estimating the coherent structure wavelength λ is derived based on dimensional analysis.
λ is assumed to depend on the local channel geometry (i.e. hydraulic diameter of the main subchannel and gap region) and on the fluid properties. The flow velocity

in the gap region and in the main subchannel is also considered. In mathematical terms,

$$\lambda = \mathscr{K}_2 \cdot (D_{\mathrm{h}}^*)^{a_1} \cdot \rho^{a_2} \cdot \mu^{a_3} \cdot v^{a_4} \cdot v_{\mathrm{gap}}^{a_5} \cdot D_{\mathrm{h}}^{a_6}, \tag{4.7}$$

where $\mathscr{K}_2$ is an arbitrary constant, D_{h}^* is the hydraulic diameter of the gap region (defined in figure 4.2), ρ is the fluid density, μ is the dynamic viscosity, and v is the fluid velocity in the main subchannel, v_{gap} is the fluid velocity in the gap region, and D_{h} is the hydraulic diameter of the main subchannel. Based on Buckingham's π theorem [88], the wavelength λ can be expressed by means of three non dimensional groups. From dimensional analysis, it follows that

$$[\mathrm{m}] = [\mathrm{m}]^{a_1} \left[\mathrm{kg\,m^{-3}}\right]^{a_2} \cdot \left[\mathrm{kg\,m^{-1}\,s^{-1}}\right]^{a_3} \cdot \left[\mathrm{m\,s^{-1}}\right]^{a_4} \cdot \left[\mathrm{m\,s^{-1}}\right]^{a_5} \cdot [\mathrm{m}]^{a_6}. \tag{4.8}$$

The associated system of equations

$$\begin{cases} a_1 - 3a_2 - a_3 + a_4 + a_5 + a_6 = 1 \\ a_2 + a_3 = 0 \\ -a_3 - a_4 - a_5 = 0 \end{cases} \tag{4.9}$$

leads to the following expression:

$$\frac{\lambda}{D_{\mathrm{h}}} = \mathscr{K}_2 \cdot \left(\frac{D_{\mathrm{h}}^*}{D_{\mathrm{h}}}\right)^{a_1} Re^{a_2} \left(\frac{v_{\mathrm{gap}}}{v}\right)^{a_5}. \tag{4.10}$$

At high Reynolds numbers it is reasonable to assume that the pressure drops through the gap region $[\Delta p]_{\mathrm{gap}}$ and through the main subchannel $[\Delta p]_{\mathrm{ch}}$, across the length L of the bundle, are equal. Expressing the pressure drops by means of the Darcy-Weisbach equation, it follows that

$$[\Delta p]_{\mathrm{gap}} = \frac{\rho}{2} v_{\mathrm{gap}}^2 \frac{L}{D_{\mathrm{h}}^*} \mathrm{f}_{\mathrm{gap}}(Re_{\mathrm{gap}}) = [\Delta p]_{\mathrm{ch}} = \frac{\rho}{2} v^2 \frac{L}{D_{\mathrm{h}}} \mathrm{f}_{\mathrm{ch}}(Re), \tag{4.11}$$

where the friction coefficients are expressed as $\mathrm{f}_{\mathrm{ch}}(Re) = C_1 Re^{-\chi_1}$ and $\mathrm{f}_{\mathrm{gap}}\left(Re_{\mathrm{gap}}\right) = C_2 Re_{\mathrm{gap}}^{-\chi_2}$ [89]. From the previous equation, the ratio v_{gap}/v can be expressed as

$$\frac{v_{\mathrm{gap}}}{v} = \left[\frac{\mathrm{f}_{\mathrm{gap}}\left(Re_{\mathrm{gap}}\right)}{\mathrm{f}_{\mathrm{ch}}(Re)} \frac{D_{\mathrm{h}}^*}{D_{\mathrm{h}}}\right]^{1/2}. \tag{4.12}$$

Substituting Equation 4.12 into Equation 4.10 leads to

$$\frac{\lambda}{D_{\mathrm{h}}^*} = \mathscr{K}' \left(\frac{D_{\mathrm{h}}^*}{D_{\mathrm{h}}}\right)^{\xi} Re^{a_2} \mathrm{f}_{\mathrm{ch}}(Re)\, \mathrm{f}_{\mathrm{gap}}\left(Re_{\mathrm{gap}}\right). \tag{4.13}$$

Experimental evidence [59, 19, 17, 76] has shown that the wavelength is independent of the Reynolds number of the main subchannel Re, so $a_2 = 0$ meaning

$$\frac{\lambda}{D_{\mathrm{h}}^*} = \mathscr{K}' \left(\frac{D_{\mathrm{h}}^*}{D_{\mathrm{h}}}\right)^{\xi} Re_{\mathrm{gap}}^{\zeta}. \tag{4.14}$$

This is the most general form of the correlation. It will be tested against the experiments performed in simple geometries such as rectangular channels hosting respectively one or two half-rods [17, 76], and an eccentric rod hosted in a rectangular channel [19]. Furthermore, two rod bundle geometries are considered: the hexagonal bundle of this work and a sector of a circular bundle [87]. The results of the validation with the experiments is discussed in section 4.5.2.

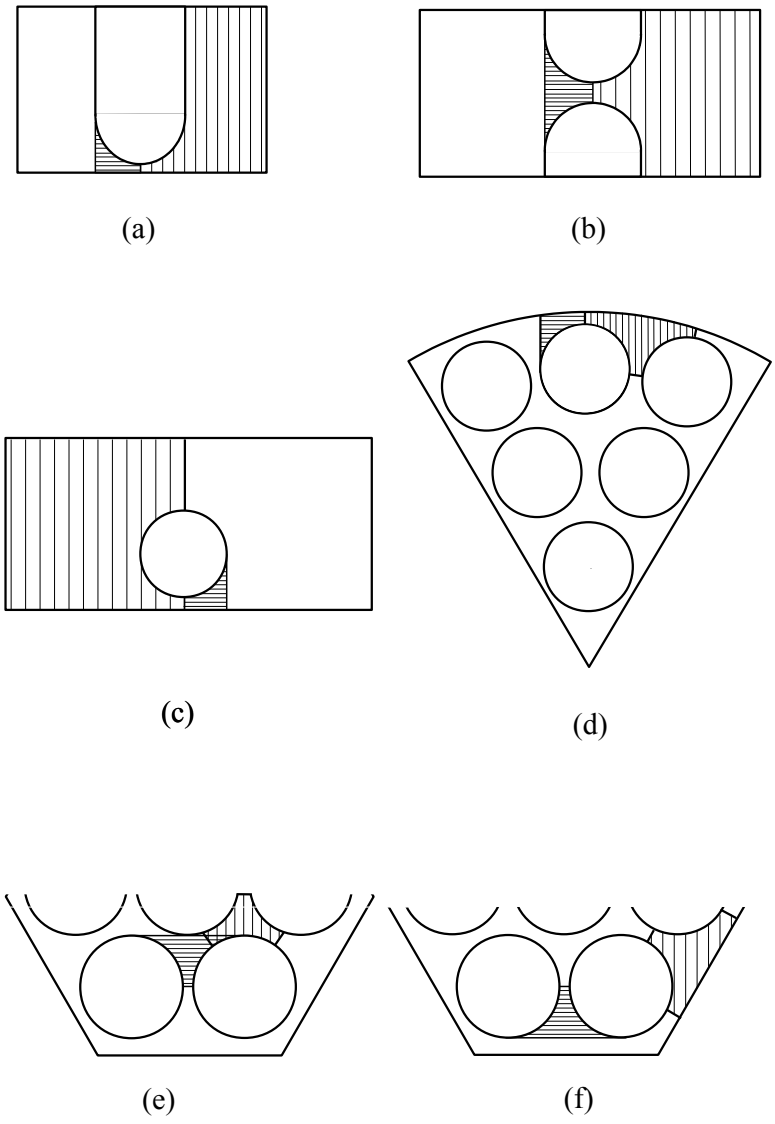

Figure 4.2: Definition of the hydraulic diameters of the gap region for the bundle geometries on which the correlation is to be tested. (a) Adopted from [17]. (b) Adopted from [76]. (c) Adopted from [19]. (d) Adopted from [87]. (e-f) This work. Horizontal hatching: gap region. Vertical hatching: main subchannel. For clarity, the main subchannel and the gap region are drawn as two separate regions whereas, in reality, they partly overlap.

4.3 Experimental apparatus

The measurement systems used to carry out the work described in this chapter are a Laser Doppler Anemometry system (described in section 2.3) for measuring the flow, and a high-speed camera to capture the vibrations occurring on the flexible part of the central rod. Both systems are mounted on and moved by the same traverse. The face of the hexagonal casing through which the measurements are

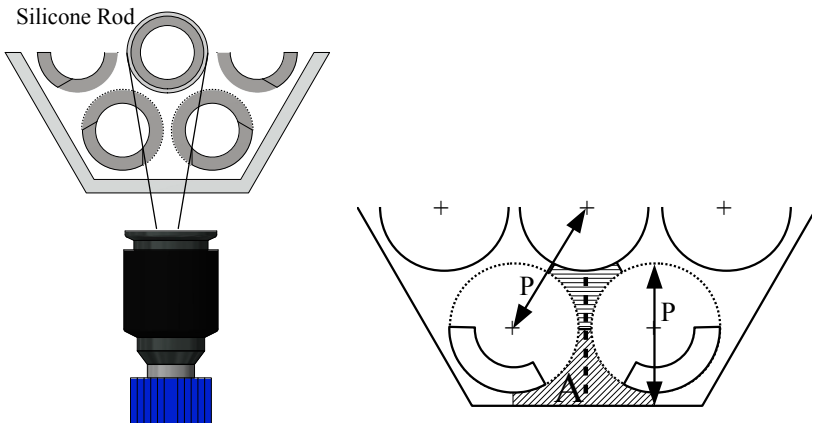

Figure 4.3: a) FIV tracking system for recording the position of one border of the rod. The dashed circular profiles represent the transparent FEP; the rods are filled with water to avoid image distortion through FEP. b) Top view of half of the hexagonal bundle geometry: the straight dashed line represents the LDA measurement path. Horizontal hatching: central subchannel. Diagonal hatching: edge subchannel.

performed is rotated in order to be perpendicular to the measurement systems. The alignment is done with a portable laser installed on the traverse and a reflective metal plate used as target on the casing. The LDA system and the post-processing of the measurements are discussed in Chapter 2, whereas the high-speed camera system is described in the following section.

4.3.1 High-speed camera

The equipment to measure flow-induced vibrations of the silicone rod consists of a Complementary Metal-Oxide Semiconductor (CMOS) camera Imager MX 4M (LaVision, Germany) capable of recording at 180 fps with full resolution (4 MP) with a reduced field of view. The camera cannot have both borders of the rod in focus without losing much spacial resolution: the camera should be placed too far from the target. Thus, only one border of the silicone rod is in focus and 15000 frames at 300 Hz are recorded in each measurement. The Nyquist frequency, being the highest frequency of a signal that can be captured with a given sampling rate,

is defined as half of the sampling frequency of a signal. This high-speed camera allows for a Nyquist frequency of 150 Hz. The frequency of the vibrating silicone rod is expected to be of the same order of the coherent structures' frequency, which is ≈10 Hz based on preliminary LDA measurements. Hence, a recording rate of 300 Hz is considered high enough to measure vibrations induced on the silicone rod.

The silicone appears white in the images and the background contrast with the surrounding fluid is enhanced with a flash light to illuminate the target area, and by keeping the setup in the dark. The recorded frames are post-processed through the Matlab Image Toolbox. The intensity values of the light in each image are converted into ones or zeros with a binary filter that uses a threshold level determined by the Otsu algorithm [90]. The position of the edge of the silicone rod appears, in each frame, as the border between the regions of ones and zeros obtained through the binary filter.

The recorded positions of the silicone rod's edge gives the instantaneous displacement, and its root mean square, on a plane orthogonal to the line of sight of the camera, calculated as follows:

$$\bar{\varepsilon}=\frac{1}{\mathrm{N}}\sum_{i=1}^{N}|\varepsilon(t_i)|\,;\qquad \varepsilon_{\mathrm{rms}}=\sqrt{\frac{1}{\mathrm{N}}\sum_{i=1}^{N}[\varepsilon(t_i)-\bar{\varepsilon}]^2}, \tag{4.15}$$

where $\bar{\varepsilon}$ is the mean displacement, N is the number of recorded frames, $\varepsilon(t_i)$ is the displacement of the i-th frame and $\varepsilon_{\mathrm{rms}}$ is the displacement root mean square. The recorded time signal of the displacement is filtered with the Henderson's 23 points moving average to reduce the noise at high frequency, following the approach of Cioncolini *et al.* in a similar work [91]. The time signal of the displacement is used as input to calculate the frequency spectrum. The first method to calculate the spectrum relies on the autocorrelation function of the displacement (Figure 4.4a), and the dominant peak in the frequency spectrum is fitted with a Gaussian bell (Figure 4.4b). The frequency range where the spectral peak is fitted is determined by the two points where the first derivative of the spectrum goes to zero. The fitting error is expressed as the Normalised Root Mean Square Error (NRMSE):

$$\mathrm{NRMSE}=\frac{\sqrt{\sum_{k=1}^{N_{\mathrm{g}}}[S_{\mathrm{fit}}(k)-S(k)]^2}}{\mathrm{N_g}\bar{S}}, \tag{4.16}$$

where $\mathrm{N_g}$ is the number of fitted points of the peak, S_{fit} and S are the fitted and the measured value of the spectrum, respectively, and $\bar{S}$ is the mean value of S. The error with which the average frequency is determined from the fitting is lower than 2%.

A second way to estimate the spectrum is through the discrete Fourier transform (DFT) of the displacement signal as

$$S=\sum_{j=0}^{M-1}\varepsilon(t_j)\exp(2\pi i t_j f_{\mathrm{sil}}), \tag{4.17}$$

where $\varepsilon(t_j)$ is the j-th recorded displacement sample, f_{sil} is the vibration frequency of the silicone rod, t_j is the j-th time instant in the signal, and i is the imaginary unit. The noise in the spectrum is reduced by means of the Bartlett's method [92] (Figure 4.4c). The noise in the signal, estimated through a no-flow record-

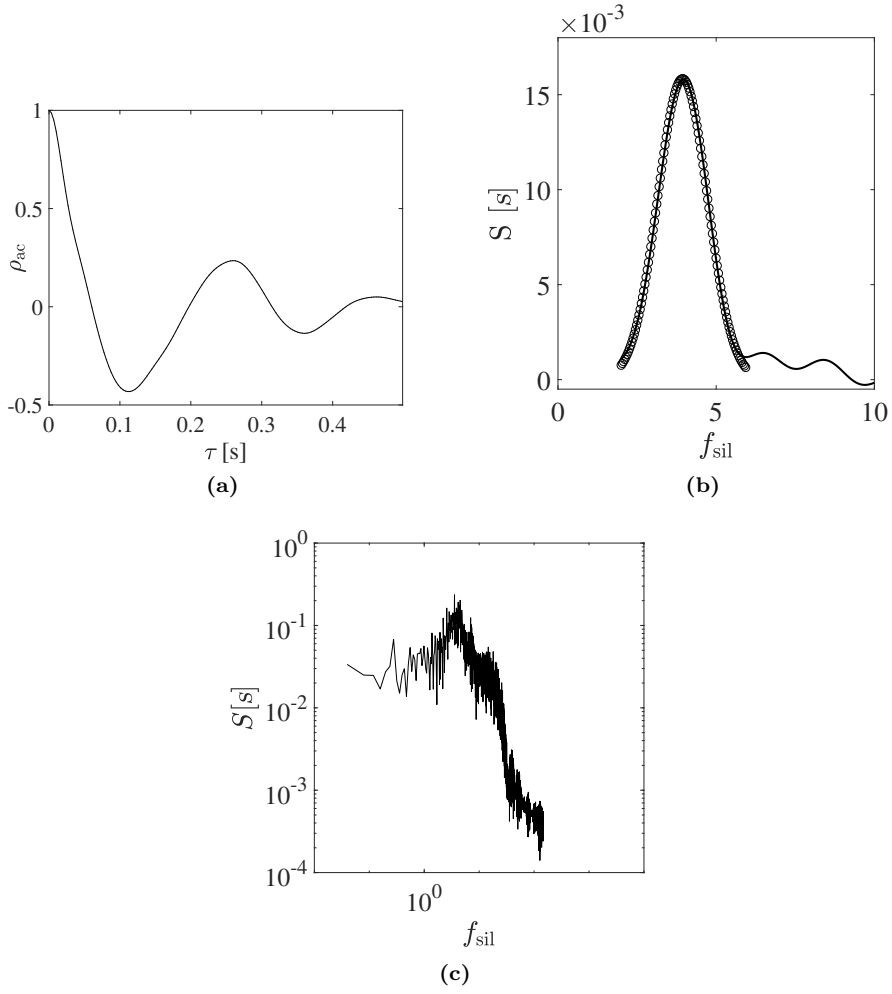

Figure 4.4: a) Autocorrelation function and b) Spectral peak characterising the vibration of the silicone rod fitted with a Gaussian function (◯). c) DFT of the vibrating silicone rod.

ing, corresponds to an equivalent displacement of 3 µm (the minimum measurable displacement is 9 µm).

4.4 Measurement campaign

The LDA measurements are carried out in the edge and central subchannel, so it is more accurate to refer to the Reynolds number of the edge (Re_e) and of the central subchannel (Re_c). Re_e is estimated as

$$Re_e = \frac{\rho \cdot v_e \cdot D_{h,e}}{\mu}, \tag{4.18}$$

where ρ and μ are the density and dynamic viscosity of water, respectively; $D_{h,e}$ is the hydraulic diameter of the edge subchannel, and v_e is the average stream-wise velocity measured inside the edge subchannel. The latter is evaluated through

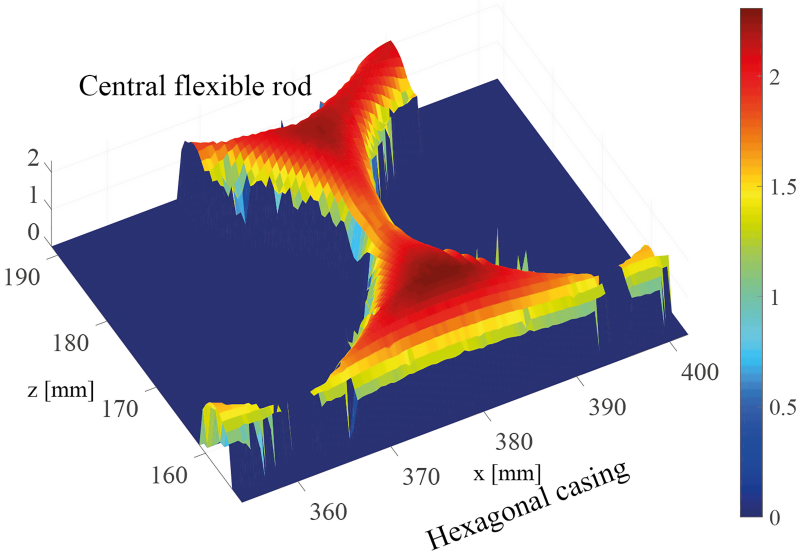

Figure 4.5: Contour plot of the stream-wise velocity component measured with LDA around the two rods close to the outer wall.

LDA measurements of the flow area A belonging to the edge subchannel (Figure 4.3b). The average is calculated as

$$v_e = \frac{1}{A}\int_A v(x,z)dA = \frac{1}{A}\sum_i\sum_j v(x_i,z_j)dA_{ij}, \tag{4.19}$$

where dA_{ij} differs per position.
An example of the results from the LDA measurement of the velocity inside the edge and part of the central subchannel is shown in Figure 4.5. The two regions ($x \approx 160\,\text{mm}; 360\,\text{mm} \leq y \leq 370\,\text{mm}$) and ($x \approx 160\,\text{mm}; y \approx 395\,\text{mm}$) are the most affected by the reflecting metal surface of the rods, hence no velocity value is available. The Reynolds number of the central subchannel, Re_c, is determined based on Re_e. Re_c requires the values of the average stream-wise velocity v_c in the central subchannel.

The pressure drops throughout all the subchannels may be considered the same [89]; in particular the pressure drops through the edge $[\Delta p]_e$ and the central $[\Delta p]_c$ subchannels may be equated and expressed via the Darcy-Weisbach equation [93]:

$$\frac{f_c \rho v_c^2}{D_{h,c}} = \frac{f_e \rho v_e^2}{D_{h,e}}, \tag{4.20}$$

where $D_{h,c}$ is the hydraulic diameter of the central subchannel, and f_c and f_e are the friction factors of central and edge subchannels, respectively. v_c can be obtained from the previous equation. For a bare rod bundle (no spacers) with turbulent flow, f_c and f_e can be expressed as [89]

$$f_c = \frac{C'_{fT,c}}{Re^n}; \qquad f_e = \frac{C'_{fT,e}}{Re^n}, \tag{4.21}$$

where n=0.18, and $C'_{fT,c}$ and $C'_{fT,e}$ are coefficients depending on the hexagonal lattice. This correlation is valid for rod bundles within the pin number range $7-217$ and the associated mean error is as low as 9% [94]. Substituting Equation 4.21 into Equation 4.20 leads to

$$v_c = v_e \cdot \left[\frac{C'_{fT,e} D_{h,c}}{C'_{fT,c} D_{h,e}} \left(\frac{D_{h,c}}{D_{h,e}} \right)^n \right]^{\frac{1}{2-n}}. \tag{4.22}$$

Re_c is finally evaluated as

$$Re_c = \frac{\rho \cdot v_c \cdot D_{h,c}}{\mu}. \tag{4.23}$$

The values of Re_e and Re_c are reported in table 4.1.

Table 4.1: Q: flow rate, Re: Reynolds number based on the bundle's total flow area, Re_e: edge subchannel Reynolds number, Re_c: central subchannel Reynolds number.

$Q\,[\mathrm{m^3\,s^{-1}}]$	Re	Re_e	Re_c
4.78×10^{-3}	27200	48630	36530
3.48×10^{-3}	20620	30540	22940
3.28×10^{-3}	17600	28200	21180
2.92×10^{-3}	15040	26240	19700
2.68×10^{-3}	13060	25130	18800
2.42×10^{-3}	11830	22660	17000
2.13×10^{-3}	10300	20310	15260
1.94×10^{-3}	10100	16620	12490
1.59×10^{-3}	8530	14950	11230
1.31×10^{-3}	6790	12730	9560
1.05×10^{-3}	6470	10100	7580

4.5 Results and discussion

This section presents the experimental results. First, the LDA measurements of the coherent structures occurring in the flow are discussed. The results are used to validate the correlation derived in section 4.2.3 for predicting the wavelength of the flow structures.
The second part focuses on the vibrations measured with the high speed camera on the silicone rod surface and on the influence of coherent structures on the oscillation of the rod wall is discussed.

4.5.1 Coherent structures in the flow

The LDA measurements are carried out at mid-length in the hexagonal Perspex casing sampling several locations in the flow along a straight line going from the outer wall to the central silicone rod. The frequency of passage of the coherent structures through the measurement region is extracted from the frequency spectrum of the stream-wise velocity component. Two additional measurements at the beginning and at the end of the transparent section are performed to check that the coherent structures are fully developed in the flow (i.e. their wavelength does not change through the measurement section).
Figure 4.6 shows the LDA measurement along the straight line throughout the gap between two front rods, with Re_e=30540 (Re_c=22940). The normalised stream-wise velocity component is reported in Figure 4.6a. The velocity root mean square is shown in Figure 4.6b, which features two maxima located at the outer wall and at close to the central rod, where turbulence increases due to the shear produced

by the viscous sublayer, similarly to common wall-bounded flows [53]. The relative maxima closer to the centre gap are due to the shear between the high-velocity region in the bulk and the low-velocity fluid inside the narrow gap.

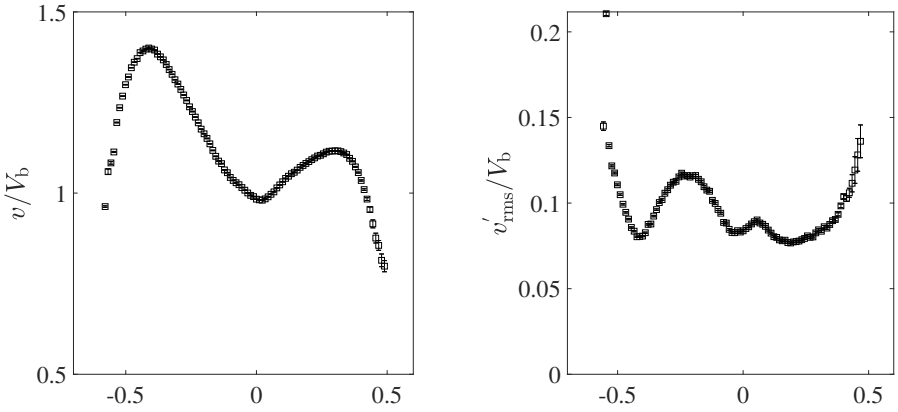

Figure 4.6: Stream-wise velocity profile (a) and root mean square (b) measured with LDA through the gap between two front rods. The abscissa is the distance from the gap centre, normalized to the rod diameter.

Turbulence inside the gap between the two rods closer to the wall is examined based on the turbulence spectrum. The slope of the spectrum carries information on the nature of turbulence, i.e. whether this is two-dimensional or three-dimensional (2D, 3D for short) within the inertial subrange of the spectrum.
This section will focus on the wavelength and the frequency of the coherent structures, which is used to validate an empirical correlation as proposed in section 4.5.2. The measured frequency of passage of the coherent structures is compared with the structural response frequency of vibration of the rod wall, as discussed in section 4.5.3.

For a 3D homogeneous turbulent flow, only the conservation of energy applies and the inertial subrange of the turbulent spectrum usually shows the well-known slope of $-5/3$. The vorticity equation for 3D turbulence and incompressible flow is

$$\frac{D\vec{\omega}}{Dt} = (\vec{\omega}\cdot\nabla)\vec{v} + \nu\nabla^2\vec{\omega}, \tag{4.24}$$

where $\frac{D\cdot}{Dt}$ is the Lagrangian (or substantial) derivative, $\vec{\omega}$ is the vorticity vector and ν is the kinematic viscosity. The first term at the right hand side of the equation accounts for the vortex-stretching, which is the largest if the velocity gradient is parallel to the vorticity vector. In 2D turbulence the vortex-stretching effect is absent [95], hence the general vorticity equation, for incompressible and inviscid fluids, takes the form

$$\frac{D\vec{\omega}}{Dt}=0, \tag{4.25}$$

which states that the vorticity must also be conserved. This additional condition results in a slope of the spectrum equal to -3, within the inertial subrange. The energy cascade is towards larger scales (lower wavenumber), whereas the vorticity cascade is towards the smallest scales in the viscous subrange, contrarily to 3D turbulent flows [96]. The slope of the inertial subrange gives thus an indication of the type of turbulence.

The frequency spectrum of the stream-wise velocity is evaluated in the middle of the gap between the edge and central subchannel. The frequency spectrum is then multiplied by f_y^3 (or $f_y^{5/3}$): following the approach of Romano [97] the resulting function $S\cdot f_y^3$ (or $S\cdot f_y^{5/3}$) should have a flat plateau within the frequency range where turbulence is 2D (or 3D). Figure 4.7a shows the frequency spectrum and Figure 4.7b shows both $S\cdot f_y^3$ and $S\cdot f_y^{5/3}$ for a Reynolds number corresponding to Re_e=12 730 (Re_c=9560). A low-frequency peak is found, which is characteristic of coherent structures that affect periodically the velocity field while moving with the mean flow. Although the spectrum exhibits a -3 slope over a short frequency decade, the overall slope appears to be close to $-5/3$, as shown by the almost flat plateau of the $S\cdot f_y^{5/3}$ plot.

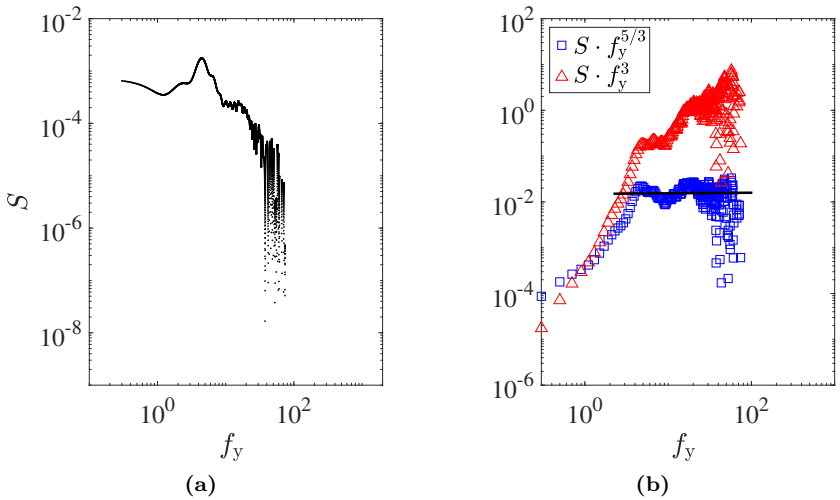

Figure 4.7: a) Frequency spectrum measured at the centre of the gap. b) $S\cdot f_y^{5/3}$ (square), $S\cdot f_y^3$ (triangle). Re_e=12 730. The black line highlights a plateau, indicating three-dimensional turbulence.

Figure 4.8 reports the case with Re_e=14 950 (Re_c=11 230), where the peak in the spectrum is at 5.3 Hz. The slope is close to $-5/3$, as shown by the constant trend of $S\cdot f_y^{5/3}$ in the same frequency range. Figure 4.9 refers to the case with Re_e=48 630

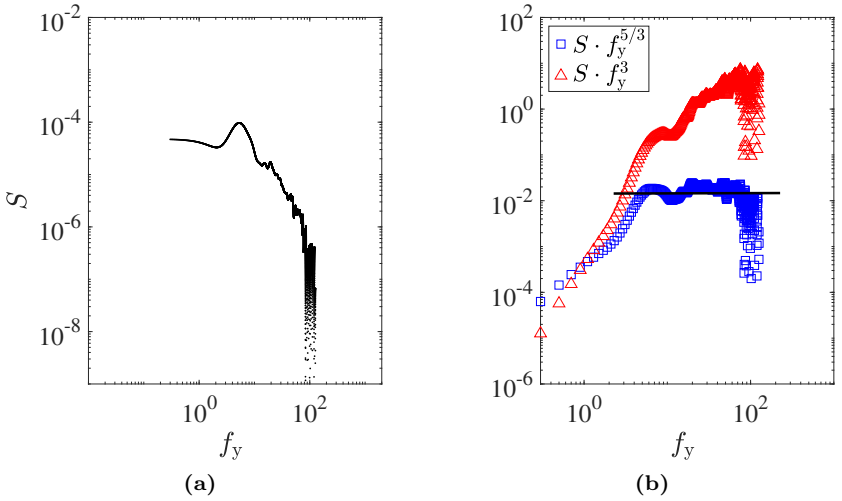

Figure 4.8: a) Frequency spectrum measured at the centre of the gap. b) $S \cdot f_y^{5/3}$ (square), $S \cdot f_y^3$ (triangle). Re_e=14 950. The black line highlights a plateau, indicating three-dimensional turbulence.

(Re_c=36 530), where coherent structures occur at a higher frequency, being 17 Hz (Figure 4.9a). The corresponding plots of $S \cdot f_y^3$ and $S \cdot f_y^{5/3}$ are shown in Figure 4.9b. The spectrum at this Reynolds number has a slope between -3 and $-5/3$. For each flow rate, the turbulent spectra are evaluated along the path going from the edge to the central subchannel (Figure 4.3b). The peaks found in the spectra reveal periodicities at the associated frequency f_y ascribed to structures occurring in the flow. An average frequency of the structures is calculated based on the values given by the single peaks. The plotted quantities are rendered non dimensional following Equation 4.6. The plots of Figure 4.10 report the average non dimensional frequency of the coherent structures f_y^* in both the edge and the central subchannel against the non dimensional flow velocity v^*. An example of the measured velocity signal is shown in Figure 4.10c where the flow oscillations due to coherent structures moving in the flow are visible for Re=10 300. The peaks detected in the frequency spectra of the velocity signals show a bell-shaped distribution of frequencies so every peak is fitted with a Gaussian bell to obtain the corresponding σ_y around the mean. This gives a frequency interval $f_y \pm \sigma_y$ which, in turn, provides a minimum and a maximum wavelength of the structures, as shown in Figure 4.11. The NRMSE resulting from the fitting, and evaluated with Equation 4.16, is lower than 5% for all the considered cases. The wavelength of the coherent structures is evaluated adopting Taylor's hypothesis (coherent structures in the flow are regarded as frozen entities moving with the stream at velocity v_{in}). The velocity v_{in} is the stream-wise velocity measured at the inflection point of the profile between the gap and the subchannels [17]. The average wavelength and its minimum and maximum values are

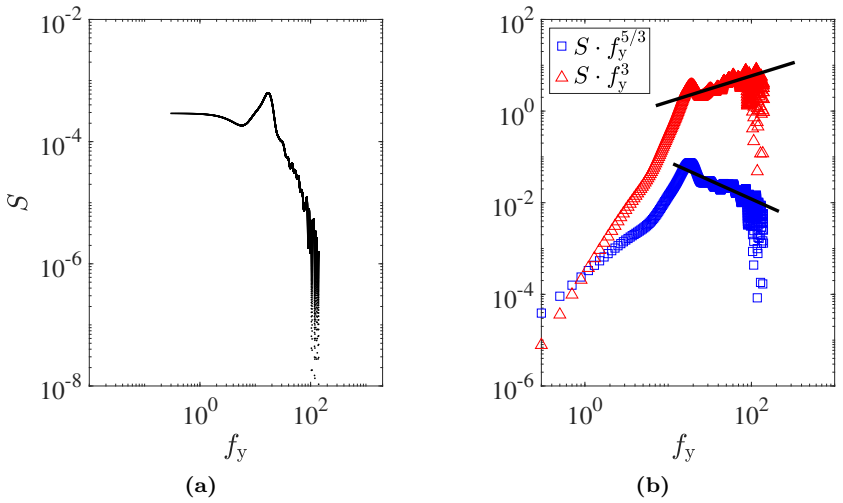

Figure 4.9: a) Frequency spectrum measured at the centre of the gap. b) $S \cdot f_y^{5/3}$ (square), $S \cdot f_y^3$ (triangle). Re_e=48 630.

$$\lambda = \frac{v_{in}}{f_y}; \qquad \lambda_{Max} = \frac{v_{in}}{f_y - \sigma_y}; \qquad \lambda_{min} = \frac{v_{in}}{f_y + \sigma_y}. \tag{4.26}$$

The uncertainty on the wavelength of the structures is estimated through the uncertainty propagation formula as

$$\delta\lambda = \sqrt{\left(\frac{\partial\lambda}{\partial f_y} df_y\right)^2 + \left(\frac{\partial\lambda}{\partial v_{in}} dv_{in}\right)^2} \approx \left|\frac{\partial\lambda}{\partial f_y} df_y\right| = \left|\frac{v_{in}}{{f_y}^2} df_y\right|, \tag{4.27}$$

where the approximation is possible because the error on v_{in} is negligible compared to the uncertainty on f_y. The frequency at which the flow structures pass through the measurement region scales almost linearly with the flow velocity.
Figure 4.11 shows the wavelength of the structures normalised by the gap region hydraulic diameter suggests that, at high Re, the average wavelength is independent of the Reynolds number, confirming previous experimental findings [59, 19, 17, 76]. Recalling the discussion of section 2.5.4 (Chapter 2), if the wavelength of coherent structures can be considered constant within a certain Reynolds interval, the quantity

$$\frac{Re^3}{\varepsilon_d}, \tag{4.28}$$

is conserved within such an interval (ε_d is the turbulent dissipation rate). This means that the turbulent dissipation rate of the flow measured at different Reynolds numbers can be compared.
Considering the lowest and highest Reynolds numbers (based on the total bundle flow area) defining the interval where the wavelength λ can be assumed constant,

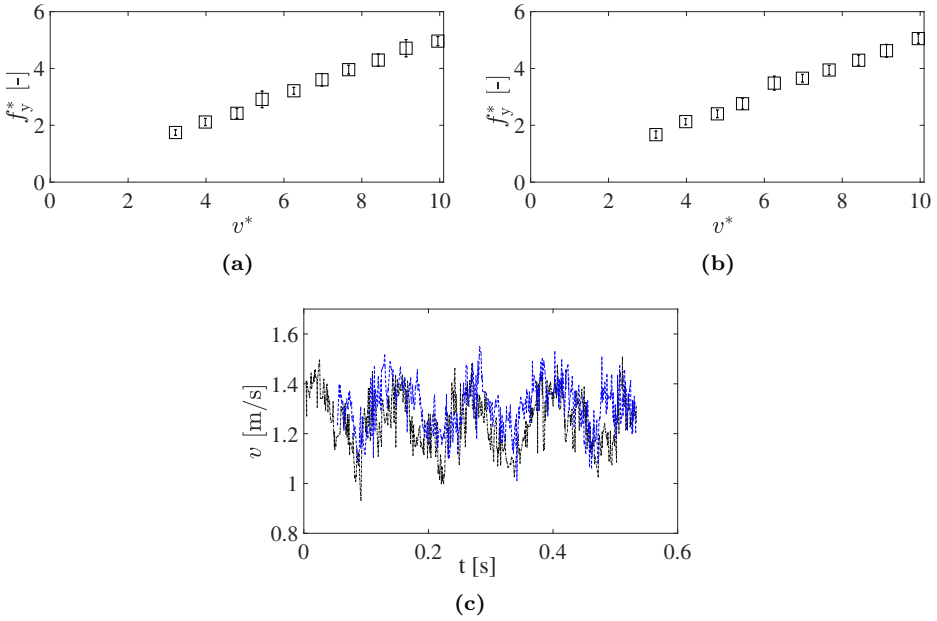

Figure 4.10: Non dimensional mean frequency of passage of the coherent structures f_y^* against the non dimensional velocity v^*, measured (a) between the edge subchannel and the gap, and (b) between the gap and the central subchannel. c) Time-dependent velocity signal of the v component, measured at two locations 2 mm apart close to the centre of the gap connecting the edge to the central subchannel.

the previous expression becomes

$$\left[\frac{Re^3}{\varepsilon_d}\right]_{Re=27200} = \left[\frac{Re^3}{\varepsilon_d}\right]_{Re=6470}, \tag{4.29}$$

from which the turbulent dissipation rate ε_d of the two cases can be compared:

$$\frac{[\varepsilon_d]_{Re=27200}}{[\varepsilon_d]_{Re=6470}} = \left(\frac{27200}{6470}\right)^3 \approx 74. \tag{4.30}$$

This ratio does not change much ($\approx$111) if the edge or central subchannel's Reynolds number is considered, instead of the whole bundle's. The dissipation rate of the flow with a Reynolds of 27200 is approximately a factor 100 higher than with a Reynolds of 6470.

The subject of the next section will be the influence of the geometry of the channel on the structure's wavelength.

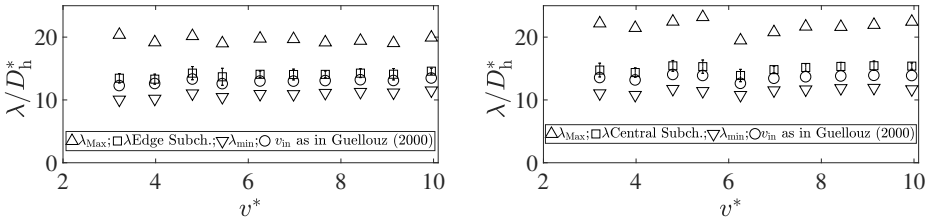

Figure 4.11: (□): Average non dimensional wavelength of the coherent structures λ/D_h^* against the non dimensional velocity v^*, measured (a) between the edge subchannel and the gap, and (b) between the gap and the central subchannel, where D_h^* is defined as in Figure 4.2. (▽) and (△): Estimated maximum and minimum wavelength with Equation 4.26. (◯): Wavelength calculated based on the convection speed provided by Guellouz and Tavoularis [19].

4.5.2 Correlation validation

The correlation derived in section 4.2.3 for predicting the wavelength of coherent structures is now applied to several experimental cases. The predicted (normalised) wavelength λ, evaluated for different geometries, and the results of the experiments are reported in Figure 4.12a against the hydraulic diameter of the gap region D_h^* (see Figure 4.2 for its definition in the considered geometries) normalised by the hydraulic diameter of the subchannel. The figure suggests that λ/D_h^* is constant and approximately equal to

$$\frac{\lambda}{D_h^*} \approx 13, \tag{4.31}$$

The wavelength of the structures scales linearly with the hydraulic diameter of the gap region D_h^*. λ/D_h^* constant means that the exponents in Equation 4.14 should be zero, that is $\xi=\zeta=0$. If one imagines to increase indefinitely the hydraulic diameter of the main subchannel D_h while keeping the gap region unaltered (hence keeping D_h^* and Re_{gap} constant), the wavelength of the structures forming close to the gap should not change much. This means that at some point λ/D_h^* will not depend on $(D_h^*/D_h)^\xi$ any more, so it is reasonable to assume that

$$\xi=0 \quad \text{for} \quad \frac{D_h^*}{D_h} \lesssim 1. \tag{4.32}$$

We see that the correlation is valid even for $D_h^*/D_h=1.15$, which is the case of the near wall subchannel of this work's bundle (Figure 4.2f). The practical meaning of $D_h^*/D_h \lesssim 1$ in a bundle is that the rod are moved farther (Figure 4.12b). In the particular case of a hexagonal bundle, this ratio has a non-zero upper limit that is reached when the rods come into contact with each other ($P/D=1$), being 2.7 and 1.6 for the central and the edge subchannel, respectively. Obviously, this case falls

out of the scope of this thesis as the contact between the rods would damage the fuel elements of a nuclear reactor. The lower limit of the D_h^*/D_h ratio, however, differs per subchannel. Figure 4.12b shows that the D_h^*/D_h ratio goes to zero if the central subchannel is considered, whereas it goes to the value $1/\pi$ for the edge (wall-bounded) subchannel.
The experiment performed with an eccentric rod inside a circular channel by Choueiri and Tavoularis [13] are included in the plot ($\bigtriangledown$ in Figure 4.12a) as well. However, this case deserves special care due to geometry very different from the bundle since the borders of the gap region are not clearly identifiable.
It is to be noted that the correlation might have a different expression for low values of the Reynolds number. Experimental results discussed in Chapter 2 of this thesis and reported in [17] show that the length of coherent structures increases at low values of the gap Reynolds number, which cannot be neglected from the correlation. Recalling the general form expressed in Equation 4.14, the exponent of the term Re_{gap}^{ζ} could, thus, become lower than zero for low values of the Reynolds.

4.5.3 Interaction between the rod and the flow

This section discusses the results of the fluid-structure interaction measurements performed with the high speed camera. Three frequencies are considered for this analysis: the frequency of oscillation of the silicone rod, its natural frequency, and the frequency at which coherent structures move in the axial direction. The average frequency of vibration of the silicone rod's wall, f_{sil}, the average displacement $\bar{\varepsilon}$, and the ε_{rms} are obtained through ten series of measurements repeated on different days for each value of the flow rate. The natural frequency of the silicone rod is estimated depending on the local velocity around the central flexible rod applying the theory explained in section 4.2.2. The stream-wise rate of passage of the coherent structures is measured with LDA in the central subchannel close to the rod (Figure 4.10b). The three frequency series, rendered non dimensional, are plotted in Figure 4.13 against the non dimensional velocity. The frequency of the coherent structures, f_y^* increases linearly with the flow speed as previously discussed. The natural frequency of the silicone rod, $f_{sil,n}^*$, decreases with the velocity of the surrounding fluid: as the flow rate increases, the damping effect of the term $\frac{1}{2}C_N\frac{m_a v}{D_{sil,o}}$ in Equation 4.2 grows under the action of the flow confinement [26], especially with highly confined flows at low P/D ratios. The vibration frequency of the rod, f_{sil}^*, increases with velocity reaching the highest value of f_{sil}^*=1.6 (f_{sil}=4.2 Hz) for v^*=7 ($Re_e \approx 8500$). If the flow rate is increased further, the frequency of the silicone rod decreases and becomes nearly constant for $v^* \geq 9.4$ ($Re_e \geq 29\,000$), as shown in more detail in Figure 4.14a. The frequency of the structures f_y^* approaches twice the natural frequency of the rod $2f_{sil,n}^*$ when the measured frequency of oscillation of the rod wall f_{sil}^* matches $f_{sil,n}^*$ for v^*=5.7 ($Re_e \approx 22\,700$).
Both trends of the mean displacement of the wall, $\bar{\varepsilon}$, and its root mean square, ε_{rms}, (Figure 4.15) display a clear peak in the Reynolds number range where $f_y^*=2f_{sil,n}^*$. The results shown in Figure 4.13 can therefore have the following interpretation. Choueiri and Tavoularis [13] measured that the lateral velocity component of the vortex street oscillated with half the rate of passage of the coherent structures

in the axial direction $f_y/2$. This was consistent with Meyer and Rehme's model (sketched in Figure 4.14b) that regarded coherent structures near a gap as counter-rotating vortices which induce a fluctuating velocity field. The components of such a field along the span-wise and stream-wise directions x and y gives a velocity that fluctuates twice as fast along y (V_y in Figure 4.14b). Conversely, the span-wise component (U_x in Figure 4.14b) would oscillate twice as slow around the mean value. The fluctuating lateral velocity component would produce an external force on the rod, oscillating in time with frequency $f_y/2$. When such force oscillates with $f_y/2=f_{sil,n}$ (Figure 4.13), the rod and the vortex street synchronise and the magnitude of the oscillations increases [98], as shown in Figure 4.15.

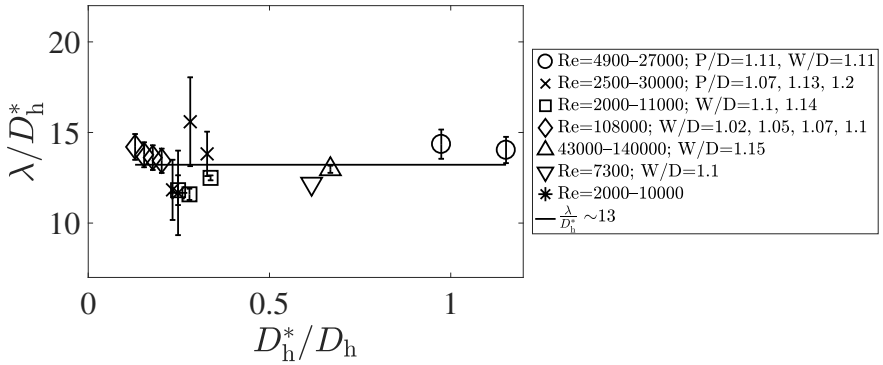

(a)

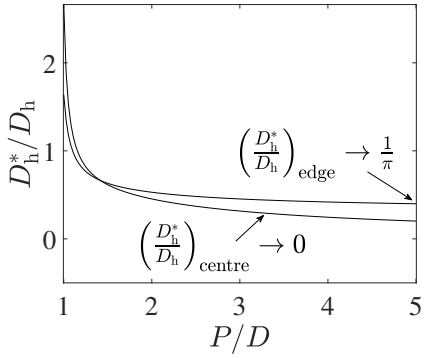

(b)

Figure 4.12: a) Normalised wavelength of coherent structures $\lambda/D_{\mathrm{h}}^{*}$ against $D_{\mathrm{h}}^{*}/D_{\mathrm{h}}$. The Reynolds numbers in the legend are based on the total flow area of the test section. ◯: this work's experiments; ×: data from [76]; □: data from [17]; ◇: data from [19]; △: data from [87]; ▽: data from [13]; ∗ data from [61]. b) Trend of $D_{\mathrm{h}}^{*}/D_{\mathrm{h}}$ as a function of P/D for edge and central subchannels of a hexagonal bundle; as the bundle becomes indefinitely large the ratio tends to zero (centre subchannel) and to a finite number (edge subchannel).

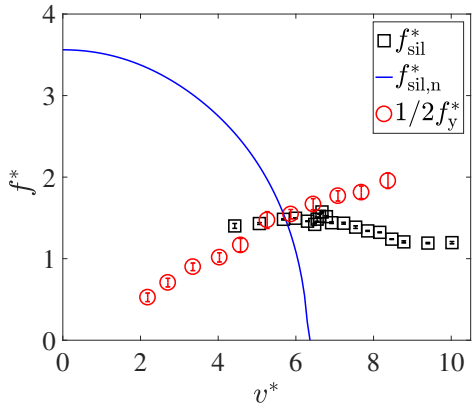

Figure 4.13: Plot of $f^*_y/2$ (◯), estimated natural frequency of the central silicone rod $f_{sil,n}$ (blue line), and frequecy of vibration of the silicone rod wall f^*_{sil} (□) measured with the high-speed camera system.

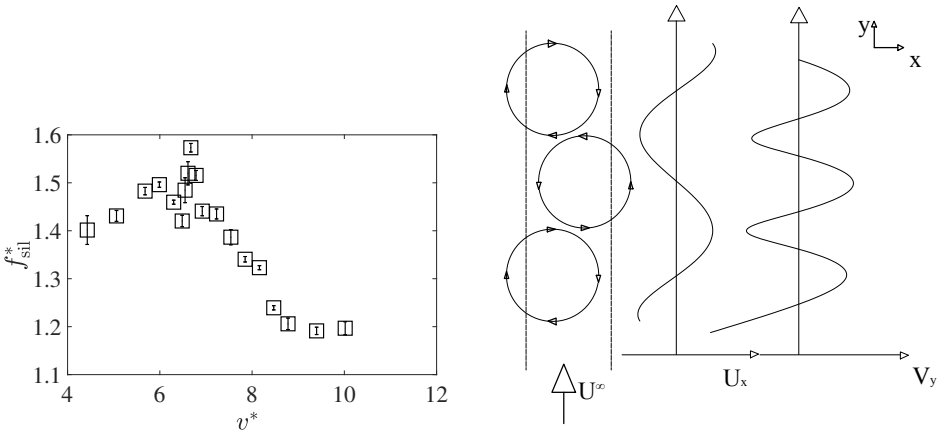

(a) **(b)**

Figure 4.14: a) Non dimensional response frequency of the silicone rod, depending on the non dimensional velocity v^*. b) Gap vortex streets moving with the axial flow along a gap, identified by the dashed borders; originally proposed by Meyer and Rehme in [18].

4.6 Practical application of this chapter's findings

The findings of this chapter are applied to a couple of real cases, being the Super Phenix and the MYRRHA (Multi-purpose hYbrid Research Reactor for High-tech Applications) reactors, cooled with liquid sodium and lead-bismuth eutectic (LBE) respectively. Both designs have the fuel rods arranged in a hexagonal lattice.

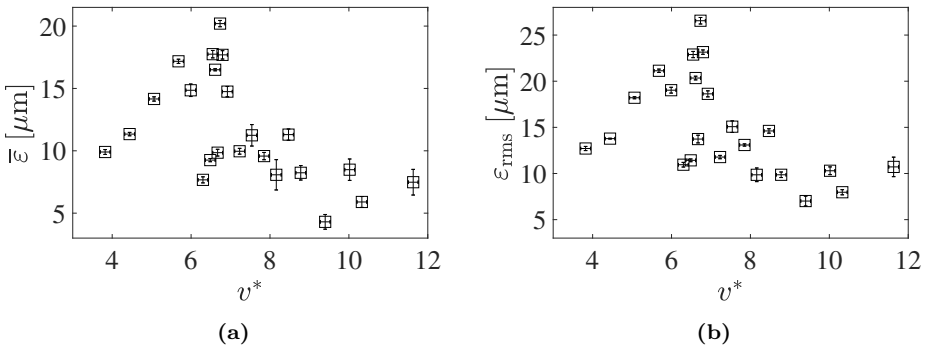

Figure 4.15: Average displacements of the silicone rod border (a) and displacement root mean square (b) depending on the Reynolds number. A clear peak in both plots, once compared with the measured response frequency, indicates synchronisation between the rod and the flow structures.

The Super Phenix has a P/D ratio of 1.12, pin diameter of 8.65×10^{-3} mm and active core length of 2 m [99, 89]. The average sodium temperature through the core is 470 °C and the mean flow speed $5\,\mathrm{m\,s^{-1}}$. Using the correlation derived in this chapter, one can estimate that the expected coherent structures inside one of the main triangular subchannels of the core of the Super Phenix have a wavelength of 4.9 cm. This corresponds to a stream-wise frequency f_y of 100 Hz. Based on the findings discussed in this chapter, a lateral frequency $\frac{f_y}{2}$ of 50 Hz is expected. The theory discussed in section 4.2 to estimate the natural frequency of a rod surrounded by other six arranged in a hexagonal lattice yields a frequency of 5.4 Hz, which is well below that of the coherent structures, seemingly not posing issues of fatigue phenomena on the fuel elements.
The second practical application is to the MYRRHA reactor, which has a P/D ratio of 1.28, pin diameter of 6.55×10^{-3} mm, wall thickness of 0.51 mm, core length of 1.4 m, and the average LBE temperature through the core 340 °C [100]. The estimated coherent structures wavelength is 5.4 cm that, moving with the average flow speed of $1.7\,\mathrm{m\,s^{-1}}$, corresponds to a stream-wise frequency of 31 Hz, hence the expected lateral frequency $\frac{f_y}{2}$=15.5 Hz. The natural frequency of the fuel rod at the considered flow velocity is 5.4 Hz.
Based on these estimations, the frequency of the coherent structures occurring in MYRRHA is closer to the natural frequency of the fuel rod than in the Super Phenix, making that design more prone to synchronization with flow structures.

However, both Super Phenix and MYRRHA employ helicoid wires wrapped around the rods to avoid contact and to prevent damage of the fuel pins, which are not taken into account in these examples.

4.7 Summary

The work described in this chapter aimed at studying the structural response of the central rod to large coherent structures occurring in the flow through a hexagonal bundle of rod tightly clustered (P/D=1.11). The flow was studied with Laser Doppler Anemometry while the vibrations induced on the flexible rod were recorded with a high-speed camera. Optical access to the measurement region was achieved by means of the refractive index-matching technique.

The measurements of frequency and displacements of the rod wall suggested synchronization between the rod and the coherent structures when these move axially with twice the natural frequency of the rod. This condition is characterised by the increased magnitude of the oscillations and by a response near to the natural frequency of the rod.

A new correlation for estimating the wavelength of the structures is derived based on dimensional analysis and experiments, resulting in a wavelength that scales linearly with the hydraulic diameter of the gap region. Such a correlation is valid for different geometries, involving channels with single rods or more complex rod bundles with P/D (or W/D) ranging from 1.02 to 1.20.

The findings presented in this chapter contribute to explain further the physics of the flow-induced vibrations of coherent structures arising in axial rod bundle flows, typical of industrial applications. Furthermore, the proposed correlation may be helpful in designing industrial components that are not prone to resonance phenomena and, thus, mechanical fatigue.

4.8 Nomenclature

Symbols	Description	Units
a_1,a_2, a_3, a_4, a_5, a_6	Exponents of the dimensional analysis	–
$C'_{\mathrm{fT,c}}$, $C'_{\mathrm{fT,e}}$	Coefficients for the pressure drop across the hexagonal section	–
C_{m}	Added mass coefficient	–
C_{N}	Lateral drag force coefficient	–
C_{T}	Longitudinal force coefficient	–
C_{V}	Viscous force coefficient	–
C_1, C_2	Coefficients	–
D_{h}	Hydraulic diameter of the subchannel	m
$D_{\mathrm{h,c}}$, $D_{\mathrm{h,e}}$	Hydraulic diameter of central and edge subchannels, respectively	m
D^*_{h}	Hydraulic diameter of the gap region	m
D_{o}	Equivalent diameter of the outer channel	m
D	Rod diameter	m
$D_{\mathrm{sil,i}}$, $D_{\mathrm{sil,o}}$	Inner and outer diameter of the silicone rod	m
$\mathrm{f_c}$, $\mathrm{f_e}$	Friction coefficients of central and edge subchannels, respectively	–
$\mathrm{f_{gap}}$, $\mathrm{f_{ch}}$	Friction coefficients of the gap region and main subchannel, respectively	–
E	Young (or elasticity) modulus	Pa
$(f^*_{\mathrm{sil,n}})$, $f_{\mathrm{sil,n}}$	(Non dimensional) natural frequency of the silicone rod, respectively	Hz
(f^*_{sil}), f_{sil}	(Non dimensional) vibration frequency of the silicone rod, respectively	Hz
(f^*_{y}), f_{y}	(Non dimensional) frequency of coherent structures, respectively	Hz
I	Moment of inertia of the silicone rod	$\mathrm{m^2}$
$\mathrm{L_{sil}}$	Silicone rod length	m
$\mathrm{m_a}$	Added mass on the silicone rod	kg
$\mathrm{m_{sil}}$	Silicone rod mass	kg
N	Number of recorded frames of the high speed camera	–
$\mathrm{N_g}$	Number of points for fitting the spectral peak	–
P	Pin pitch	m
P/D	Ratio between the pitch and the diameter of the half rods	–
$[\Delta p]_{\mathrm{ch}}$, $[\Delta p]_{\mathrm{gap}}$	Pressure drop across the main subchannel and the gap region, respectively	Pa
$[\Delta p]_{\mathrm{c}}$, $[\Delta p]_{\mathrm{e}}$	Pressure drop across central and edge subchannels, respectively	Pa
Q	Volumetric flow rate	$\mathrm{m^3\,s^{-1}}$
x, y, z	Span-wise (transversal), stream-wise (vertical), and normal directions	m

S, S_{fit}	Spectrum and fitted value, respectively	
$\bar{S}$	Mean value of the spectrum	
W/D	Nearest wall distance-to-rod diameter ratio	–

Symbols	**Description**	**Units**
v^*, v	(Non dimensional) stream-wise (vertical) velocity component, respectively	$\mathrm{m\,s^{-1}}$
v_{c}, v_{e}	(Non dimensional) stream-wise (vertical) velocity component inside the central and edge subchannels, respectively	$\mathrm{m\,s^{-1}}$
v_{gap}	Stream-wise (vertical) velocity component inside the gap region	$\mathrm{m\,s^{-1}}$
v_{in}	Value at the inflection point in the profile of the stream-wise (vertical) velocity component	$\mathrm{m\,s^{-1}}$
v'_{rms}	Root mean square of the stream-wise (vertical) velocity component	$\mathrm{m\,s^{-1}}$
t	Time	s

Greek letters	**Description**	**Units**
δ	Gap width	m
ε_{d}	Dissipation rate based on Kolmogorov theory	$\mathrm{m^2\,s^{-3}}$
$\varepsilon(t_i)$, $\bar{\varepsilon}$	Instantaneous and mean displacement of the silicone rod	µm
ε_{rms}	Root mean square of the displacement of the silicone rod	m
ζ	Exponent	–
λ	Average stream-wise (vertical) wavelength of coherent structures	m
λ_{Max}, λ_{min}	Maximum and minimum estimated stream-wise wavelength of coherent structures	m
μ	Dynamic viscosity of water	Pa s
ν	Kinematic viscosity	$\mathrm{m^2\,s^{-1}}$
ξ	Exponent	–
ρ	Fluid density	$\mathrm{kg\,m^{-3}}$
ρ_{ac}	Autocorrelation coefficient	–
σ_{y}	Width of the Gaussian bell fitting the frequency spectra	Hz
χ_1, χ_2	Exponents	–
$\vec{\omega}$	Vorticity vector	$\mathrm{s^{-1}}$

Acronyms	**Description**
CMOS	Complementary Metal-Oxide Semiconductor
DFT	Discrete Fourier Transform
FEP	Fluorinated Ethylene Propylene
FIV	Flow-induced vibration
FSI	Fluid-structure interaction
Gen-IV	Generation IV
LBE	Lead-bismuth eutectic
LDA	Laser Doppler Anemometry
LMFBR	Liquid Metal Fast Breeder Reactor
LWR	Light Water Reactor
MYRRHA	Multi-purpose hYbrid Research Reactor for High-tech Applications
NRMSE	Normalised Root Mean Square Error
RIM	Refractive Index Matching
SEEDS-1	SEven rods Experiments in Delft for Sesame-1
TRIGA	Training Research Isotopes General Atomic

Non dimensional groups	**Description**
Re	Reynolds number
Re_{c}, Re_{e}	Reynolds number of central and edge subchannels
Re_{gap}	Reynolds number of the gap region

Chapter 5

Measuring and modelling migratory flow due to wire spacers in rod bundles

5.1 Introduction and motivation

Rod bundles characterise the geometry of many industrial components, such as heat exchangers and the core of light water and liquid metal cooled nuclear reactors. In particular, the core of a Liquid Metal Fast Breeder Reactor (LMFBR) consists of a hexagonal bundle of rods, each wrapped by a wire wound helicoidally. These wires prevent damage by fretting of the fuel rod's cladding, and guide the liquid metal through the gaps between the pins enhancing radial heat transfer and improving the safe operation of the reactor.
Depending on the position of the wire, the flow was found to unexpectedly bend against the direction of the wire. This was called "migratory flow" by Ohtake *et al.* and ascribed to the increased hydraulic resistance caused by the wire inside the considered subchannel [44]. A physical model that could predict such a flow bending, however, was not provided, nor it is available nowadays.
This chapter describes the work carried out to measure migratory flow in a 7-rod, wire-wrapped hexagonal bundle to develop a model that explains and quantifies the bending of the flow due to the action of the wire. The facility, SEEDS-2, replaces SEEDS-1 in the experimental loop. Planar Particle Image Velocimetry (PIV) is performed to measure the flow near the wire wrapped around the central rod of the bundle. The optical access needed for the measurements is provided by making the outer casing of transparent Perspex, and by replacing part of the steel of the rods with Fluorinated Ethylene Propylene (FEP), which is a refractive index-matching material.

The content of this chapter has been submitted *Int. J. Heat Fluid Fl.* **80** (2019). DOI:10.1016/j.ijheatfluidflow.2019.108491

The approach is structured as follows:

1. The flow field at the front of the central wrapping wire is studied with PIV for six equally spaced Reynolds numbers, at room temperature, and with water as working fluid.

2. The pressure gradient field close to the wire is retrieved from the measured velocity field and the discretised, two-dimensional Navier-Stokes equations.

3. A model, derived from the Euler equations, is derived for estimating both the pressure gradient normal to the wire and the bending angle of the flow streamlines.

4. The pressure gradient field obtained from the model is compared with the experimentally obtained field.

5. Finally, the theoretically predicted bending angle of the flow is compared with the experimental values to confirm the validity of the proposed model.

5.2 Experimental apparatus

The measurement system is a planar PIV system consisting of a laser source and a high speed camera. The light source illuminates a region of fluid close to the wire wrapped around the central rod of the hexagonal bundle. The images needed for computing the flow velocity are recorded by the camera from the front side of the Perspex hexagonal casing.

5.2.1 PIV and uncertainty quantification

The light source of the PIV system is a class-IV, diode pumped 5 W laser with a wavelength of 532 nm (LaVision, Germany). The DaVis software allows for adjusting the separation time between the two laser pulses. The combination of a spherical and a cylindrical lens creates the laser sheet, which has a beam waist (the thinnest region of the sheet) thickness of 1 mm. The flow is seeded with borosilicate glass hollow spheres (LaVision, Germany) with an average density of $1.1\,\mathrm{g\,cm^{-3}}$ and average diameter of $9-13\,\mu\mathrm{m}$. The camera used for PIV measurements is a Complementary Metal-Oxide Semiconductor (CMOS) Imager MX-4M (LaVision, Germany) with 4 MP of resolution (pixel size of $5.5\,\mu\mathrm{m}$). The camera mounts an AF-S 50 mm F/1.4 (Nikon) lens with a magnification factor M_0=0.13. The depth of the laser sheet (out-of-plane direction) δz is given by [101] as

$$\delta z = 4\left(1+\frac{1}{M_0}\right)^2 \mathrm{f}_{\#}^2 \lambda_\mathrm{l} = 0.6\,\mathrm{mm}, \tag{5.1}$$

where $\mathrm{f}_{\#}$ is the lens aperture, and λ_l is the laser wavelength.
Pairs of images are recorded by the camera with a frequency 18 Hz where the particles appear as bright spots as they reflect light. The time separation between the images, in each pair, is adjusted by the laser: this can be as low as 100 µs.

Cross-correlating each pair of images allows for detecting the displcement of each particle during the time interval between the two images. Based on a calibration factor, the pixel displacement is finally converted into a velocity value. An intensity correction algorithm consisting of a background subtraction is used to diminish the reflection from the internal components of the bundle. The recorded images are pre-processed by subtracting the local intensity of each image (sliding background) to keep intensity fluctuations at a minimum. This method averages the local intensity of light around each particle. The mean value is then subtracted from the intensity value of each pixel to improve the local contrast. The velocity vectors are calculated with a multi-pass option where the initial size of the interrogation window is 64×64 pixels and two passes are used: the displacement of the particles obtained in the first pass is used as information to shift the interrogation window in the next pass. The initial size of the interrogation window is subsequently decreased to 48×48 pixels. A reference vector field computed on 500 images is used in the first pass to introduce an initial deformation of the interrogation window. This enhances the signal-to-noise ratio of the correlation peaks. The post-processing consists of a median filter to remove outliers [102, 35]. The resulting blank points are filled with a vector interpolation algorithm.

The uncertainty on the the PIV measurements consists of a statistical error and a systematic error. The statistical error σ_{stat} is evaluated following [101] as

$$\sigma_{\mathrm{stat}} = \frac{\sigma}{\sqrt{\mathrm{N}}} = \sqrt{\frac{1}{\mathrm{N}\,(\mathrm{N}-1)} \sum_{i=1}^{\mathrm{N}} (v_i - \bar{v})^2}, \tag{5.2}$$

where σ is the standard deviation of the measured velocity samples, N is the number of samples, and $\bar{v}$ is the mean value.
The systematic error σ_{syst} is due to the calibration of the PIV system: the conversion factor F from pixel to mm is based on the image of the wire, whose diameter in mm is known:

$$\mathrm{F} = D_{\mathrm{w}} / D_{\mathrm{w,p}}, \tag{5.3}$$

being D_{w} and $D_{\mathrm{w,p}}$ the diameter of the wire in mm and pixel, respectively.
Since there is a dimensional tolerance δD_{w} on the wire diameter (reported in table 3.2), F is subject to an uncertainty as well. This is estimated considering that a generic velocity vector is evaluated from the measurements as

$$v_i = \frac{\Delta_{\mathrm{p}} \mathrm{F}}{dt} = \frac{\Delta_{\mathrm{p}}}{dt} \frac{D_{\mathrm{w}}}{D_{\mathrm{w,p}}}, \tag{5.4}$$

where Δ_{p} is the particle displacement in pixel between two images and dt is the time between the frames. An uncertainty on the diameter of the wire expressed in pixel $\delta D_{\mathrm{w,p}} = 1$ is also taken into account in the systematic error.
The systematic error σ_{syst} is evaluated through the uncertainty propagation formula as

$$\sigma_{\mathrm{syst}} = \sqrt{\left(\frac{\partial v_i}{\partial D_{\mathrm{w}}} \delta D_{\mathrm{w}} \right)^2 + \left(\frac{\partial v_i}{\partial D_{\mathrm{w,p}}} \delta D_{\mathrm{w,p}} \right)^2}, \tag{5.5}$$

where the two derivative terms are obtained by deriving Equation 5.4 with respect to D_w and $D_{w,p}$:

$$\frac{\partial v_i}{\partial D_w} = \frac{\Delta_p}{dt\ D_{w,p}}; \qquad \frac{\partial v_i}{\partial D_{w,p}} = -\frac{\Delta_p\ D_w}{dt\ D_{w,p}^2}. \tag{5.6}$$

The total uncertainty $\sigma_{\bar{v}}$ is estimated adding in quadrature σ_{stat} and σ_{syst}:

$$\sigma_{\bar{v}} = \sqrt{\sigma_{stat}^2 + \sigma_{syst}^2}. \tag{5.7}$$

The uncertainty thus calculated is included in the line plots of the PIV measurements shown from here on.

5.3 Measurement campaign

The measurement campaign consists of six flow rate values for which the corresponding Reynolds numbers are calculated based on the bundle's hydraulic diameter $D_h = 4A/P_w$, where A is the bundle flow area, and P_w is the corresponding wetted perimeter, according to [89]. Table 5.1 reports the water temperature of the experiments and the Reynolds number for the investigated flow rates. Each

Table 5.1: Q: mass flow rate; T: temperature of the water; Re: Reynolds number.

Q [$m^3\,s^{-1}$]	T [°C]	Re
2.95×10^{-3}	32.3	16330
2.70×10^{-3}	31.7	14760
2.30×10^{-3}	32.0	12650
1.80×10^{-3}	32.2	9940
1.370×10^{-3}	32.3	7580
9.00×10^{-4}	32.4	4990

PIV measurements consist of 10000 images collected at a rate of 18 frames per second. The location of the measurement region is shown in Figure 5.1. The laser sheet enters the outer hexagonal Perspex casing (Figure 5.1a) and it goes through the FEP, reaching the central wire spacer where the measurement region is located (red rectangular area in Figure 5.1b). For a preliminary measurement, the laser sheet is moved closer to the rod (Figure 5.1b, dashed profile in section B-B) in order to study the flow area downstream the wire. The second, and main, measurement campaign is conducted with the laser sheet closer to the bulk region of the subchannel, being tangent to the central rod's wire spacer. The flow area in front of the helicoid spacer is thus investigated.

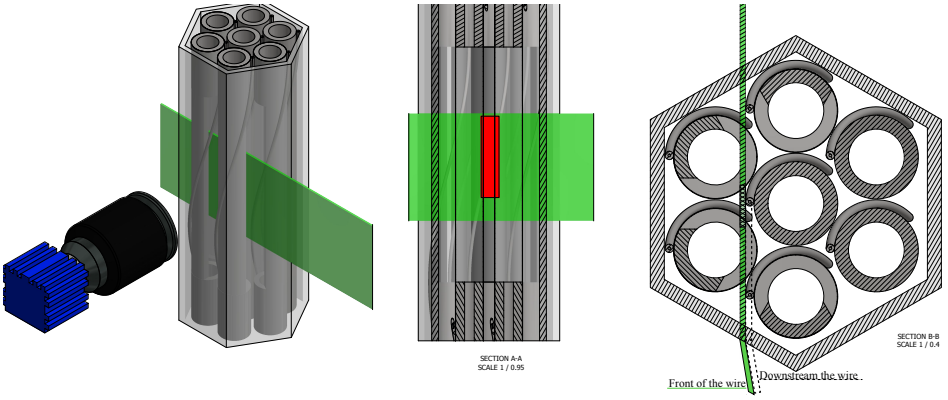

Figure 5.1: a) Overview of the rod bundle test section as the laser light of the PIV system goes through: the area of interest (AOI) is the red rectangular area of the laser sheet. b) Front section (section A-A) and top view (section B-B) of the bundle where the light sheet goes through the FEP in front of the central rod's wire. Section B-B shows the positions of the laser sheet corresponding to the preliminary measurement (dashed line), and to the measurement campaign focusing on the flow area in front of the wire.

5.4 Symmetry of the flow

Due to the closeness of the elements of the bundle, the correct placement of the rods is very important to avoid flow blockages and asymmetric flow during the experiments. Owing to the small size of the bundle, an error in the orientation of the rods would affect the whole flow field. For this reason, a preliminary series of masurements is carried out at Re=23450 focusing on the flow around the central rod.

Given the symmetry of the setup, the flow fields at different locations along the central wire should be similar. Therefore, two PIV measurements are performed that study the flow near the centre. One PIV measurement is carried out through the front of the hexagonal Perspex casing, measuring the flow area shown in Figure 5.1; the main measurement campaign will be carried out at this location.

Later, the bundle is turned by 60° clock-wise allowing for a second, additional measurement through the side (Figure 5.2): the measured area is shifted upward in order to have the wire in the same position of the first measurement, relative to the gap. A similar measurement could not be performed through the left side as the measured area could not be reached by the moving system.

The two time-averaged flow fields thus obtained are shown in Figure 5.3. The flow fields are qualitatively similar, indicating that the rods are correctly oriented inside the hexagonal case.

A quantitative comparison between the two measurements is done by evaluating

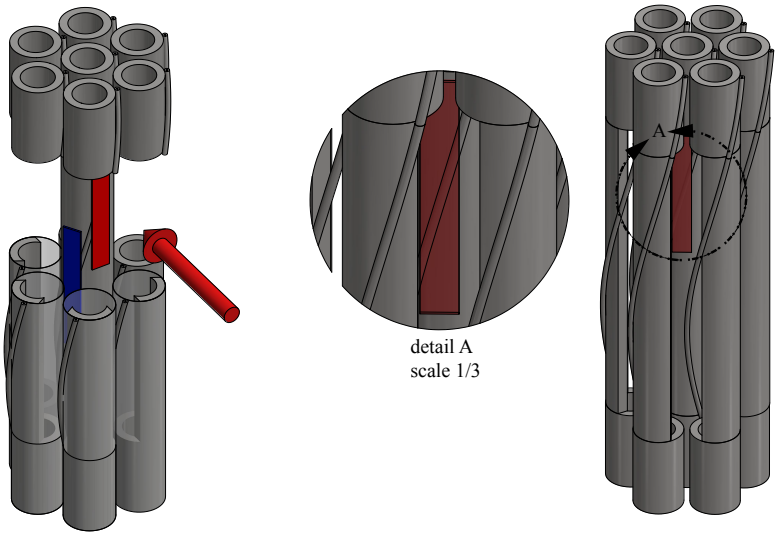

(a) **(b)**

Figure 5.2: a) Flow areas through the front (blue) and through the side (red) studied to check the flow symmetry; the red arrow indicates the second side through which the additional measurement is performed. b) The wire in the additional measurement region is in the same position, relative to the gap, of the measurement through the front (detail A).

the velocity magnitude along three arbitrary vertical lines of the flow fields. The velocity magnitude is shown in Figure 5.4, where each plot refers to one of the three lines. The plots show that the magnitude of the velocity measured through the two faces is similar within 6.4% (x=4 mm), 3.5% (x=6 mm), and 4.1% (x=8 mm), suggesting that the flow inside the subchannels is not obstructed and that the rods are installed correctly inside the bundle.

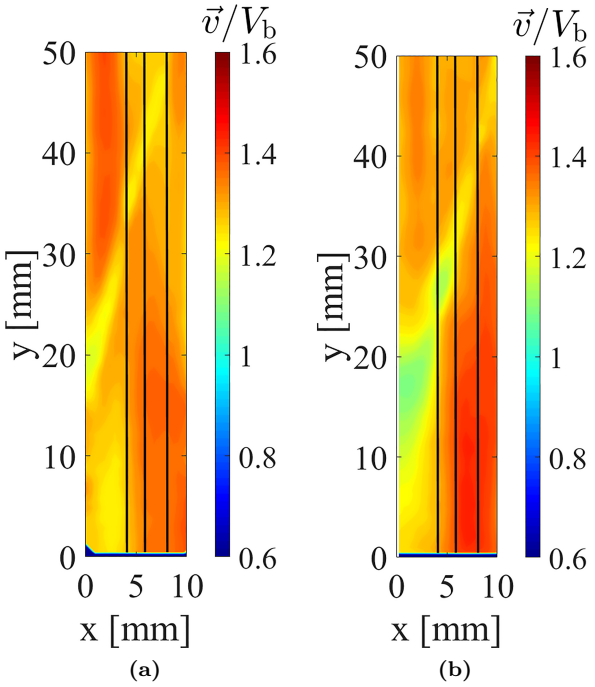

Figure 5.3: Flow field measured through the front side (a) and through the side to the right (b). The vertical lines highlight the paths followed for comparing the two flow fields.

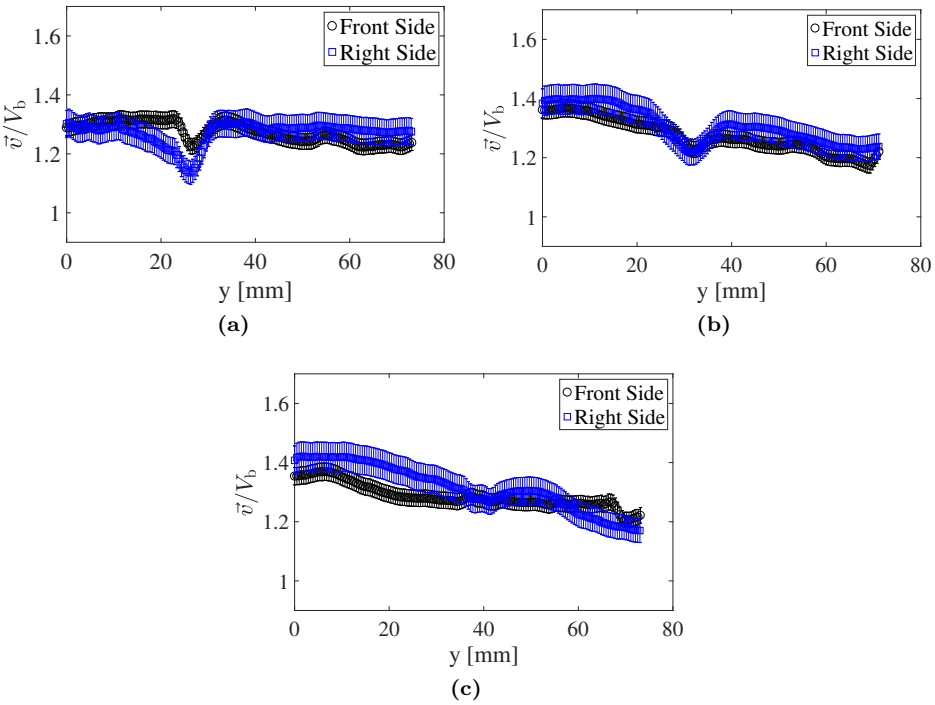

Figure 5.4: Normalised velocity magnitude evaluated along the vertical line (a) x=4 mm, (b) x=6 mm and (c) x=8 mm for the two measurements.

5.5 Time-averaged velocity fields

The initial measurement campaign studies the fluid region downstream the wire (Figure 5.1b, view B-B), showing that the flow follows the helical path of the wire, as expected, contributing to the mixing. This is evident from Figure 5.5a where the blue colour indicates a negative direction of the u component (towards the left). The flow field of the lateral component measured downstream the wire for the six Reynolds numbers is shown in Figure 5.6 where the superimposed vectors follow the wire direction (from top right to bottom left in the plots).

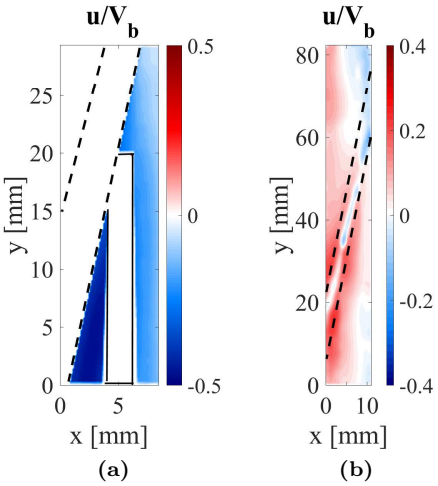

Figure 5.5: a) Contour plot of the lateral velocity component u measured beneath the wire; the dashed line indicates the wire's position, whereas the solid line bounds the area affected by reflection, which is masked out. b) Contour plot of the u component measured at the front of the wire, closer to the bulk of the subchannel; the dashed line marks the borders of the wire.

Figure 5.5b shows that if the measurement region is moved to the front of the wire, closer to the bulk of the subchannel, the fluid changes direction moving against the wire's path. This is clear from the red colour that shows a positive u, hence a flow in the positive x direction. This flow behaviour, called "migratory flow" by Ohtake *et al.* [44], was ascribed to the increased hydraulic resistance that the wire causes in the subchannel. A similar behaviour is found in Song *et al.* [45].

The velocity fields shown hereafter focus on the flow in front of the central wire where the migratory flow is observed. The measured quantities are the stream-wise and span-wise velocity components v and u, respectively.
Figure 5.7 shows the contour plot of the time-averaged axial velocity component v, for the considered values of Reynolds numbers (see table 5.1). A low-speed region appears at the downstream side of the wire, which is also found by [33].

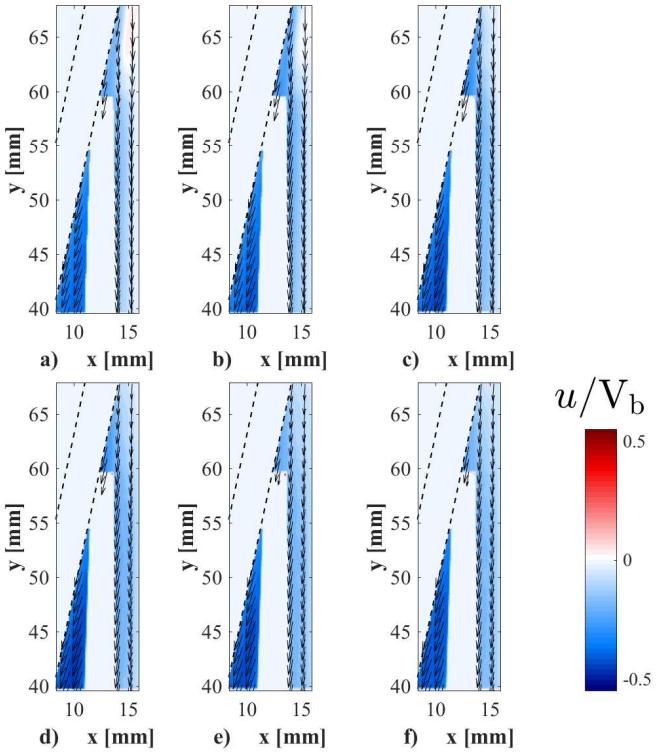

Figure 5.6: Span-wise time-averaged velocity component u normalised to the bulk velocity V_b, measured downstream the wire, shown as a dashed line. a) Re=4990; b) Re=7580; c) Re=9940; d) Re=12650; e) Re=14760; f) Re=16330.

This region is more spread-out at the lower Reynolds numbers and it becomes narrower as the Reynolds increases. This is quantitatively more clear in Figure 5.8a where v is evaluated along the vertical line x=5.6 mm for Re=4990, Re=12650 and Re=16330 (the flow direction in the line plot is from left to right). At Re=4990 the low-speed region downstream of the wire is more pronounced and it affects a larger area of the wake.

Figure 5.9 shows the contour plot of the normalised time-averaged span-wise velocity component u for the six studied Reynolds numbers. The positive sign of the lateral velocity component means that the flow coming from the top bends towards the right as it approaches the wire. The figure shows that the relative magnitude of u is slightly higher at lower Reynolds numbers, meaning that the flow tends to bend more markedly at lower flow rates. The lateral component u is evaluated along the same vertical line and the values are plotted in Figure 5.8b. The lateral component becomes increasingly higher as the wire is approached; the bending towards the wire is relatively stronger as the Reynolds number is decreased, reaching a maximum for Re=4990.

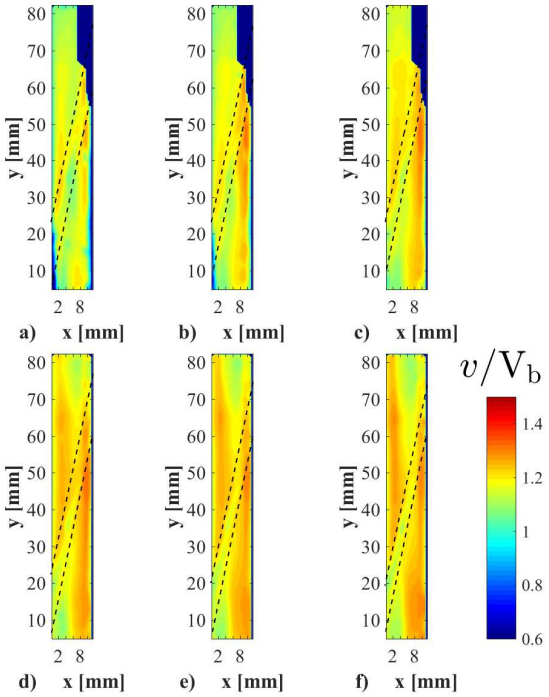

Figure 5.7: Stream-wise time-averaged velocity component v normalised to the bulk velocity V_b. a) Re=4990; b) Re=7580; c) Re=9940; d) Re=12650; e) Re=14760; f) Re=16330. The main flow is from top to bottom. The cases a, b, and c have the upper-right corner masked-out due to reflections.

5.5.1 Determining the pressure gradient field from the 2D Navier-Stokes equations

The pressure gradient normal to the wire, later on needed to describe the migratory flow, is evaluated by means of the Navier-Stokes equations applied to the measured velocity fields. Due to the action of the wire that pulls the fluid transversally throughout the gaps, the fluid measured close to the rod is assumed to have two major velocity components: the lateral flow direction induced by the wire, and the main axial direction. Based on the experiments described in [103], the out-of-plane velocity component is estimated to be equal at most to $10\%V_b$ for a Reynolds number of 6300. Moreover, a recent numerical work [45] showed that the local flow behaviour near the wire is independent of the Reynolds number. It is thus reasonable to assume that the relative magnitude of the out-of-plane velocity component near the wire does not strongly depend on the flow rate. Hence, the flow is considered two-dimensional. The Navier-Stokes equations are discretised in space and time following the approach of [104, 105]. The pressure gradient is

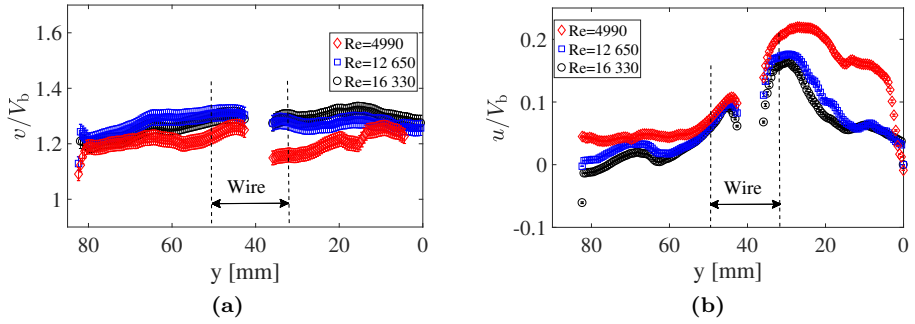

Figure 5.8: a) Stream-wise (axial) and b) span-wise (lateral) velocity components evaluated along the vertical line x=5.6 mm in the plane at the front of the wire for three Reynolds numbers. The flow direction is from left to right. Due to light reflection from the wire, some values measured at the wire's position are not included.

expressed as follows:

$$\nabla p = -\rho \left[\frac{\partial \vec{v}}{\partial t} + (\vec{v} \cdot \nabla)\vec{v} - \nu \nabla^2 \vec{v} \right], \tag{5.8}$$

where ν is the kinematic viscosity. Assuming a two-dimensional flow, Equation 5.8 is decomposed along x (and similarly along y) as

$$\frac{\partial p(x,y,t)}{\partial x} = -\rho \left[\frac{\partial u(x,y,t)}{\partial t} + u(x,y,t)\frac{\partial u(x,y,t)}{\partial x} + v(x,y,t)\frac{\partial u(x,y,t)}{\partial y} - \nu \left(\frac{\partial^2 u}{\partial x^2} + \frac{\partial^2 u}{\partial y^2} \right) \right]. \tag{5.9}$$

The time derivative term is discretized with a central finite difference scheme following [105], and considering a separation time between two consecutive images of 0.055 s. The same discretization scheme is used for the spatial derivatives of u and v. This leads, for the x direction (and similarly for the y direction), to

$$\begin{aligned} \frac{\partial p(i,j,\tau)}{\partial x} = -\rho \Bigg[& \frac{u(i,j,\tau+1) - u(i,j,\tau-1)}{2\Delta t} + u(i,j,\tau)\frac{u(i+1,j,\tau) - u(i-1,j,\tau)}{2\Delta x} \\ & + v(i,j,\tau)\frac{u(i,j+1,\tau) - u(i,j-1,\tau)}{2\Delta y} \\ & - \nu \Bigg(\frac{u(i+1,j,\tau) - 2u(i,j,\tau) + u(i-1,j,\tau)}{(\Delta x)^2} \\ & + \frac{u(i,j+1,\tau) - 2u(i,j,\tau) + u(i,j-1,\tau)}{(\Delta y)^2} \Bigg) \Bigg], \end{aligned} \tag{5.10}$$

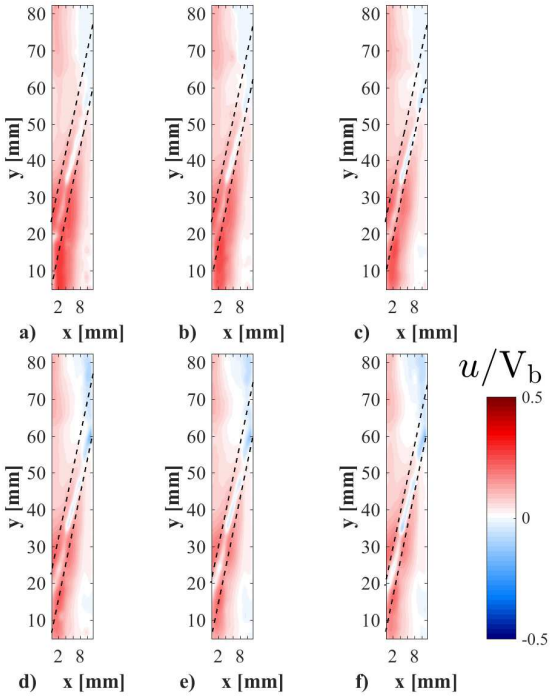

Figure 5.9: Span-wise velocity component u normalised to the bulk velocity V_b, overlapped to the vectorial field. a) Re=4990; b) Re=7580; c) Re=9940; d) Re=12650; e) Re=14760; f) Re=16330. The main flow is from top to bottom.

where Δx and Δy are the spatial pitches between consecutive vectors of the matrix along x and y, respectively. Equation 5.10, and the corresponding one for the y direction, are averaged over the total recorded images to obtain the time-averaged pressure gradient components along x and y:

$$\overline{\frac{\partial p(i,j)}{\partial x}} = \frac{1}{\mathrm{N}} \sum_{\tau=1}^{\mathrm{N}} \frac{\partial p(i,j,\tau)}{\partial x}, \tag{5.11}$$

and

$$\overline{\frac{\partial p(i,j)}{\partial y}} = \frac{1}{N} \sum_{\tau=1}^{N} \frac{\partial p(i,j,\tau)}{\partial y}, \tag{5.12}$$

where N is the number of recorded PIV images. Finally, the time-averaged pressure gradient normal to the wire is estimated as

$$\frac{\partial p(i,j)}{\partial \tilde{x}} = \overline{\frac{\partial p(i,j)}{\partial x}} \sin\theta + \overline{\frac{\partial p(i,j)}{\partial y}} \cos\theta, \tag{5.13}$$

where θ=77° is the angle that the wire forms with the horizontal (later sketched in Figure 5.11a).

5.6 Modelling of migratory flow

The time-averaged velocity fields shown in the previous section show that the flow near the wire bends against the wrapping direction of the helicoid spacer (Figure 5.6), if the flow is measured at the front of the wire. This section discusses the theory through which this behaviour is modelled and explained.

5.6.1 Euler equations in the streamline's coordinate system

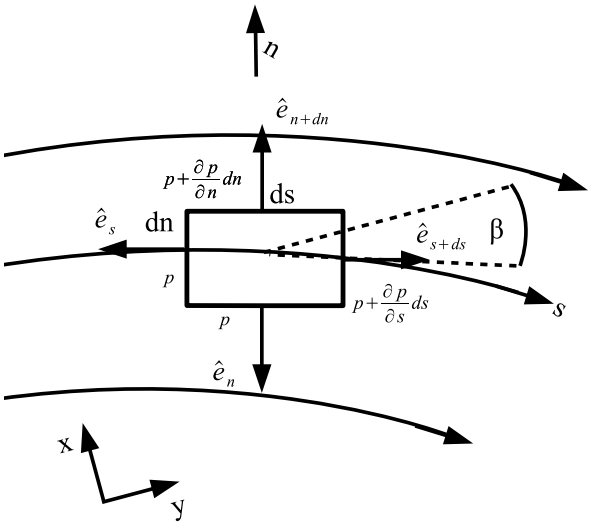

Figure 5.10: Force balance in a Lagrangian frame of reference following a fluid element of volume dV=dnds per unit of depth along a streamline; β is the angle that the stremline forms with the y axis.

The methodology followed in this chapter relies on the study of the flow streamlines. For this reason, a Lagrangian reference system (i.e. moving with the fluid) is adopted to derive the inviscid Navier-Stokes equations, known as Euler equations, that are needed to carry out the study. These equations can be better used to describe the flow near the wire.
Following a fluid element of volume dV=dnds along a streamline, the force balance in a Lagrangian reference system is defined as

$$\sum \vec{F}_{\text{ext}} = \frac{D(\text{M}\vec{v})}{Dt} \overset{\text{Def}}{=} \frac{\partial(\text{M}\vec{v})}{\partial t} + (\vec{v}\cdot\vec{\nabla})\text{M}\vec{v}, \tag{5.14}$$

where $\vec{F}_{\text{ext}}$ is the sum of external forces acting on the control volume element, $\vec{v}$ is the velocity vector, $\frac{D\cdot}{Dt}$ is the substantial (or Lagrangian) derivative, and M=ρdV is the mass of the control volume, with ρ the fluid density. If M is constant, the previous equation becomes

$$\sum \vec{F}_{\text{ext}} = \text{M}\left[\frac{\partial \vec{v}}{\partial t} + (\vec{v}\cdot\vec{\nabla})\vec{v}\right]. \tag{5.15}$$

The definition of streamline implies that the velocity vector is always tangent to the streamline, so it has no component along the normal direction n [101], therefore $\vec{v}$ can be re-written as

$$\vec{v} = U_{\text{s}}\hat{e}_{\text{s}},$$

being U_{s} the modulus of the vector and $\hat{e}_{\text{s}}$ the unit vector along the tangent direction s.
By separating the external forces along the s and n directions, Equation 5.15 becomes

$$\begin{aligned}\sum F_{\text{ext,s}}\hat{e}_{\text{s}} + \sum F_{\text{ext,n}}\hat{e}_{\text{n}} = \rho \text{dnds}\left[\frac{\partial\left(U_{\text{s}}\hat{e}_{\text{s}}\right)}{\partial t} + \left(\vec{v}\cdot\vec{\nabla}\right)\left(U_{\text{s}}\hat{e}_{\text{s}}\right)\right] = \\ = \rho\left[\frac{\partial\left(U_{\text{s}}\hat{e}_{\text{s}}\right)}{\partial t} + \frac{\partial U_{\text{s}}}{\partial s}\left(U_{\text{s}}\hat{e}_{\text{s}}\right)\right]\text{dnds}\end{aligned} \tag{5.16}$$

The sum of the external forces acting along the s direction is

$$\sum F_{\text{ext,s}} = \rho\left[\frac{\partial U_{\text{s}}}{\partial t} + \frac{\partial U_{\text{s}}}{\partial s}U_{\text{s}}\right]\text{dnds}. \tag{5.17}$$

The left-hand side term is obtained from a balance of the forces acting on the control volume along s:

$$\sum F_{\text{ext,s}} = p\text{dn} - \left(p + \frac{\partial p}{\partial s}\text{ds}\right)\text{dn} = -\frac{\partial p}{\partial s}\text{dsdn}. \tag{5.18}$$

Substituting Equations 5.17 in 5.18 leads to

$$-\frac{\partial p}{\partial s}\text{dsdn} = \rho\left[\frac{\partial U_{\text{s}}}{\partial t} + \frac{\partial U_{\text{s}}}{\partial s}U_{\text{s}}\right]\text{dsdn}, \tag{5.19}$$

which is re-written as

$$-\frac{1}{\rho}\frac{\partial p}{\partial s} = \frac{\partial U_{\text{s}}}{\partial t} + \frac{\partial U_{\text{s}}}{\partial s}U_{\text{s}}. \tag{5.20}$$

This equation describes the acceleration of an element of fluid due to the pressure gradient $\frac{\partial U_{\text{s}}}{\partial s}$ along the followed streamline. The control volume dV moves along the streamline (i.e. s direction) with no displacement along the n direction. This means that there is an equilibrium condition along n. The right-hand side terms of Equation 5.16 are entirely acting along the s direction, meaning that along n

$$\sum F_{\text{ext,n}} = 0. \tag{5.21}$$

Analogously to the balance of external forces along the s direction (Equation 5.18), a balance can be written for the n direction:

$$p\mathrm{ds}-\left(p+\frac{\partial p}{\partial n}\mathrm{dn}\right)\mathrm{ds}+\mathrm{M}\frac{U_\mathrm{s}^2}{R}=-\frac{\partial p}{\partial n}\mathrm{dsdn}+\rho\frac{U_\mathrm{s}^2}{R}\mathrm{dnds}=0, \tag{5.22}$$

where R is the radius of curvature of the streamline defined as in [106]

$$R=\left[1+\left(\frac{dx}{dy}\right)^2\right]^{3/2}\left(\frac{d^2x}{dy^2}\right)^{-1}, \tag{5.23}$$

where dx/dy is the derivative of the streamline along the stream-wise direction y. Finally, Equation 5.22 becomes

$$\frac{\partial p}{\partial n}=\rho\frac{U_\mathrm{s}^2}{R}. \tag{5.24}$$

This equation means that a streamline bends under the action of the transversal pressure gradient $\partial p/\partial n$, with the pressure decreasing towards the centre of curvature of the streamline [107]. Equations 5.20 and 5.24 constitute the Euler equations in the streamline reference frame [108]:

$$\frac{\partial p}{\partial n}=\rho\frac{U_\mathrm{s}^2}{R},\qquad \frac{\partial p}{\partial s}=\rho\left(\frac{\partial U_\mathrm{s}}{\partial t}+\frac{\partial U_\mathrm{s}}{\partial s}U_\mathrm{s}\right). \tag{5.25}$$

The reader is directed to Appendix C for a derivation of the previous set of equations by following an Eulerian approach, instead of Lagrangian.
Figure 5.11a sketches a streamline that bends as the fluid approaches the wire spacer. The main flow is along the y direction and from top to bottom in the figure. A sample of the real time-averaged streamline distribution is shown in Figure 5.11b. The streamlines are superimposed to the field of the lateral (spanwise) velocity component.
The derivative of the velocity along a streamline, $\partial U_\mathrm{s}/\partial s$, is computed as

$$\frac{\partial U_\mathrm{s}}{\partial s}=\frac{U_\mathrm{s}(i+1)-U_\mathrm{s}(i-1)}{s(i+1)-s(i-1)}, \tag{5.26}$$

with the indices $i+1$ and $i-1$ referring to the points along the streamline. This is substituted in Equation 5.25 and the pressure gradient normal to the wire ($\tilde{x}$ direction) is finally evaluated as

$$\frac{\partial p}{\partial \tilde{x}}=\frac{\partial p}{\partial n}\sin(\theta-\beta)+\frac{\partial p}{\partial s}\cos(\theta-\beta), \tag{5.27}$$

where $\theta=77^\circ$ is the wire's pitch angle with the horizontal axis (see Figure 5.11a for reference) and β is the angle that the streamline forms with the vertical (see Figure 5.11a for reference). This equation can be used to estimate the pressure gradient normal to the wire as a tool to explain the experimental results regarding the flow direction.

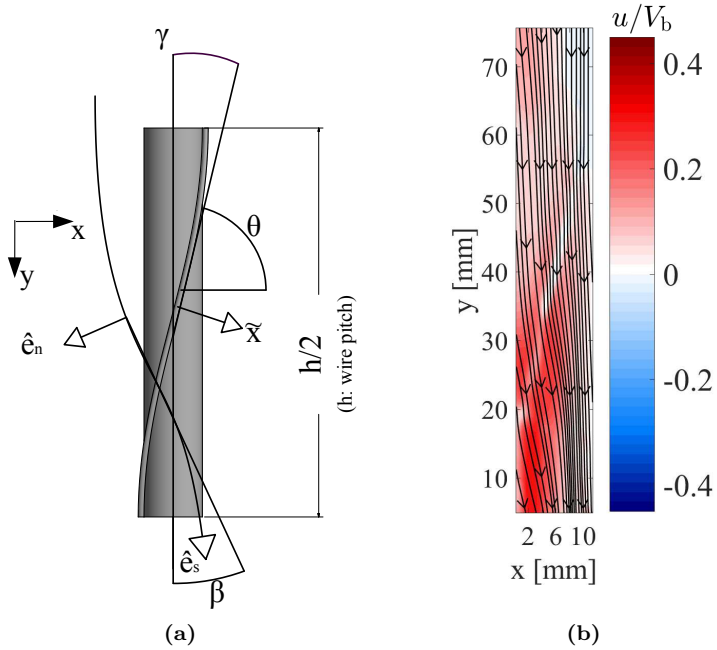

Figure 5.11: a) Deflection of a streamline near the wire spacer; the Euler equations are applied in the streamline's frame of reference $(\hat{e}_n;\hat{e}_s)$ to reconstruct the pressure gradient field normal to the wire. $\tilde{x}$ is the direction normal to the wire. b) Example of the mean velocity's streamlines superimposed to the lateral velocity component.

5.6.2 An equation for the bending of the streamlines

This section aims at deriving an equation that describes and quantifies the bending of the flow streamline due to the proximity of the wire spacer. By doing so, our understanding of the physics governing the migratory flow improves. We start from the Euler equation across a streamline (Equation 5.24) that, without gravitational effects, is

$$-\frac{U_s^2(\vec{r})}{R(\vec{r})}\hat{e}_n=-\frac{1}{\rho}\frac{\partial p(\vec{r})}{\partial n}\hat{e}_n, \tag{5.28}$$

where $\vec{r}=(x,y)$ is the position in the two-dimensional flow field.
A streamline is defined as the locus of points always tangent to the local velocity vector [101]:

$$\frac{dx}{dy}=\frac{u(\vec{r})}{v(\vec{r})} \tag{5.29}$$

where $u(\vec{r})$ and $v(\vec{r})$ are the velocity components along a streamline. For any

streamline $s=(\psi(y),y)$ it follows that

$$\frac{d\psi(y)}{dy}=\frac{u(\vec{r})}{v(\vec{r})}=\frac{U_s\sin\beta(\vec{r})}{U_s\cos\beta(\vec{r})}=\tan\beta(\vec{r}), \tag{5.30}$$

which is expressed in terms of the angle β formed by the streamline with the vertical (see Figure 5.11a). The velocity magnitude U_s is then expressed as

$$U_s^2(\vec{r})=u^2(\vec{r})+v^2(\vec{r})=v^2(\vec{r})\left[1+\frac{u^2(\vec{r})}{v^2(\vec{r})}\right]=v^2(\vec{r})\left[1+\tan^2\beta(\vec{r})\right]. \tag{5.31}$$

Upon substitution of Equation 5.31 in Equation 5.28, this becomes

$$\rho\frac{v^2(\vec{r})}{R(\vec{r})}\left[1+\tan^2\beta(\vec{r})\right]\hat{e}_n=\frac{\partial p(\vec{r})}{\partial n}\hat{e}_n. \tag{5.32}$$

Considering a single streamline $(\psi(y),y)$ and recalling the definition of R (Equation 5.23), the previous equation becomes

$$\rho v^2(\vec{r})\left[1+\tan^2\beta(\vec{r})\right]\frac{d^2\psi(y)}{dy^2}\left[1+\left(\frac{d\psi(y)}{dy}\right)^2\right]^{-3/2}\hat{e}_n=\frac{\partial p(\vec{r})}{\partial n}\hat{e}_n. \tag{5.33}$$

Following Equation 5.30 $\tan\beta(\vec{r})$ replaces the $d\psi(y)/dy$ term, hence

$$\rho v^2(\vec{r})\frac{1+\tan^2\beta(\vec{r})}{\left[1+\tan^2\beta(\vec{r})\right]^{3/2}}\frac{d^2\psi(y)}{dy^2}\hat{e}_n=\frac{\rho v^2(\vec{r})}{\left[1+\tan^2\beta(\vec{r})\right]^{1/2}}\frac{d^2\psi(y)}{dy^2}\hat{e}_n=\frac{\partial p(\vec{r})}{\partial n}\hat{e}_n. \tag{5.34}$$

The second order derivative is rearranged as

$$\frac{d^2\psi(y)}{dy^2}=\frac{d}{dy}\left(\frac{d\psi(y)}{dy}\right)=\frac{d}{dy}\tan\beta(\vec{r})=\left[1+\tan^2\beta(\vec{r})\right]\frac{d\beta(\vec{r})}{dy}, \tag{5.35}$$

and substituted into Equation 5.34, to obtain an expression linking the pressure gradient normal to the streamline with the local angle of inflection $\beta(\vec{r})$:

$$\frac{1}{\rho v^2(\vec{r})}\frac{\partial p(\vec{r})}{\partial n}=\left[1+\tan^2\beta(\vec{r})\right]^{1/2}\frac{d\beta(\vec{r})}{dy}. \tag{5.36}$$

In order to obtain $\beta(\vec{r})$, Equation 5.36 is integrated in dy on both sides along the considered streamline $s=(\psi(y),y)$. The integral is estimated between $y=-\infty$, far upstream, where the influence of the wire is negligible and the streamline is straight ($\beta=0$), and the arbitrary coordinate $y=\sigma$ along the streamline. By moving all the terms that do not contain $\beta(\vec{r})$ to the right-hand side of the equation, we get

$$\int_{-\infty}^{\sigma}\left[1+\tan^2\beta(\vec{r})\right]^{1/2}\frac{d\beta(\vec{r})}{dy}dy=\int_{-\infty}^{\sigma}\frac{1}{\rho v^2(\vec{r})}\frac{\partial p(\vec{r})}{\partial n}dy.$$

The solution of this equation is

$$\beta(y{=}\sigma){=}\int_{-\infty}^{\sigma}\frac{1}{\rho v^2(\vec{r})}\frac{\partial p(\vec{r})}{\partial n}dy. \tag{5.37}$$

For the complete derivation of the previous equation, the reader is directed to Appendix D.
Considering that $\frac{\partial y}{\partial s}{=}\cos\beta$ (see Figure 5.10), the previous equation can be rewritten as

$$\beta(y{=}\sigma){=}\int_{-\infty}^{s}\frac{1}{\rho v^2(\vec{r})}\frac{\partial p(\vec{r})}{\partial n}\cos\beta(\vec{r})ds. \tag{5.38}$$

For small β, the cosine can be neglected:

$$\beta(y{=}\sigma){=}\int_{-\infty}^{s}\frac{1}{\rho v^2(\vec{r})}\frac{\partial p(\vec{r})}{\partial n}ds. \tag{5.39}$$

This final equation gives the value of β as the result of a path integral over a streamline. The bending of the flow is the result of the interaction between the transverse pressure gradient and inertia.
In an LMFBR, the inertial term $\rho v^2(\vec{r})$ may differ from our experiments due to the different fluid properties and flow velocities through the subchannels of the core. Two cases are taken as reference to estimate such a difference: the sodium-cooled Super Phenix and the LBE-cooled MYRRHA designs. The density for sodium and LBE at operation conditions is, respectively, $\rho_{\mathrm{Na}}{=}840\,\mathrm{kg\,m^{-3}}$ at 470 °C and $\rho_{\mathrm{LBE}}{=}10\,360\,\mathrm{kg\,m^{-3}}$ at 340 °C. As for the flow speed, typical values are $5\,\mathrm{m\,s^{-1}}$ for a sodium reactor and $2\,\mathrm{m\,s^{-1}}$ for LBE. The inertial term $\rho v^2(\vec{r})$ results 5 and 10 times higher for sodium and LBE, respectively, meaning a smaller bending angle and a more straight flow. However, in a LMFBR the angle of the wire's helix might be different, affecting the $\frac{\partial p(\vec{r})}{\partial n}$ term; this is not taken into account in the comparison.
Furthermore, it is interesting to observe that the value of the bending angle at a certain coordinate s along a streamline depends on the upstream path, as indicated by the need of solving the integral. The small β approximation is accurate within an error of 5% for $\beta{\in}[0,\pi/3]$, and within 12% for $\beta{\in}[0,\pi/4]$.

5.7 Results and discussion

In the first part of this section, the results of the model based on the Euler equations are shown; they consist of the pressure gradient fields evaluated normal to the wire. These are then compared to the experimental results, being the pressure gradient field derived from the 2D Navier-Stokes equations. Finally, Equation 5.39, which predicts the bending angle β, is also compared to the experiments.

5.7.1 Pressure gradient normal to the wire predicted by the Euler equations

This section presents the reconstructed pressure gradient modelled through the Euler equation, following the approach discussed in section 5.6. Equation 5.27 is applied to the streamlines to estimate the local, non-dimensional pressure gradient normal to the wire, $\frac{2D_w}{\rho V_b}\frac{\partial p}{\partial \tilde{x}}$, where $1/2\rho V_b^2$ is the dynamic pressure, and D_w the wire diameter. Figure 5.12 shows the pressure gradient field normal to the wire, along the $\tilde{x}$ direction (see Figure 5.11a for the reference system). Figure 5.12

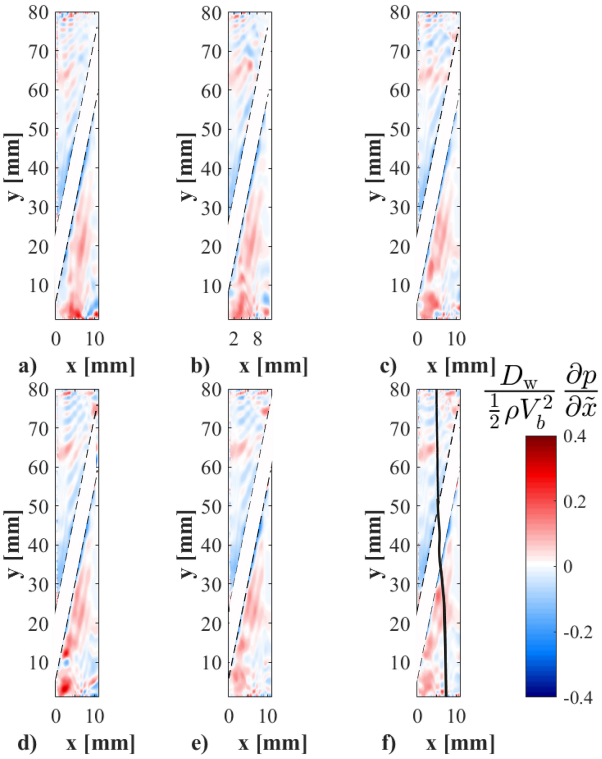

Figure 5.12: Mean non-dimensional pressure gradient normal to the wire spacer modelled through the Euler equations. The flow is from top to bottom; a) Re= 4990; b) Re=7580; c) Re=9940; d) Re=12650; e) Re=14760; f) Re=16330; an exemplifying streamline is also reported. The region over the wire is not shown due to reflection.

shows that the negative pressure gradient bends the streamlines towards the wire, leading to the lateral velocity field previously shown in Figure 5.9. Thereafter, the flow enters the downstream region, where the pressure increases with $\tilde{x}$ (positive $\partial p/\partial \tilde{x}$) throughout the recirculation region, similarly to the experiments performed by Biswas *et al.* [109] with a backward-facing step. Here the positive pressure

gradient $\partial p/\partial \tilde{x}$ straightens the streamline, decreasing thus the bending angle β. The region over the wire is not shown as it is affected by reflection coming form the metal surface.

5.7.2 Comparison with the pressure gradient predicted by the Navier-Stokes equation

The pressure gradient normal to the wire estimated by the model based on the Euler equations is compared with the solution given by the Navier-Stokes equation (Equation 5.13). Figure 5.12 shows the pressure gradient field predicted by the Euler equations, whereas the pressure gradient obtained from solving the two-dimensional Navier-Stokes equations is shown in Figure 5.13. The pressure gradi-

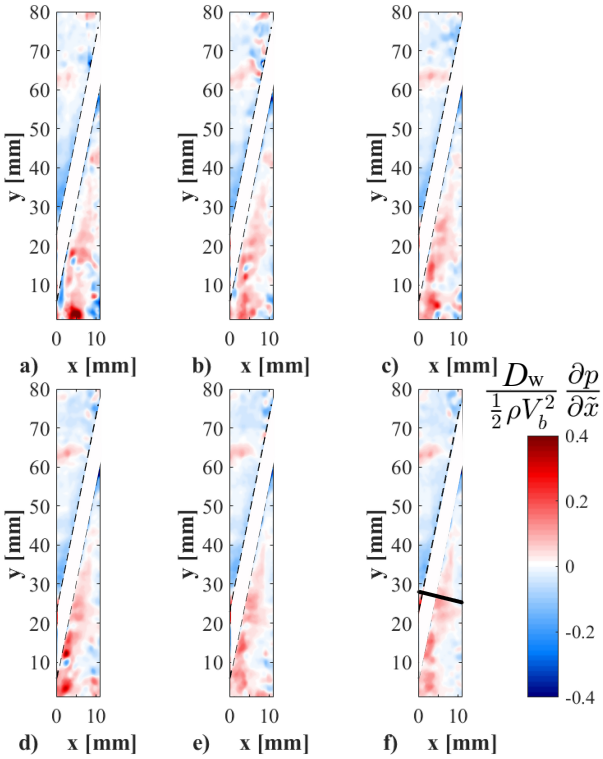

Figure 5.13: Time-averaged non-dimensional pressure gradient normal to the wire, computed from the two-dimensional Navier-Stokes equations. The flow is from top to bottom. a) Re=4990; b) Re=7580; c) Re=9940; d) Re=12 650; e) Re=14 760; f) Re=16 330; the black line is followed for extracting the numerical values for comparison. The region over the wire is not shown due to reflection.

ent normal to the wire based on the Euler equations is confirmed by the results of the Navier-Stokes equations, where the viscous effects are taken into account and

the only assumption is that the flow is two-dimensional.

A quantitative comparison is performed following a sampling line normal to the wire, drawn in Figure 5.13f, for the six investigated Reynolds numbers. Figure 5.14 shows the plot of $\frac{\partial p}{\partial \tilde{x}}$ modelled through the Euler equation (◯) and calculated from the Navier-Stokes equations (□). The abscissa $\tilde{x}$ is the coordinate over the line normal to the wire selected for the comparison. The position of the wire is also indicated for reference. The error bars associated with the model (◯) are based on the error resulting from fitting the velocity field with the streamlines. The

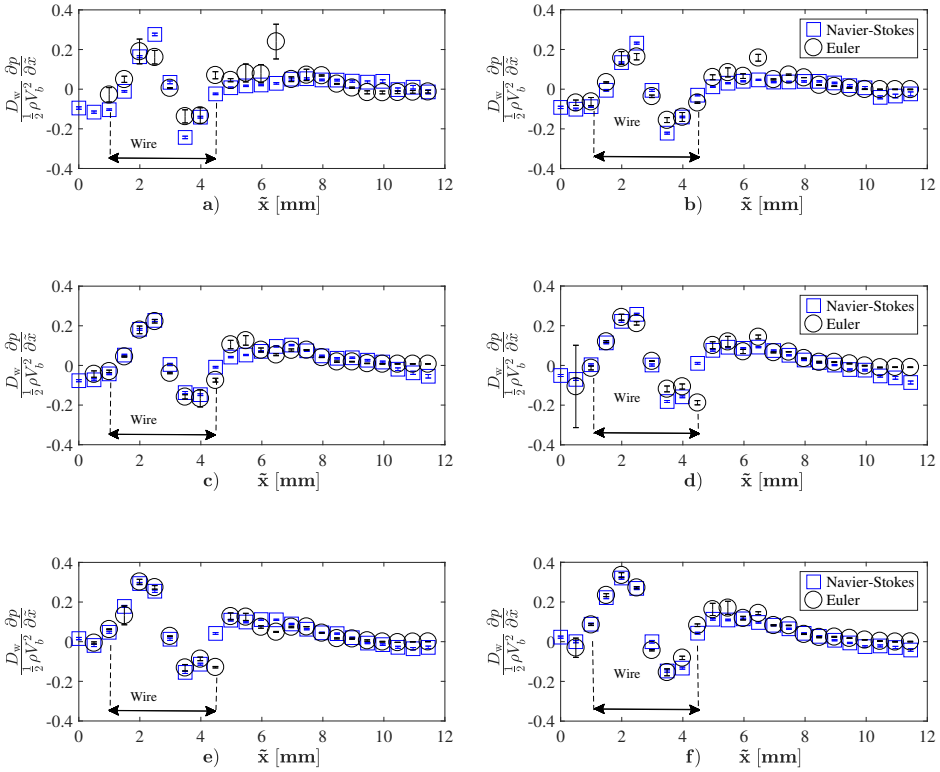

Figure 5.14: Non-dimensional pressure gradient normal to the wire predicted by the Euler equations (◯, Equation 5.27) compared to the results obtained with the Navier-Stokes equations (□, Equation 5.13). a) Re=4990; b) Re=7580; c) Re=9940; d) Re=12650; e) Re=14760; f) Re=16330.

error bars associated with the results of the Navier Stokes equations applied to the measured velocity fields (□) are based on statistical deviation around the mean value. The figure shows good agreement between the two data series indicating, thus, that the model is capable of predicting the pressure gradient caused by the wire. Moreover, the agreement between the model (where the viscous effects are neglected) and the Navier-Stokes equations (where they are included) suggests

that the viscous term does not play a significant role in such a flow.

5.7.3 Validating the predicted bending angle against the experiments

In this section the bending angle β, predicted by Equation 5.39, is compared with the angle obtained from the time-averaged velocity fields measured with PIV. Based on the measurements, β is evaluated along the streamline following Equation 5.30:

$$\beta(\vec{r}) = \arctan\left[\frac{u(\vec{r})}{v(\vec{r})}\right]. \tag{5.40}$$

The results are plotted in Figure 5.15a against the normalised coordinate s along the considered streamline (drawn in Figure 5.12).

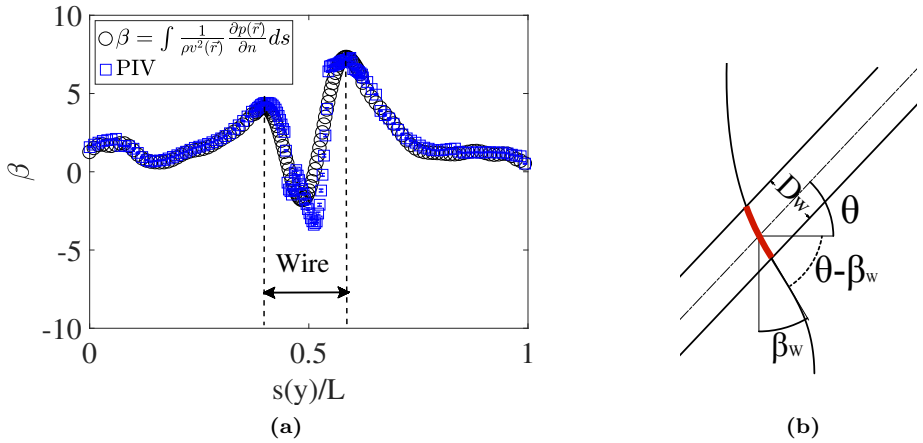

Figure 5.15: a) Bending angle β along a streamline evaluated with Equation 5.39 (◯) compared to the angle obtained from the PIV measurements (□). The abscissa is normalised by the streamline's total length. Re=16330. b) The path Γ_w of the streamline over the wire (red) is considered straight to simplify Equation 5.39; θ is the pitch angle of the wire.

The accuracy on the prediction of β is expressed as the normalised root mean square error (NRMSE):

$$\mathrm{NRMSE} = \frac{\sqrt{\frac{1}{N_s}\sum_{i=1}^{N_s}\left[\beta(i)_{\mathrm{Eq.5.39}} - \beta(i)_{\mathrm{PIV}}\right]^2}}{(\beta_{\max})_{\mathrm{PIV}} - (\beta_{\min})_{\mathrm{PIV}}}, \tag{5.41}$$

where N_s is the number of points along the streamline where the pressure gradient is evaluated, and the subscript PIV refers to the angle retrieved from the experiments. The error thus evaluated is 8%: most of the contribution to the error is located in the measured region closest to the wire, being $0.47 \leq s(y)/L \leq 0.55$, where

reflections of light coming from the metal may affect the measurement. Based on the agreement between the angle measured from the experiments and the prediction, the new expression derived for estimating β (Equation 5.39) shows that it is a valid alternative to the Euler equations for linking the pressure gradient to the corresponding bending angle β, being more easily measurable than the curvature radius.

Equation 5.39 is derived under the assumption that the viscous effects are negligible. The comparison between the model and the Navier-Stokes equations proves that this assumption is valid for these experiments, where water is the working fluid. However, this simplification may not be valid in a LMFBR.
In order to assess its validity, two reference designs are considered being Super Phenix and MYRRHA reactors, whose average core temperatures are 470 °C and 340 °C respectively. The kinematic viscosity of sodium and LBE at operation conditions is $\nu_{\mathrm{Na}}=3\times10^{-7}\,\mathrm{m^2\,s^{-1}}$ and $\nu_{\mathrm{LBE}}=1.6\times10^{-7}\,\mathrm{m^2\,s^{-1}}$. These are of the same order of magnitude as the water's viscosity in the experiments, being $8\times10^{-7}\,\mathrm{m^2\,s^{-1}}$. For both cases, the inertial forces are more important than those of the experiments, being the Reynolds number equal to 160000 and 120000 for Super Phenix and MYRRHA respectively. Therefore viscous forces are even less important when the model is applied to a liquid metal-cooled reactor.

5.8 Approximating the bending in the wire region

The bending angle of the flow can be predicted through Equation 5.39 following the path of a streamline. Limiting our attention to the wire region (red path in Figure 5.15b), β can be estimated relying on a number of assumptions that simplify the integral in Equation 5.39. Recalling Equation 5.27 for the pressure gradient normal to the wire

$$\frac{\partial p}{\partial \tilde{x}}=\frac{\partial p}{\partial n}\sin(\theta-\beta)+\frac{\partial p}{\partial s}\cos(\theta-\beta), \tag{5.42}$$

the contribution of the $\partial p/\partial s$ term is negligible compared to the $\partial p/\partial n$ term: from a comparison it appears that this term is three orders of magnitude smaller than $\partial p/\partial n$ throughout the entire path of the streamline. This means that the accelerating force along the streamline is negligible compared to the centripetal one responsible for the bending of the streamline. Hence the following approximation is done:

$$\frac{\partial p}{\partial \tilde{x}}\approx\frac{\partial p}{\partial n}\sin(\theta-\beta).$$

It follows that the pressure gradient normal to the wire is

$$\frac{\partial p}{\partial n}\approx\frac{\partial p}{\partial \tilde{x}}\frac{1}{\sin(\theta-\beta)},$$

which can be substituted in Equation 5.39 derived in the previous section, leading to

$$\beta(y{=}\sigma){=}\int_{-\infty}^{s}\frac{1}{\rho v^2(\vec{r})\sin[\theta-\beta(\vec{r})]}\frac{\partial p(\vec{r})}{\partial\tilde{x}}ds.$$

The previous integral is split into two parts, being

$$\beta(y{=}\sigma){=}\int_{-\infty}^{\text{lead.}}\ldots ds+\int_{\text{lead.}}^{\text{trail.}}\ldots ds,$$

where the two extremes of integration refer to the position of the leading (lead.) and trailing (trail.) edge of the wire along a streamline.
The second approximation consists of linearizing the pressure gradient in the second integral across the wire of diameter D_{w}:

$$\left(\frac{\partial p}{\partial\tilde{x}}\right)_{\text{w}}\approx\frac{(\Delta p)_{\text{w}}}{D_{\text{w}}},\tag{5.43}$$

where $(\Delta p)_{\text{w}}$ is the pressure drop across the wire in the perpendicular direction. This can be expressed as

$$(\Delta p)_{\text{w}}{=}\frac{1}{2}\rho C_{\text{p}}U_{\perp}^2,\tag{5.44}$$

being C_{p} a local drag coefficient and $U_{\perp}$ the velocity perpendicular to the wire. This linearization leads to

$$\beta(y{=}\sigma){=}\int_{-\infty}^{\text{lead.}}\ldots ds+\frac{C_{\text{p}}U_{\perp}^2}{2D_{\text{w}}}\int_{\text{lead.}}^{\text{trail.}}\frac{1}{v^2(\vec{r})\sin[\theta-\beta(\vec{r})]}ds,\tag{5.45}$$

which, with $\theta\gg\beta$ (see Figure 5.11 as an example), simplifies into

$$\beta(y{=}\sigma){=}\int_{-\infty}^{\text{lead.}}\ldots ds+\frac{C_{\text{p}}U_{\perp}^2}{2D_{\text{w}}\sin\theta}\int_{\text{lead.}}^{\text{trail.}}\frac{1}{v^2(\vec{r})}ds.\tag{5.46}$$

Figure 5.15b sketches the path followed by a streamline across the wire. For a cylinder lying on a flat plate in the presence of a flow in the perpendicular direction, Bearman *et al.* [110] measured a value of the pressure coefficient C_{p} of 0.5, which accounts for the pressure drop in the wake of the cylinder. Since the wire is small compared to the rod, it can be locally approximated to a cylinder on a flat plate, and C_{p} can be used for the estimation of β. The velocity perpendicular to the wire is calculated as

$$U_{\perp}{=}U_{\infty}\cos\theta,\tag{5.47}$$

being U_{∞} the free stream velocity evaluated far upstream of the wire. The β angle at the trailing edge of the wire is finally evaluated as

$$\beta(y{=}\sigma){=}\int_{-\infty}^{\text{lead.}}\frac{1}{\rho v^2(\vec{r})\sin\theta}\frac{\partial p(\vec{r})}{\partial\tilde{x}}ds+\frac{C_{\text{p}}(U_{\infty}\cos\theta)^2}{2D_{\text{w}}\sin\theta}\int_{\text{lead.}}^{\text{trail.}}\frac{1}{v^2(\vec{r})}ds,\tag{5.48}$$

which yields β=6.5°, whereas the measured angle is 7.4°, corresponding to an error of 14%. The difference between the values can be ascribed to the geometry where C_p is measured, which differs from the wire-wrapped rod case, being a cylinder lying on a flat plate. Moreover, the approximation $\theta \gg \beta$ could also have an effect on the final result. Nevertheless, Equation 5.48 could be a first step towards a correlation that estimates the bending of the flow near the wire based on macroscopic variables. In fact, this equation could also be used to estimate the pressure drop across a wrapping wire based on the value of the β angle, which can be obtained from the streamline field.

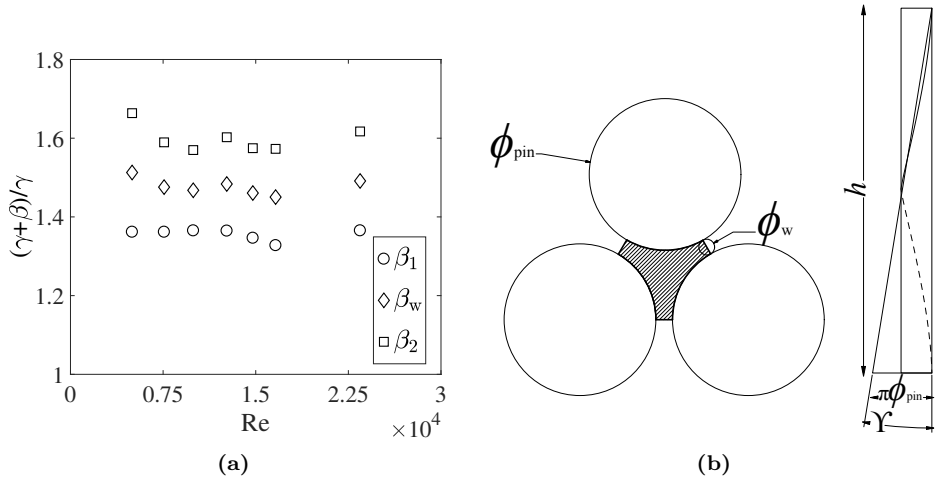

Figure 5.16: a) Bending angle measured upstream (β_1), downstream (β_2) of the wire, and mean value (β_w). The wire's pitch angle with the vertical axis γ=13° is determined from $\tan\gamma = \pi\phi_{pin}/h$. b) Triangular subchannel: the hydraulic diameter ϕ_h is based on the main subchannel area (hatched).

PIV measurements of the flow in front of the wire are disturbed by the reflection of the light by the metal, thus β is measured at two points located respectively at the leading edge (β_1) and at the trailing edge (β_2) of the wire, 12 mm apart. β is measured at these two locations as the angle formed by the streamline with the vertical axis. The measurement is repeated for all the investigated Reynolds numbers, and the results are reported in Figure 5.16. The plot shows that β does not strongly depend on the flow rate, for $Re \geq 7580$ (note that this condition could be already reached for $4990 < Re \leq 7580$). The near-constant trend of β shown in the figure means that the ratio between the velocity components u and v remains constant as well ($\tan\beta \equiv u/v$), although the single components change with the Reynolds number. Thus, the flow rate does not affect the direction of the flow, as

concluded also by Song *et al.* [45].

5.9 Estimating the bending with dimensional analysis

The expression derived for estimating the bending angle of the flow (Equation 5.39) depends on the characteristics of the flow field (velocity components and flow streamlines). It follows directly from theory and it has its roots in the physics of the Euler equations. However, it may be useful to develop a correlation to predict such an angle based on macroscopic variables such as the design parameters of the rod bundle (rod diameter, wire diameter, wire pitch, fluid properties).
The bending angle across the wire, β_w, can be derived from dimensional analysis. The considered geometry is a triangular subchannel of an arbitrary wire-wrapped, hexagonal rod bundle (Figure 5.16b). The velocity components u and v that determine the bending angle are affected by the geometry of the channel, accounted for in the hydraulic diameter term ϕ_h, the fluid properties ρ and μ, the bulk velocity V_b, the angle of the helicoid wire Υ and the wire diameter ϕ_w. The angle can, thus, be written as a function of these variables as

$$\tan\beta_w \equiv \frac{u}{v} = \left(h/\phi_{pin}\right)^{b_1} \cdot \rho^{b_2} \cdot \mu^{b_3} \cdot \phi_h^{b_4} \cdot V_b^{b_5} \cdot \phi_w^{b_6}, \tag{5.49}$$

where h/ϕ_{pin} is the ratio between the wire wrapped pitch and the rod diameter, commonly used in wire-wrapped rod bundles, and related to the helicoid angle Υ through

$$\tan\Upsilon = \pi\frac{\phi_{pin}}{h},$$

being Υ defined in Figure 5.16b. For a given ϕ_{pin} and ϕ_w, the P/D ratio determines the hydraulic diameter ϕ_h of the subchannel containing the wire [89]:

$$\phi_h = \frac{2\sqrt{3}\phi_{pin}^2 (P/D)^2 - \pi\left(\phi_{pin}^2 + \phi_w^2\right)}{\pi\left(\phi_{pin} + \phi_w\right)}. \tag{5.50}$$

The dimensional analysis of Equation 5.49 yields the following expression:

$$[-] = [-]^{b_1} \cdot \left[\mathrm{kg\,m^{-3}}\right]^{b_2} \cdot \left[\mathrm{kg\,m^{-1}\,s^{-1}}\right]^{b_3} \cdot [\mathrm{m}]^{b_4} \cdot \left[\mathrm{m\,s^{-1}}\right]^{b_5} \cdot [\mathrm{m}]^{b_6}, \tag{5.51}$$

from which the following system of equations can be written:

$$\begin{cases} b_1 = 1 \\ b_2 + b_3 = 0 \\ -3b_2 - b_3 + b_4 + b_5 + b_6 = 0 \\ -b_3 - b_5 = 0 \end{cases} \tag{5.52}$$

The solution of the system gives the following correlation:

$$\tan\beta_w = \frac{h}{\phi_{pin}} Re^{b_3} \left(\frac{\phi_w}{\phi_h}\right)^{b_6}. \tag{5.53}$$

Experimental evidence from this work shows that β_w is not a function of the Reynolds number (Figure 5.16a) meaning that $b_3 \approx 0$, simplifying the previous equation into

$$\tan\beta_w = \frac{h}{\phi_{pin}} \left(\frac{\phi_w}{\phi_h}\right)^{b}. \tag{5.54}$$

The value of the exponent b is determined as

$$b = \frac{\ln\left(\frac{\phi_{pin}}{h}\tan\beta_w\right)}{\ln\left(\phi_w/\phi_h\right)}. \tag{5.55}$$

Substituting the dimensions of SEEDS-2 experimental setup (table 3.2) in the previous formula yields

$$b = \frac{\ln\left(\frac{D}{h}\tan\beta_w\right)}{\ln\left(D_w/D_h\right)} \approx 4.6, \tag{5.56}$$

where D, h, D_w and D_h are the dimensions of this work's bundle, and β_w is the mean value of the bending angle measured from the experiments.
The narrowness of the subchannel is taken into account through the ratio ϕ_w/ϕ_h. If P/D is given, the ratio ϕ_w/ϕ_{pin} is also fixed. For example, a hexagonal rod bundle with P/D of 1.11, such as the one of this research, yields $\phi_w/\phi_h = 0.35$, independently from the diameter of the wire and rod.
The pitch angle Υ is defined as $\tan\Upsilon = \pi\phi_{pin}/h$. It follows that hexagonal bundles with the same P/D ratio and γ (hence the same h/ϕ_{pin} ratio) should bend by the same amount close to the wire spacer. Note that these findings are valid for a geometry of the triangular subchannel where the wire is in contact with the adjacent rod (see Figure 5.16b), as in the case of the experimental setup of this work.

To the author's knowledge, there is no other study from literature that focuses on measuring the bending angle induced by the wire spacer. The correlation presented in this section is the first step towards a more general form. Validating this correlation would thus require to modify the geometry of the setup and repeat the experiments to assess the influence of the individual parameters such as P/D, wire pitch, and wire diameter. However, this was not possible for this research. Nevertheless, an attempt at quantifying the uncertainties on this correlation shows that the error on the predicted β_w is 5% (for the estimation of the error, the reader is directed to Appendix E).

5.10 Summary

This chapter described the work that aimed at modelling and explaining the migratory flow close to the helicoid wire spacer inside a 7-rods, wire-wrapped hexagonal bundle by reconstructing the pressure gradient in the direction normal to the wire. Experiments have been performed inside the rod bundle, where the axial flow has been investigated with PIV, making use of a refractive index-matching technique to reduce refraction of light inside the test section. Six Reynolds numbers were considered while measuring the time-averaged velocity fields.

The results show that the flow downstream the wire followed the helicoid path, as expected. However, if the investigated region was moved to the front of the wire, closer to the bulk of the subchannel, the flow changed the direction by moving against the wire's helicoid path. The pressure gradient normal to the wire has been modelled through the Euler equations applied to the streamlines, thereby showing that the bending of the flow is caused by the pressure gradient imposed by the wire.

The results modelled through the Euler equations were compared with the solution of the two-dimensional Navier-Stokes equations leading to a good qualitative and quantitative agreement. Furthermore, an expression to predict the bending angle of the flow has been derived and successfully validated against the experimental results.

The findings presented in this chapter give more insight into the physics governing the bending of the flow close to the wire spacer, highlighting how the flow bending is the result of the interaction between the transverse pressure gradient and inertia of the flow. The model hereby presented leads the way to future possibilities for evaluating the bending angle through macroscopic, known variables such as bundle dimensions and flow rate. In this regard, a correlation based on dimensional analysis, and supported by experimental fidings, has been proposed to estimate the bending angle from the dimensions of the bundle (diameter of wire and rod, P/D ratio, and helicoid wire pitch).

5.11 Nomenclature

Symbols	Description	Units
A	Flow area	m^2
b_1, b_2, b_3, b_4, b_5, b_6	Exponents of the dimensional analysis	–
C_p	Local drag coefficient	–
D_h	Hydraulic diameter	m
D_w, $D_{w,p}$	Wire diameter, and in pixel respectively	mm
$\hat{e}_n$, $\hat{e}_s$	Normal and tangential unit vectors in the streamline's frame of reference	–
F	mm-to-pixel conversion factor	$mm\,px^{-1}$
$\vec{F}_{ext}$	External forces acting on a volume of fluid	N
$f_\#$	Lens aperture	–
h	Helicoidal wire pitch	mm
i, j, τ	Indices	–
L	Streamline's length	mm
N	Number of recorded frames	–
N_s	Number of points along a streamline	–
n, s	Indices pertaining to the normal and tangential coordinate along a streamline	–
M	Mass of fluid	kg
M_0	Magnification factor	–
P/D	Ratio between the pitch and the diameter of the half rods	–
P_w	Wetted perimeter	m
p	Pressure	Pa
$(\Delta p)_w$	Pressure drop across the wire	Pa
Q	Volumetric flow rate	$m^3\,s^{-1}$
R	Radius of curvature	m
$\vec{r}$	Vector of position	m
v_i, $\bar{v}$	Instantaneous and mean velocity	$m\,s^{-1}$
$\vec{v}$	Velocity vector	$m\,s^{-1}$
V_b	Bulk velocity	$m\,s^{-1}$
dV	Control volume	
δD_w	Uncertainty on the wire diameter	mm
$\delta D_{w,p}$	Uncertainty on the wire diameter in pixels	px
T	Temperature	°C
t	Time	s
dt, Δt	Time interval between two consecutive frames, and two consecutive images	s
U_s	Velocity tangent to the streamline	$m\,s^{-1}$
$U_\perp$	Velocity component perpendicular to the wire	$m\,s^{-1}$
U_∞	Free stream velocity, far upstream of the wire	$m\,s^{-1}$
u	Span-wise (transversal) velocity component	$m\,s^{-1}$

x, y, z	Span-wise (transversal), stream-wise (vertical), and normal directions	m
Δx, Δy	Transversal and vertical separation interval between velocity vectors	m
$\tilde{x}$	Coordinate normal to the wire	m
δz	Depth of focus	mm

Greek letters	**Description**	**Units**
β	Bending angle of the streamline	$^\circ$
β_1, β_2	Bending angle of the streamline measured upstream and downstream of the wire	$^\circ$
β_{Max}, β_{min}	Maximum and minimum angle of bending along the path of a streamline	$^\circ$
β_{w}	Mean bending angle of the streamline across the wire	$^\circ$
Γ_{w}	Path followed by a streamline over the wire	m
γ	Helicoid wire angle of SEEDS-2 facility	$^\circ$
Δ_{p}	Particle displacement between two consecutive images	pixel
θ	Angle formed by the wire with the horizontal	$^\circ$
λ_{l}	Wavelength of the laser	nm
ν, ν_{LBE}, ν_{Na}	Kinematic viscosity of water, lead-bismuth eutectic, and sodium	$\mathrm{m^2\,s^{-1}}$
ρ, ρ_{LBE}, ρ_{Na}	Density of water, lead-bismuth eutectic, and sodium	$\mathrm{kg\,m^{-3}}$
σ_{stat}, σ_{syst}	Statistical and systematic errors on the measurements	$\mathrm{m\,s^{-1}}$
$\sigma_{\overline{v}}$	Mean error on the measurements	$\mathrm{m\,s^{-1}}$
Υ	Helicoid wire angle of a generic hexagonal bundle, wire-wrapped facility	$^\circ$
ϕ_{pin}, ϕ_{w}, ϕ_{h}	Pin diameter, wire diameter, and hydraulic diameter of the subchannel of a generic hexagonal bundle, wire-wrapped facility	m

Acronyms	**Description**
AOI	Area of interest
CMOS	Complementary Metal-Oxide Semiconductor
FEP	Fluorinated Ethylene Propylene
LBE	Lead-bismuth eutectic
LMFBR	Liquid Metal Fast Breeder Reactor
MYRRHA	Multi-purpose hYbrid Research Reactor for High-tech Applications
NRMSE	Normalised Root Mean Square Error
PIV	Particle Image Velocimetry
SEEDS-1	SEven rods Experiments in Delft for Sesame-1
SEEDS-2	SEven rods Experiments in Delft for Sesame-2

Non dimensional groups	**Description**
Re	Reynolds number

Chapter 6

Conclusions and recommendations

When this research started only one correlation was available for predicting the length of coherent structures in bundle geometries; however this had been developed for a rather specific shape of the channel, lacking thus general validity. This work proposes, thus, a correlation applicable to different geometries, including full rod bundles.
Literature is rich in experimental works on Fluid-Structure Interaction (FSI) with rod bundle geometries. However, an experimental study that specifically addressed the role of coherent structures in inducing vibrations inside rod bundles was still missing. For that reason, this research aimed at providing, and provides, novel experimental evidence regarding vibrations induced by coherent structures on the rods of a bundle.
Migratory flow was first observed in the seventies in rod bundles with helicoid wire spacers. A rather general explanation was proposed, which ascribed the phenomenon to the hydraulic resistance caused by the wire inside the subchannel. Only recently, was a numerical study conducted that partially focussed again on the effect of migratory flow. However literature was still missing any attempt to model this phenomenon, which therefore became one of the goals of this research.

This experimental research focusses on large coherent structures in rod bundles, their contribution to flow-induced vibrations (FIV), and the so-called migratory flow observed in hexagonal rod bundles with wire spacers wrapped around the rods. To these purposes, three experimental facilities have been designed and built. A rectangular channel hosting two half-rods, and two 7-rod hexagonal bundles: one hosting a flexible rod for FSI experiments, and the other featuring helicoid wires wrapped around the rods to investigate migratory flow. Laser Doppler Anemometry (LDA), Particle Image Velocimetry (PIV), and a high speed camera have been used in combination with the refractive index-matching technique (RIM) to achieve optical access near the measured area. The experiments have been conducted with water as working fluid, in isothermal conditions and ambient pressure.

Large coherent structures have been detected in the gap between the rods, suggesting a lateral movement of these structures across the subchannels (cross-flow). The measurements have shown that this phenomenon has a threshold in the Reynolds number, above which cross-flow through the gap region has not been detected. This is also confirmed by previous numerical works performed at similar values of the Reynolds number for an annular gap. A similar threshold effect of the Reynolds number has been observed when considering the velocity difference (% bulk velocity) between bulk and gap regions of the channel. This velocity difference increases below the same threshold value of Reynolds, whereas it becomes constant at higher Reynolds numbers.
Coherent structures carried by the flow in the axial direction of the bundle synchronise with the flow-induced oscillations of the flexible rod, leading to an increased amplitude of the rod's oscillation.
Based on experiments and on physical reasoning, our understanding of what determines the size of coherent structures has improved. This research shows that the wavelength is a function of the hydraulic diameter of the main channel where the bulk flow is found, and of the local hydraulic diameter, being this defined by the gap flow area. In fact, the wavelength appears to be function of their ratio, thereby depending on the velocity difference between the two regions. This study has eventually led to a new correlation for estimating the size of coherent structures, which has been tested against the experiments conducted in several geometries.
Migratory flow has been explained as the result of the pressure gradient induced by the wire in the fluid that bends the flow. Moreover, deriving a theoretical model to explain such a phenomenon has increased our understanding of the physics at play. The model shows that the bending is the result of the interaction between the pressure gradient and the inertial forces applied to the fluid.

The remainder of this chapter describes in more detail the conclusions of this research, and ultimately provides recommendations for future works to address some still unanswered questions.

6.1 Coherent structures in a compound channel

The flow of coolant through the core of a nuclear reactor can generate large coherent structures that can be beneficial to the safety of the core as they prevent hot spots on the cladding of the fuel elements. Designing safer and more efficient nuclear reactors requires that some questions regarding these coherent structures be addressed, such as

How do Reynolds number and gap width affect the behaviour of coherent structures in a gap geometry?

To answer these questions, a facility has been assembled consisting of a rectangular

channel hosting two half-rods facing each other; the idea of such a setup originated from the work of Mahmood [17]. Owing to the relative easiness of access to the measured region, this setup allowed for detailed measurements of the flow in the gap between the rods. The gap width between the half-rods could be adjusted to 1, 2, or 3 millimeter, corresponding to a pitch-to-rod diameter ratio of 1.07, 1.13, or 1.20. The flow between the rods has been measured with LDA, a non-intrusive optical measurement technique, within the Reynolds number range $600 - 29\,000$. Optical access to the gap region has been achieved by making one of the rods of Fluorinated Ethylene Propylene (FEP), a refractive index-matching material with nearly the same refractive index of water.
Large coherent structures carried by the flow near the gap, also known as gap vortex streets, have been measured from the analysis of the time-dependent signal of the velocity components. Their axial length is estimated through the Taylor hypothesis, which regards these structures as "frozen" entities carried by the flow with a convection speed lower than the bulk velocity. The measurements have shown that the length of the structures is not a function of the Reynolds number above a certain value of this, and that their length tends to an asymptotic value. The velocity difference between the bulk flow and the centre of the gap (% bulk velocity), which is the driving force of coherent structures, becomes also independent of the Reynolds number above a certain threshold. This might explain why the wavelength is not affected by the Reynolds number.
However, for lower values of the Reynolds number, coherent structures become longer, extending farther into the bulk of the main subchannels, suggesting a possible growth also in the lateral direction due to the extending of the region where the average velocity changes. This could be due to the widening shear layer region between the gap and the bulk, similarly to wall-bounded flows with decreasing Reynolds number. Measurements with different P/D ratio have also shown that coherent structures become longer with increasing gap width.
Cross-flow of coherent structures across the gap has been revealed by periodicities in the span-wise (lateral) velocity component measured near the centre of the gap, showing that the frequency of cross-flow decreases with larger gaps.
The plot of the stream-wise velocity root mean square has shown the presence of an additional peak in the middle of the gap, which occurs below a certain value of the Reynolds number. This threshold effect can be related to the velocity difference between the main channel and the gap, which is the driving force of coherent structures, and which becomes larger below the same threshold value of Reynolds. The peak in the velocity root mean square measured at the centre of the gap can indicate cross-flow of structures across the gap, which increase the turbulence level in this region.

6.2 Size of large coherent structures in rod bundle geometries

The size (i.e. the wavelength) of large coherent structures occurring in a rod bundle has a direct impact on the design of the core of a nuclear reactor. Their size

affects the lateral mixing across the subchannels, as shown by Mahmood [17], and estimating the length of these structures is important for flow-induced vibration (FIV) studies. When this research started there was one correlation available in literature provided by Guellouz and Tavoularis [19] to estimate the wavelength based on the geometry of the subchannel. However, this correlation was based on the rather specific case of a solitary rod inside a rectangular channel with an axial flow. Hence, the following question was put forward:

What is the form of a new correlation based on experimental evidence and physical reasoning valid for rod bundles?

Such a correlation has been derived starting from dimensional analysis, and further developed relying on experiments conducted in the rectangular channel hosting two half-rods (P/D=1.07, 1.13, 1.20) and the 7-rod hexagonal bundle (P/D=1.11) of this work. In its most general form, the correlation predicts that the wavelength is function of the Reynolds number limited to the gap flow area, and of the ratio between the hydraulic diameter of the gap region and the main channel connected to the gap:

$$\frac{\lambda}{D_{\mathrm{h}}^{*}}=\mathscr{K}'\left(\frac{D_{\mathrm{h}}^{*}}{D_{\mathrm{h}}}\right)^{\xi} Re_{\mathrm{gap}}^{\zeta}.$$

Experiments have shown that the wavelength of coherent structures does not change with the Reynolds number. The new correlation has also been tested on data retrieved from other channel geometries available in literature. These included a rectangular channel hosting a half-rod with two values of the gap size (P/D=1.10, 1.14), a rectangular channel hosting a rod with four gap sizes (P/D=1.02, 1.05, 1.07, 1.10), and a sector of circular rod bundle (P/D=1.15). Within the range of $D_{\mathrm{h}}^{*}/D_{\mathrm{h}}$ ratio defined by these considered geometries, the correlation assumes a simpler form. Namely, it predicts that the wavelength scales linearly with the hydraulic diameter of the gap region D_{h}^{*}, defined by the flow area bounded by the gap:

$$\frac{\lambda}{D_{\mathrm{h}}^{*}}\approx 13.$$

According to this expression, the size of coherent structures depends on the shape of the gap, whereas the main channel to which this is connected does not seem to have any influence. This correlation is valid within an error of 9% in the Reynolds number range $2000-108\,000$, and for the P/D range of $1.02-1.20$. Moreover, the tests on different geometries have shown that the correlation is applicable not only to rod bundles, but also to other geometries. For low Reynolds numbers, experimental evidence has shown that the length of coherent structures may depend on the Reynolds number. In fact, the structures become longer when the Reynolds number decreases to low values. This suggests that the term $Re_{\mathrm{gap}}^{\zeta}$ is not negligible at low Reynolds numbers, and that the exponent could be negative.

6.3 Vibrations induced by gap vortex streets

Coherent structures forming in the flow may enhance the heat exchange between the fuel pins and the coolant of a nuclear reactor. However, these structures might trigger vibrations of the fuel rods due to the oscillation that they cause in the flow. This could cause structural damage to the fuel element's cladding through fretting and fatigue. In rod bundles, vibrations induced by periodical vortices in a transversal flow have been thoroughly studied. In axial flows, however, their role was still unclear. Hence the following question was formulated:

What is the role of coherent structures in inducing vibrations in a rod bundle with axial flow?

To answer this question, optical measurements have been conducted in a 7-rod hexagonal bundle with P/D=1.11. The flow has been measured with LDA to detect coherent structures and calculate their frequency. Displacements and frequency of oscillation of the central rod, made of silicone, have been measured with a high speed camera. Optical access has been achieved by using FEP as refractive index-matching material for the outer rods of the bundle.
The experiments show that the frequency of coherent structures moving axially along the bundle increases linearly with the Reynolds number, meaning that the structures move faster as the flow rate is increased.
If coherent structures move in the axial direction with a frequency that is twice the first natural frequency of the rod (i.e. f_{y}=$2f_{\mathrm{sil,n}}$), the rod oscillates with a frequency equal to its natural frequency. As coherent structures are entities carried by the flow, their stream-wise frequency f_{y} increases with the bulk flow velocity. When f_{y} reaches the value of f_{y}=$2f_{\mathrm{sil,n}}$, there is synchronisation between the rod and coherent structures.

6.4 Migratory flow in a rod bundle with wire spacers

The core of a liquid metal-cooled reactor typically employs wire spacers as a solution to prevent fuel elements from touching each other. These wires are wrapped helicoidally around the rods to enhance the mixing of coolant (hence heat removal) and to avoid hot spots on the fuel cladding. Due to the presence of this additional component, the flow inside a rod bundle is very complex to understand and to model. In 1976, Ohtake *et al.* measured the flow inside a 37-rod, wrapped-wire hexagonal bundle by means of hot wire anemometry. They observed that the flow near the wire bent transversally against the wrapping direction of the wire. The phenomenon was called migratory flow and ascribed to the hydraulic resistance caused by the wire inside the considered subchannel. The numerical work of Song *et al.* [45] suggested that this was caused by a pair of counter-rotating vortices forming downstream of the wire. However, a physical model and a general understanding of migratory flow was still missing.

Can migratory flow be explained and modelled to predict the associated bending angle of the flow close to the wire spacer?

To answer this question, a model has been derived following a theoretical approach to predict the pressure gradient and the bending of the flow. Then the predicted results have been compared with the experiments performed in the 7-rod, wire-wrapped hexagonal bundle by means of planar PIV, for several values of the Reynolds number.
The model for the pressure gradient has been derived from the steady state, two-dimensional, inviscid Navier-Stokes equations applied to the flow streamlines, and successfully validated against the results based on the experiments.
An equation for estimating the bending angle of the flow at an arbitrary point along a streamline has been derived and compared with the measurements. The bending angle is expressed as an integral along the streamline, upstream of the considered point s:

$$\beta(\vec{r}) = \int_{-\infty}^{s} \frac{1}{\rho v^2(\vec{r})} \frac{\partial p(\vec{r})}{\partial n} ds.$$

The underlying meaning of this equation is that the bending of the flow is the result of the interaction between the pressure gradient normal to the streamline $\partial p(\vec{r})/\partial n$, which bends the streamline, and the inertial force acting on the fluid $\rho v^2(\vec{r})$, which tends to straighten the flow back.
The measurements have shown that the flow close to the wire follows the helicoid path in the downstream region. If the measurement region is shifted closer to the main subchannel, however, the flow bends towards the wire, against the helicoid path, suggesting the presence of migratory flow.
The bending angle measured on the flow streamlines does not depend on the Reynolds number, above a certain threshold. It follows that the ratio between the lateral and axial velocity components u/v is also independent of the Reynolds number, since this ratio is linked to the bending angle by the definition of streamline.
Furthermore, a correlation for estimating the angle by which the flow bends close to the wire has been derived based on experiments and through dimensional analysis:

$$\tan\beta_{\mathrm{w}} = \frac{h}{\phi_{\mathrm{pin}}} \left(\frac{\phi_{\mathrm{w}}}{\phi_{\mathrm{h}}} \right)^{b}.$$

This correlation is different from the integral previously shown because it depends on macroscopic variables such as the dimensions of the bundle (wire and rod diameter), the wire pitch, and the geometry of the subchannel through the hydraulic diameter. The correlation predicts that the flow through bundles characterised by the same P/D ratio and helicoid pitch angle should bend by the same amount close to the wire spacer. This represents a first step towards a more general expression that links the bending of the flow to the parameters of the hexagonal lattice and to the flow rate.

6.5 Perspectives

One of the main limitations of this research, concerning with FSI, is that the flow and the oscillations of the rod could not be measured at the same time. The LDA system requires a dark background to enhance the dection of the seeding particles (hence the local velocity) added to the fluid. On the other hand, measuring the oscillations induced on the rod require a powerful flashlight to improve the contrast between the white silicone rod and the darker surrounding fluid. Measuring simultaneously the flow field and the oscillations of the rod would give more insight into the mutual interplay between the vibrating rod and the coherent structures occurring in the flow. Future research should then address this issue, for example by installing accelerometers on the rod surface that do not interfere with the requirements for measuring the flow.

The effect that the oscillating rod has on the surrounding fluid would lead to a better understanding of the coupling between the rod and coherent structures that may occur in the flow. In this research, flow measurements have been conducted only in the presence of the vibrating rod. For future works, it is thus encouraged that flow measurements be performed first without any moving body, and then in the presence of the oscillating rod. The effect that vibrations may have on coherent structures could thus be evaluated.

The research described in Chapter 4 focused on measuring the displacements of only one edge of the silicone rod due to the limited resolution of the high speed camera. Measuring both edges at the same time can be helpful to know more about the mode of vibration of the rod. For example, the instantaneous displacement of the two edges could be compared by means of cross-correlation to understand if the rod oscillates in a beam mode or in a shell mode (for example with the edges moving inward and outward at the same time). Adding one camera would also make possible to measure the out-of-plane displacement of the rod, which has not been possible in this work.

Temperature fluctuations of the coolant through the core of a fast nuclear reactor might lead to deformation or bending of the fuel elements due to different thermal expansion of the cladding, as discussed by Hartig [111]. The bent fuel elements would, in turn, confine the flow even more inside some of the surrounding subchannels, which would lead to a further deterioration of the heat transfer. This would trigger a self-sustaining, oscillatory mechanism that, on the long term, could lead to mechanical fatigue on the rods. This phenomenon was observed in the sodium-cooled KNK-II pilot plant in Germany, as reported by Heinecke [112]. For this reason, it would be interesting to measure coherent structures and flow-induced vibrations inside a bundle hosting a central off-centred rod (i.e. closer to some of the surrounding rods) to deformed rod case. The correlation derived in this research predicts that the eccentric rod could cause coherent structures to shorten due to the decreased hydraulic diameter of the gap region. This would eventually increase the frequency of coherent structures in the fluid, thereby affecting the interaction with the rods.

The experimental results shown in Chapter 5 suggest that migratory flow transfers

fluid from the near-gap region towards the main subchannel. At the same time, measurements of the flow closer to the rod have shown that the fluid follows the wire, moving from the main subchannel towards the gap. For a nuclear reactor, this combined effect is important because it transfers hotter fluid from the low-speed gap region to the bulk of the subchannel. At the same time, the gap region is replenished with colder fluid from the main subchannel, thereby enhancing heat transfer and avoiding hot spots on the fuel cladding. Future research could, therefore, aim at quantifying the lateral mass transfer between the gap region and the subchannel. For example, several "slices" of fluid could be measured with PIV as the laser is moved farther away from the rod, towards the bulk of the subchannel. A mass balance could thus be applied to the resulting measured volume of total lateral surface S:

$$\frac{dm}{dt} = \int_S \rho \vec{v} \cdot \hat{n} dS.$$

This approach could provide information on the net transfer of fluid between the gap and the subchannel due to the presence of the wire.

An attempt at providing a correlation to predict the bending angle of the flow near the wire has been done in the latter part of Chapter 5. The correlation involves several macroscopic variables such as the dimensions of the bundle (wire and rod diameters, helicoid wire's pitch). Although the influence of the dimensional tolerances of these parameters has been estimated, the correlation should be validated on different wire-wrapped rod bundle geometries, for example by changing the wire-to-rod diameter ratio or the pitch of the helicoid path. This could not be done in this research and it is therefore recommended as future work.

Optical measurements in a 7-rod bundle offer easier optical access and may be cheaper due to lower material costs, compared to larger bundles with 19, 37 or 61 pins. However, due to the reduced size of a 7-rod bundle, material tolerances of the components (i.e. rod and wire diameter, thickness of the hexagonal casing) might have a larger relative influence on the flow area. For example, a deviation from the nominal value of the thickness of the outer hexagonal wall could reduce the flow area in the cross section, affecting the flow and the estimation of the bulk velocity. This aspect is thus to be taken in careful consideration when designing a rod bundle facility.

6.6 Nomenclature

Symbols	Description	Units
D_{h}^{*}	Hydraulic diameter of the gap region	m
$f_{\mathrm{sil,n}}$	Natural frequency of the oscillating silicone rod	Hz
f_{y}	Frequency of coherent structures	Hz
m	Mass of fluid	kg
n, s	Indices pertaining to the normal and tangential coordinate along a streamline	–
P/D	Ratio between the pitch and the diameter of the half rods	–
p	Pressure	Pa
$\vec{r}$	Vector of position	m
S	Lateral surface of the measured volume of fluid	m^2
t	Time	s
u, v	Transversal and vertical velocity component of the flow	$\mathrm{m\,s^{-1}}$

Greek letters	Description	Units
β	Bending angle of the streamline	$^{\circ}$
λ	Wavelength of coherent structures in the stream-wise (vertical) direction	m
ρ	Fluid density	$\mathrm{kg\,m^{-3}}$

Acronyms	Description
FEP	Fluorinated Ethylene Propylene
FIV	Flow-induced vibration
FSI	Fluid-structure interaction
LDA	Laser Doppler Anemometry
PIV	Particle Image Velocimetry
RIM	Refractive index-matching

Non dimensional groups	Description
Re	Reynolds number

Bibliography

[1] IAEA. *Nuclear Technology Review*. Tech. rep. International Atomic Energy Agency, 2018. URL: https://www.iaea.org/publications/reports.

[2] W. Marcum and B. I. Spinrad. "Liquid-metal reactors". In: *Encyclopedia Britannica* (2019). URL: https://www.britannica.com/.

[3] N. Notenboom and P. Boot. *An essay on the colourful scene of Europe's energy*. Tech. rep. PBL Netherlands Environmental Assessment Agency, 2016. URL: https://www.pbl.nl/en/publications/an-essay-on-the-colourful-scene-of-europes-energy-transition.

[4] A. De Carbonnel. "EU's climate chief calls for net-zero emissions by 2050". In: *Reuters* (2018). URL: https://www.reuters.com.

[5] L. V. Finogenov et al. "3D laser inspection of fuel assembly grid spacers for nuclear reactors based on diffractive optical elements". In: *Measurement Science and Technology* **18** (2007). DOI: 10.1088/0957-0233/18/6/S18.

[6] S. Tavoularis. "Rod bundle vortex networks, gap vortex streets, and gap instability: A nomenclature and some comments on available methodologies". In: *Nuclear Engineering and Design* **241** (2011), pp. 2624–2626. DOI: 10.1016/j.nucengdes.2011.03.052.

[7] M. Van Dyke. *An Album of Fluid Motion*. The Parabolic Press, 1982. ISBN: 0-915760-02-9.

[8] L. Meyer. "From discovery to recognition of periodic large scale vortices in rod bundles as source of natural mixing between subchannels-A review". In: *Nuclear Engineering and Design* **240** (2010), pp. 1575–1588. DOI: 10.1016/j.nucengdes.2010.03.014.

[9] F. R. S. Lord Rayleigh. "On the Stability, or Instability, of certain Fluid Motions". In: *London Mathematical Society*. Vol. s1–11. 1879, pp. 57–72. DOI: 10.1112/plms/s1-11.1.57.

[10] D. S. Rowe and B. M. Johnson. "Implications concerning rod bundle cross-flow mixing based on measurements of turbulent flow structure". In: *International Journal of Heat and Mass Transfer* **17** (1974), pp. 407–419. DOI: 10.1016/0017-9310(74)90012-X.

[11] K. Rehme. "The structure of turbulent flow through rod bundles". In: *Nuclear Engineering and Design* **99** (1987), pp. 141–154. DOI: 10.1016/0029-5493(87)90116-6.

[12] S. V. Möller. "On phenomena of turbulent flow through rod bundles". In: *Experimental Thermal and Fluid Science* **4** (1991), pp. 25–35. DOI: 10.1016/0894-1777(91)90018-M.

[13] G. H. Choueiri and S. Tavoularis. "Experimental investigation of flow development and gap vortex street in an eccentric annular channel. Part 1. Overview of the flow structure". In: *Journal of Fluid Mechanics* **752** (2014), pp. 521–542. DOI: 10.1017/jfm.2014.343.

[14] A. Gosset and S. Tavoularis. "Laminar flow instability in a rectangular channel with a cylindrical core". In: *Physics of Fluids* **18** (2006). DOI: 10.1063/1.2194968.

[15] E. Piot and S. Tavoularis. "Gap instability of laminar flows in eccentric annular channels". In: *Nuclear Engineering and Design* **241** (2011), pp. 4615–4620. DOI: 10.1016/j.nucengdes.2010.08.025.

[16] F. Baratto, S. C. C. Bailey, and S. Tavoularis. "Measurements of frequencies and spatial correlations of coherent structures in rod bundle flows". In: *Nuclear Engineering and Design* **236** (2006), pp. 1830–1837. DOI: 10.1016/j.nucengdes.2005.12.009.

[17] A. Mahmood. "Single-Phase Crossflow Mixing in a Vertical Tube Bundle Geometry - An Experimental Study". PhD thesis. Delft University of Technology, June 2011.

[18] L. Meyer and K. Rehme. "Large-scale turbulence phenomena in compound rectangular channels". In: *Experimental Thermal and Fluid Science* **8** (1994), pp. 286–304. DOI: 10.1016/0894-1777(94)90059-0.

[19] M. S. Guellouz and S. Tavoularis. "The structure of turbulent flow in a rectangular channel containing a cylindrical rod - Part 1: Reynolds-averaged measurements". In: *Experimental Thermal and Fluid Science* **23** (2000), pp. 59–73. DOI: 10.1016/S0894-1777(00)00039-X.

[20] G. H. Choueiri and S. Tavoularis. "Experimental investigation of flow development and gap vortex street in an eccentric annular channel. Part 2. Effects of inlet conditions, diameter ratio, eccentricity and Reynolds number". In: *Journal of Fluid Mechanics* **768** (2015), pp. 294–315. DOI: 10.1017/jfm.2015.90.

[21] D. Chang and S. Tavoularis. "Unsteady Numerical Simulations of Turbulence and Coherent Structures in Axial Flow Near a Narrow Gap". In: *Journal of Fluids Engineering* **127** (2005), p. 458. DOI: 10.1115/1.1900140.

[22] E. Merzari and H. Ninokata. "Proper orthogonal decomposition of the flow in a tight lattice rod-bundle". In: *Nuclear Engineering and Design* **241** (2011), pp. 4621–4632. DOI: 10.1016/j.nucengdes.2010.12.005.

[23] Naudascher E. and Rockwell D. “Oscillator-model approach to the identification and assessment of flow-induced vibrations in a system”. In: *Journal of Hydraulic Research* **18** (1980), pp. 59–82.

[24] M. P. Païdoussis. *Fluid-Structure Interaction: Slender Structures and Axial Flow*. Vol. 1. Academic Press, 2014. ISBN: 978-0-12-397312-2.

[25] J. De Ridder et al. “Simulating the fluid forces and fluid-elastic instabilities of a clamped-clamped cylinder in turbulent axial flow”. In: *Journal of Fluid and Structures* **55** (2015), pp. 139–154. DOI: 10.1016/j.jfluidstructs.2015.03.001.

[26] M. P. Païdoussis. “The dynamical behaviour of cylindrical structures in axial flow”. In: *Annals of Nuclear Science and Engineering* **1** (1974), pp. 83–106. DOI: 10.1016/0302-2927(74)90055-5.

[27] M. P. Païdoussis. “Dynamics of flexible slender cylinders in axial flow Part 1. Theory”. In: *Journal of Fluid Mechanics* **26** (1966), pp. 717–736. DOI: 10.1017/S0022112066001484.

[28] M. P. Païdoussis. *Fluid-Structure Interactions: Slender Structures and Axial Flow*. Vol. 2. Elsevier, 2016. ISBN: 978-0-12-397333-7.

[29] University of Washington Libraries. *History of the The Tacoma Narrows Bridge*. URL: https://www.lib.washington.edu/specialcollections/collections/exhibits.

[30] A. Jenkins. “Self-oscillation”. In: *Physics Reports* **525** (2013), pp. 167–222. DOI: 10.1016/j.physrep.2012.10.007.

[31] A. Moorthi, A. K. Sharma, and K. Velusamy. “A review of sub-channel thermal hydraulic codes for nuclear reactor core and future directions”. In: *Nuclear Engineering and Design* **332** (2018), pp. 329–344. DOI: 10.1016/j.nucengdes.2018.03.012.

[32] H. Sato et al. “Study on Velocity Field in a Wire Wrapped Fuel Pin Bundle of Sodium Cooled Reactor-Detailed Velocity Distribution in a Subchannel”. In: *Proc. 13th International Topical Meeting on Nuclear Reactor Thermal Hydraulics (NURETH-13)*. Kanazawa City, Japan, 2009.

[33] N. Goth et al. “Comparison of experimental and simulation results on interior subchannels of a 61-pin wire-wrapped hexagonal fuel bundle”. In: *Nuclear Engineering and Design* **338** (2018), pp. 130–136. DOI: 10.1016/j.nucengdes.2018.08.002.

[34] T. Nguyen and Y. Hassan. “Stereoscopic particle image velocimetry measurements of flow in a rod bundle with a spacer grid and mixing vanes at a low Reynolds number”. In: *International Journal of Heat and Fluid Flow* **67** (2017), pp. 202–219. DOI: 10.1016/j.ijheatfluidflow.2017.08.011.

[35] T. Nguyen et al. “PIV measurements of turbulent flows in a 61-pin wire-wrapped hexagonal fuel bundle”. In: *International Journal of Heat and Fluid Flow* **65** (2017), pp. 47–59. DOI: 10.1016/j.ijheatfluidflow.2017.03.007.

[36] A. Shams et al. “High fidelity numerical simulations of an in fi nite wire-wrapped fuel assembly”. In: *Nuclear Engineering and Design* **335** (2018), pp. 441–459. DOI: 10.1016/j.nucengdes.2018.06.012.

[37] P. Fischer, J. Lottes, and A. Siegel. “Large Eddy Simulation of wire-wrapped fuel pins I: hydrodynamics of a single pin”. In: *Proc. Joint Int. Topical Meeting on Mathematics & Computation and Supercomputing in Nuclear Applications (M&C + SNA 2007*. Monterey, CA USA, 2007.

[38] W. D. Pointer, P. Fischer, and A. Siegel. “RANS-based CFD Simulations of Wire-Wrapped Fast Reactor Fuel Assemblies”. In: *Proc. ICAPP ’08*. Anaheim, CA (USA), 2008.

[39] E. Merzari et al. “Benchmark exercise for fluid flow simulations in a liquid metal fast reactor fuel assembly”. In: *Nuclear Engineering and Design* **298** (2016), pp. 218–228. DOI: 10.1016/j.nucengdes.2015.11.002.

[40] A. V. Obabko, E. Merzari, and P. Fischer. “Nek5000 large eddy simulations for thermal-hydraulics of deformed wire-wrap fuel assemblies”. In: *Transactions of the American Nuclear Society (ANS 2016)*. Las Vegas, USA, 2016.

[41] L. Brockmeyer et al. “Numerical simulations for determination of minimum representative bundle size in wire wrapped tube bundles”. In: *Nuclear Engineering and Design* **322** (2017), pp. 577–590. DOI: 10.1016/j.nucengdes.2017.06.038.

[42] A. Shams, F. Roelofs, and E. M. J. Komen. “High-fidelity numerical simulation of the flow through an infinite wire-wrapped fuel assembly”. In: *Proc. 16th International Topical Meeting on Nuclear Reactor Thermal Hydraulics (NURETH 16)*. Chicago, IL (USA), 2015.

[43] D. Dovizio, A. Shams, and F. Roelofs. “Numerical prediction of flow and heat transfer in an infinite wire-wrapped fuel assembly”. In: *Nuclear Engineering and Design* **349** (2019). DOI: 10.1016/j.nucengdes.2019.04.041.

[44] T. Ohtake, S. Uruwashi, and K. Takahashi. “Velocity Measurements in the Subchannel of the Wire-Spaced Subassembly”. In: *Nuclear Technology* **30** (1976), pp. 333–349. DOI: 10.13182/NT76-A31648.

[45] Song, M. S. and Jeong, J. H. and Kim, E. S. “Numerical investigation on vortex behavior in wire-wrapped fuel assembly for a sodium fast reactor”. In: *Nuclear Engineering and Technology* **51** (2019), pp. 665–675. DOI: 10.1016/j.net.2018.12.012.

[46] L. W. Tilton and J. K. Taylor. “Refractive index and dispersion of distilled water for visible radiation, at temperatures 0 to 60 °C”. In: *Journal of Research of the National Bureau of Standards* **20** (1938), pp. 419–477.

[47] F. Roelofs et al. “Towards validated prediction with RANS CFD of flow and heat transport in a wire-wrap fuel assembly”. In: *Proc. SESAME International Workshop*. Petten, The Netherlands, 2019.

[48] A. Sciacchitano and B. Wieneke. “PIV uncertainty propagation”. In: *Measurement Science and Technology* **27** (2016). DOI: 10.1088/0957-0233/27/8/084006.

[49] R. J. Adrian and C. S. Yao. "Power spectra of fluid velocities measured by laser Doppler velocimetry". In: *Experiments in Fluids* **5** (1986), pp. 17–28. DOI: 10.1007/BF00272419.

[50] M. J. Tummers and D. M. Passchier. *Spectral analysis of Individual Realization LDA data*. Tech. rep. Delft University of Technology, Faculty of Aerospace Engineering, Report LR 808, 1996.

[51] H. Nobach. "Processing of stochastic sampled data in laser Doppler anemometry". In: *Proc. 3rd International Workshop on Sampling Theory and Applications*. 1999.

[52] H. Nobach. "Fuzzy time quantization and local normalization for the direct spectral estimation from lase Doppler velocimetry data". In: *Experiments in Fluids* **56** (2015), pp. 1–4. DOI: 10.1007/s00348-015-1975-x.

[53] S. B. Pope. *Turbulent Flows*. Cambridge (UK): Cambridge University Press, 2000. ISBN: 978-0-521-59886-6.

[54] F. T. M. Nieuwstadt, B. J. Boersma, and J. Westerweel. *Turbulence - Introduction to Theory and Applications of Turbulent Flows*. Springer Nature, 2016.

[55] W. T. Mayo. "A Discussion of Limitations and Extensions of Power Spectrum Estimation with Burst Counter LDV Systems". In: *Proc. 2nd International Workshop on Laser Velocimetry*. 1974.

[56] M J Tummers and D M Passchier. "Spectral analysis of biased LDA data". In: *Measurement Science and Technology* **12** (2001), pp. 1641–1650. DOI: 10.1088/0957-0233/12/10/304.

[57] X. Wu and A. C. Trupp. "Spectral measurements and mixing correlation in simulated rod bundle subchannels". In: *International Journal of Heat and Mass Transfer* **37** (1994), pp. 1277–1281. DOI: 10.1016/0017-9310(94)90212-7.

[58] J. Goulart, L. Noleto, and S. V. Möller. "Experimental study of mixing layer in a closed compound channel". In: *Journal of the Brazilian Society of Mechanical Sciences and Engineering* **36** (2014), pp. 411–420. DOI: 10.1007/s40430-013-0081-3.

[59] L. Meyer and K. Rehme. "Periodic Vortices in Flow Through Channels With Longitudinal Slots or Fins". In: *Proc. 10th Symposioum on Turbulent shear flows*. University Park, PA (USA), 1995.

[60] I. Marusic et al. "Wall-bounded turbulent flows at high Reynolds numbers: Recent advances and key issues". In: *Physics of Fluids* **22** (2010), pp. 1–24. DOI: 10.1063/1.3453711.

[61] A. S. Lexmond, R. F. Mudde, and T. H. J. J. Van Der Hagen. "Visualisation of the Vortex Street and Characterisation of the Cross Flow in the Gap Between Two Sub-Channels". In: *Proc. 11th International Topical Meeting on Nuclear Reactor Thermal-Hydraulics*. Avignon, France, 2005.

[62] M. S. Guellouz and S. Tavoularis. "The structure of turbulent flow in a rectangular channel containing a cylindrical rod - Part 2: phase-averaged measurements". In: *Experimental Thermal and Fluid Science* **23** (2000), pp. 75–91. DOI: 10.1016/S0894-1777(00)00039-X.

[63] A. N. Kolmogorov. "A refinement of previous hypotheses concerning the local structure of turbulence". In: *Journal of Fluid Mechanics* **13** (1962), pp. 83–85.

[64] S. Chang, S. Kim, and C. Song. "Turbulent mixing in a rod bundle with vaned spacer grids: OECD/NEA-KAERI CFD benchmark exercise test". In: *Nuclear Engineering and Design* **279** (2014), pp. 19–36. DOI: 10.1016/j.nucengdes.2014.05.013.

[65] R. D. Guenther. *Modern Optics*. John Whiley & Sons, 1990. ISBN: 978-0-47-160538-6.

[66] M. P. Païdoussis. "Fluidelastic vibration of cylinder arrays in axial and cross flow: State of the art". In: *Journal of Sound and Vibration* **76** (1981), pp. 329–360. DOI: 10.1016/0022-460X(81)90516-2.

[67] J. De Ridder et al. "Vortex-induced vibrations by axial flow in a bundle of cylinders". In: *Proc. 11th International Conference on Flow-Induced Vibrations*. The Hague, The Netherlands, 2016, pp. 1–8.

[68] H. Dolfen et al. "Numerical Investigation of Vortex-Induced Vibrations of a Bundle of Cylinders in Axial Flow". In: *Proc. 9th International Symposium on Fluid-Structure Interactions, Flow-Sound Interactions, Flow-Induced Vibration & Noise*. Toronto, Canada, 2018, pp. 1–6.

[69] I. E. Idel'chik. *Handbook of hydraulic resistance*. Begell House, 2007. ISBN: 978-1-56-700251-5.

[70] E. Rathakrishnan. *Fluid Mechanics, An Introduction*. Phi Learning Private Ltd, 2012. ISBN: 978-8-12-034593-5.

[71] E. E. Dominguez-Ontiveros and Y. Hassan. "Non-intrusive experimental investigation of flow behavior inside a 5X5 rod bundle with spacer grids using PIV and MIR". In: *Nuclear Engineering and Design* **239** (2009), pp. 888–898. DOI: 10.1016/j.nucengdes.2009.01.009.

[72] E. E. Dominguez-Ontiveros and Y. A. Hassan. "Experimental study of a simplified 3 × 3 rod bundle using DPTV". In: *Nuclear Engineering and Design* **279** (2014), pp. 50–59. DOI: 10.1016/j.nucengdes.2014.04.037.

[73] M. Rohde et al. "Rod bundle and pool-type experiments in water serving liquid metal reactors". In: *Thermal Hydraulics Aspects of Liquid Metal Cooled Nuclear Reactors*. Ed. by F. Roelofs. Woodhead Publishing Series in Energy, 2019. Chap. 3.1, pp. 49–82. DOI: 10.1016/B978-0-08-101980-1.00011-9.

[74] Y. A. Hassan and E. E. Dominguez-Ontiveros. "Flow visualization in a pebble bed reactor experiment using PIV and refractive index matching techniques". In: *Nuclear Engineering and Design* **238** (2008), pp. 3080–3085. DOI: 10.1016/j.nucengdes.2008.01.027.

[75] S. Hosokawa et al. “Measurements of turbulent flows in a 2X2 rod bundle”. In: *Nuclear Engineering and Design* **249** (2012), pp. 2–13. DOI: 10.1016/j.nucengdes.2011.11.035.

[76] F. Bertocchi, M. Rohde, and J. L. Kloosterman. “LDA measurements of coherent flow structures and cross- flow across the gap of a compound channel with two half-rods”. In: *Nuclear Engineering and Design* **326** (2018), pp. 17–30. DOI: 10.1016/j.nucengdes.2017.10.023.

[77] Y. Modarres-Sadeghi et al. “Experiments on vertical slender flexible cylinders clamped at both ends and subjected to axial flow.” In: *Philosophical Transactions of the Royal Society A: Mathematical, Physical and Engineering Sciences* **336** (2007), pp. 1275–1296. DOI: 10.1098/rsta.2007.2131.

[78] Y. Perets, E. Sher, and R. Harari. “An experimental study on axial-flow-induced vibration of confined flexible rods with sequenced transverse rib roughness”. In: *Experimental Thermal and Fluid Science* **93** (2018), pp. 86–95. DOI: 10.1016/j.expthermflusci.2017.12.026.

[79] Y. M. Chen. “Flow-induced vibrations in tube bundle heat exchangers with cross and parallel flows. Part 1: parallel flow.” In: *Flow-Induced Vibration in Heat Exchangers*. Ed. by D. D. Reiff. ASME, 1970, pp. 57–66.

[80] R. D. Blevins. “Flow-induced vibration in nuclear reactors: a review”. In: *Progress in Nuclear Energy* **4** (1979), pp. 25–49. DOI: 10.1016/0149-1970(79)90008-8.

[81] M. P. Païdoussis, N. T. Issid, and M. Tsui. “Parametric resonance oscillations of flexible slender cylinders in harmonically perturbed axial flow. Part 2: Experiments”. In: *Journal of Applied Mechanics* **47** (1980), pp. 715–719. DOI: 10.1115/1.3153779.

[82] M. J. Pettigrew et al. “Flow-induced vibration: recent findings and open questions”. In: *Nuclear Engineering and Design* **185** (1998), pp. 249–276. DOI: 10.1016/0029-5493(91)90319-D.

[83] S. F. Hoerner. *Fluid-Dynamic Drag*. Bakersfield, CA (US): Hoerner, 1965. ISBN: 978-9-99-119444-8.

[84] V. F. Sinyavskii, V. S. Fedotovskii, and A. B. Kukhtin. “Oscillation of a cylinder in a viscous liquid”. In: *Prikladnaya Mekhanika* **16** (1980), pp. 62–67.

[85] M. J. Pettigrew and C. E. Taylor. “Two-phase flow-induced vibration: An overview”. In: *Journal of Pressure Vessel Technology* **116** (1994), pp. 233–253. DOI: 10.1115/1.2929583.

[86] S. S. Chen. *Flow - Induced Vibration of circular cylindrical structures*. Tech. rep. ANL-85-51. Argonne National Laboratory, 1985.

[87] A. Don and S. Tavoularis. “Measurements of turbulent flow in a large-scale model of a 37-rod bundle”. In: *Nuclear Engineering and Design* **337** (2018), pp. 116–127. DOI: 10.1016/j.nucengdes.2018.06.018.

[88] E. Buckingham. "On physically similar systems; illustrations on the use of dimensional equations". In: *Physical Review* **4** (1914), pp. 345–376. DOI: 10.1103/PhysRev.4.345.

[89] N. E. Todreas and M. S. Kazimi. *Nuclear System*. Vol. 1. CRC Press, 1990. ISBN: 1-56032-051-6.

[90] N. Otsu. "A threshold selection method from gray-level histograms". In: *IEEE transactions on Systems, Man and Cybernetics* **9** (1979), pp. 62–66. DOI: 10.1109/TSMC.1979.4310076.

[91] A. Cioncolini et al. "Axial-flow-induced vibration experiments on cantilever rods fo nuclear reactor applications". In: *Nuclear Engineering and Design* **338** (2018), pp. 102–118. DOI: 10.1016/j.nucengdes.2018.08.010.

[92] H. H. Monson. *Statistical Digital Signal Processing and Modeling*. John Wiley & Sons, 1996. ISBN: 978-8-12-651610-0.

[93] F. M. White. *Fluid Mechanics*. Mc Graw Hill, 2016. ISBN: 978-9-38-596549-4.

[94] S. K. Chen, Y. M. Chen, and N. M. Todreas. "The upgraded Cheng and Todreas correlation for pressure drop in hexagonal wire-wrapped rod bundles". In: *Nuclear Engineering and Design* **335** (2018), pp. 356–373. DOI: 10.1016/j.nucengdes.2018.05.010.

[95] G. K. Batchelor. "Computation of the Energy Spectrum in Homogeneous Two-Dimensional Turbulence". In: *Physics of Fluids* **12** (1969), pp. 233–239. DOI: 10.1063/1.1692443.

[96] R. H. Kraichnan. "Inertial Ranges in Two-Dimensional Turbulence". In: *Physics of Fluids* **10** (1967), pp. 1417–1423. DOI: 10.1063/1.1762301.

[97] G. P. Romano. "Analysis of two-point velocity measurements in near-wall flows". In: *Experiments in Fluids* **20** (1995), pp. 68–83. DOI: 10.1007/BF00189296.

[98] C. H. K. Williamson and R. Govardhan. "Vortex-Induced Vibrations". In: *Annual Review of Fluid Mechanics* **36** (2004), pp. 413–455. DOI: 10.1146/annurev.fluid.36.050802.122128.

[99] J. Guidez and G. Prêle. *SuperPhenix Technical and Scientific Achievements*. Atlantis Press, 2017. ISBN: 978-94-6239-245-8.

[100] P. Baeten et al. "MYRRHA: A multipurpose research facility". In: *EPJ Web of Conferences* **79** (2014). DOI: 10.1051/epjconf/20147903001.

[101] C. Tropea, A. L. Yarin, and J. L. Foss. *Springer Handbook of Experimental Fluid Mechanics*. Springer, 2007. ISBN: 978-3-54-030299-5.

[102] J. Westerweel. "Efficient detection of spurious vectors in particle image velocimetry data". In: *Experiments in Fluids* **247** (1994), pp. 236–247. DOI: 10.1007/BF00206543.

[103] T. Nguyen et al. “Stereoscopic PIV measurements of near-wall flow in a tightly packed rod bundle with wire spacers”. In: *International Journal of Heat and Fluid Flow* 92 (2018), pp. 420–435. DOI: 10.1016/j.expthermflusci.2017.11.009.

[104] R. de Kat and B. W. van Oudheusden. “Instantaneous planar pressure from PIV: analytic and experimental test-cases”. In: *Proc. 15th Int. Symposium on Applications of Laser Techniques to Fluid Mechanics*. Lisbon, Portugal, 2010.

[105] R. De Kat and B. W. Van Oudheusden. “Instantaneous planar pressure determination from PIV in turbulent flow”. In: *Experiments in Fluids* **52** (2011), pp. 1089–1106. DOI: 10.1007/s0034801112375.

[106] V. A. Zorich. *Mathematical analysis I*. Springer, 2004. ISBN: 978-3-54-040386-9.

[107] J. A. Fay. *Introduction to Fluid Mechanics*. MIT Press, 1994. ISBN: 978-0-26-206165-0.

[108] R. W. Fox et al. *Fox and McDonald’s Introduction to Fluid Mechanics*. Wiley, 2011. ISBN: 978-0-47-054755-7.

[109] G. Biswas, M. Breuer, and F. Durst. “Backward-Facing Step Flows for Various Expansion Ratios at Low and Moderate Reynolds Numbers”. In: *Journal of Fluids Engineering* **126** (2004), pp. 362–374. DOI: 10.1115/1.1760532.

[110] P. W. Bearman and M. M. Zdravkovich. “Flow around a circular cylinder around a plane boundary”. In: *Journal of Fluid Mechanics* **89** (1978), pp. 33–47. DOI: 10.1017/S002211207800244X.

[111] M. Hartig, T. Schulenberg, and A. Batta. “Numerical Study of Fluid-Structure Interaction with Heat Transfer at Supercritical Pressure in a Fuel Rod Assembly”. In: *ASME Journal of Nuclear Engineering and Radiation Science* **2** (2015). DOI: 10.1115/1.4031816.

[112] J. Heinecke and G. Weber. “Thermoelastic Instabilities of Fast Reactor Fuel Pins”. In: *Proc. 5th International Conference on Flow Induced Vibrations*. Brighton (UK), 1991.

[113] D. W. van Krevelen and K. te Nijenhuis. *Properties of Polymers*. Elsevier, 2009. ISBN: 978-0-08-054819-7.

[114] J. O’M. Bockris and A. K. N. Reddy. *Modern Electrochemistry-Ionics*. Vol. 1. Kluwer Academic Publishers, 2002. ISBN: 0-306-45554-4.

Appendix A

This appendix shows the derivation of Equation 2.26 used in chapter 2 to estimate the refraction of the laser beam through the FEP layer. Referring to Figure A.1

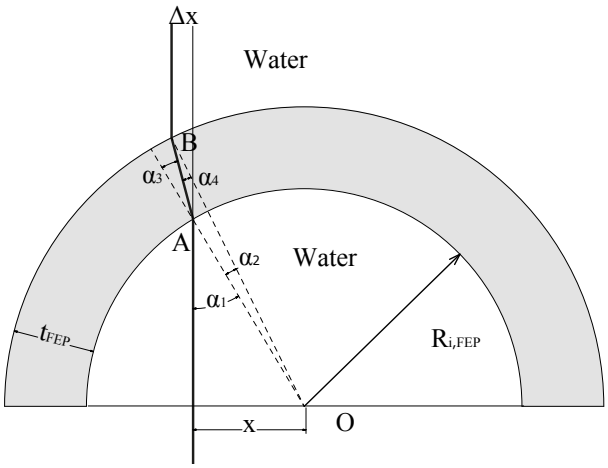

Figure A.1: Refraction of the laser beam as it crosses the FEP half-rod. The horizontal refraction Δx due to the curvature of the FEP wall is retrieved from geometrical considerations.

$$\sin\alpha_1 = \frac{x}{\mathrm{R}_{i,\mathrm{FEP}}}; \qquad \sin\alpha_3 = \sin\alpha_1 \frac{\eta}{\eta_{\mathrm{FEP}}}, \tag{A.1}$$

where α_3 is the angle of the refracted light ray through the FEP, η and η_{FEP} are air and FEP's indices of refraction. $\alpha_3$is obtained as

$$\alpha_3 = \arcsin\left(\frac{x\eta}{\eta_{\mathrm{FEP}}\mathrm{R}_{i,\mathrm{FEP}}}\right). \tag{A.2}$$

Considering the triangle $\overset{\triangle}{\mathrm{AOB}}$, the law of sine is applied twice:

$$\frac{\overline{AB}}{\sin\alpha_2}=\frac{R_{i,FEP}}{\sin\alpha_4};\qquad \frac{\overline{AB}}{\sin\alpha_2}=\frac{R_{i,FEP}+t_{FEP}}{\sin(\pi-\alpha_3)}. \tag{A.3}$$

Hence,

$$\sin\alpha_4=\sin\alpha_3\frac{R_{i,FEP}}{R_{i,FEP}+t_{FEP}}=\frac{x\eta}{\eta_{FEP}(R_{i,FEP}+t_{FEP})}, \tag{A.4}$$

from which α_4 is obtained as

$$\alpha_4=\arcsin\left[\frac{x\eta}{\eta_{FEP}(R_{i,FEP}+t_{FEP})}\right]. \tag{A.5}$$

The inner angles of the triangle $\overset{\triangle}{AOB}$ sum up to π:

$$\alpha_2+(\pi-\alpha_3)+\alpha_4=\pi, \tag{A.6}$$

meaning that the value of α_2 is estimated as

$$\alpha_2=\pi-(\pi-\alpha_3)-\alpha_4, \tag{A.7}$$

where α_3 and α_4 are given by Equations A.2 and A.5.

$\overline{AB}$ is obtained by applying the law of cosine to the triangle $\overset{\triangle}{AOB}$:

$$\begin{aligned}\overline{AB}^2 &= R_{i,FEP}{}^2+(R_{i,FEP}+t_{FEP})^2+\\ &\quad -2R_{i,FEP}(R_{i,FEP}+t_{FEP})\cos\alpha_2.\end{aligned} \tag{A.8}$$

Finally, the distortion due to the presence of FEP is given by

$$\Delta x=\overline{AB}\sin(\alpha_1-\alpha_3). \tag{A.9}$$

Appendix B

The refractive index matching technique (RIM) can be applied either by employing materials whose refractive index is close to the working fluid's (S2F method, for conciseness), or by adjusting the refractive index of the fluid to the one of the material forming the experimental setup (F2S method, for conciseness) [73]. The experimental facilities described in this thesis adopt the S2F method (see section 3.2.3) because the F2S option has proven unfeasible in the current experiments. This appendix explains why the F2S method has not been followed. A possible implementation of the F2S RIM technique would consist of components (rods, casing) made of Perspex (η_{PMMA}=1.49) while the working fluid would be a solution of water and salt to adjust the refractive index to the Perspex's. The refractive index of such a solution, η_{sol}, can be estimated through the Looyenga or the Lorentz-Lorenz formulas [113], respectively

$$\left(\eta_{\mathrm{sol}}^{2/3}-1\right)\phi_{\mathrm{sol}}=\sum\phi_i\left(\eta_i^{2/3}-1\right) \tag{B.1}$$

and

$$\left(\frac{\eta_{\mathrm{sol}}^2-1}{\eta_{\mathrm{sol}}^2+2}\right)\phi_{\mathrm{sol}}=\sum\phi_i\left(\frac{\eta_i^2-1}{\eta_i^2+2}\right), \tag{B.2}$$

where η_{sol} is the refractive index of the solution to be determined, ϕ_{sol} is the molar volume of the solution, and ϕ_i and η_i are the molar volume and the refractive index of the individual compounds (i.e. water and salt). The refractive index of a solution of NaCl and water is measured with an Abbe refractometer to test the accuracy of Equation B.1 and B.2: the results are shown in Figure B.1.

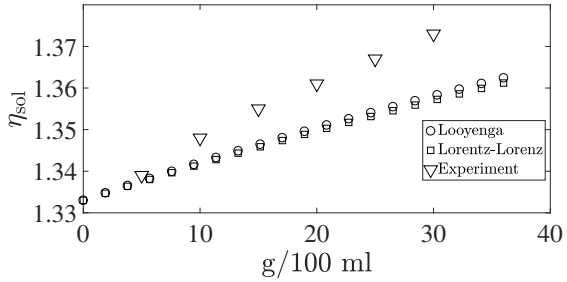

Figure B.1: Refractive index as a function of the concentration of NaCl dissolved in water predicted by the theory and measured experimentally.

The Looyenga and Lorentz-Lorenz equations underpredict the experimental refractive index of the solution and the discrepancy grows larger as more salt is added to the solution. A possible explanation is that the two equations do not take into account the volume change between the crystal and ionic (dissolved) form of the salt, which is to be determined empirically [114]. If the components of the rod bundle would be made of Perspex, the acqueous solution should reach a refractive index of η_{PMMA}=1.49. The considered salts are CsI, CsCl, KI and KSCN. The refractive index of the acqueous solution is estimated with Equation B.1 and B.2, and shown in Figure B.2a and B.2b, respectively. Although Figure B.2 shows that

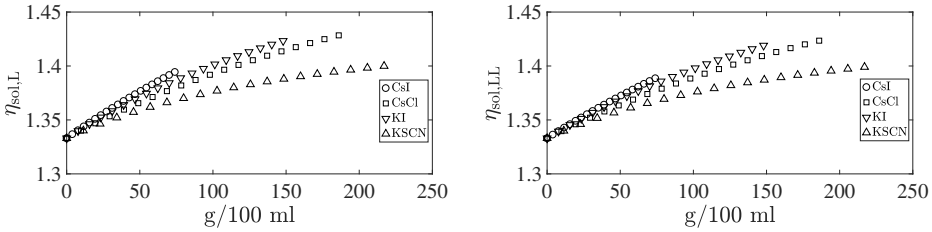

(a) **(b)**

Figure B.2: Refractive index of an acqueous solution as a function of the amount of dissolved salt, evaluated through the Looyenga equation a) and Lorentz-Lorenz equation b). The refractive index that needs to be matched is η_{PMMA}=1.49. The series are plotted throughout the solubility range of the considered salt.

CsI and KI are the best candidates to match the Perspex's refractive index, the required amount of salt exceeds their solubility limit. Furthermore, a salty solution would corrode the metal parts of the experimental lopp such as the pump, hence the F2S RIM technique is discarded and the S2F strategy is followed instead.

Appendix C

Considering a control volume immersed in a fluid in steady state (Figure C.1), and neglecting gravity and frictions, a momentum balance can be set up. In an

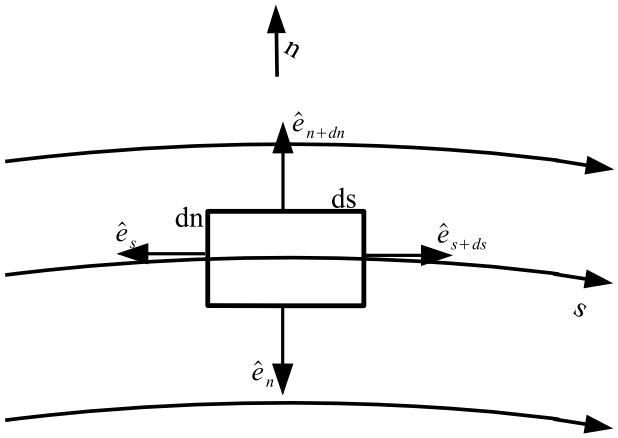

Figure C.1: Control volume in a Eulerian reference frame.

Eulerian frame of reference, along the s direction, this is

$$\rho U_{\mathrm{s}} \cdot U_{\mathrm{s}} \mathrm{dn} \hat{e}_{\mathrm{s}} + \rho U_{\mathrm{s+ds}} \cdot U_{\mathrm{s+ds}} \mathrm{dn} \hat{e}_{\mathrm{s+ds}} + \rho U_{\mathrm{n}} \cdot U_{\mathrm{s}} \mathrm{dn} \hat{e}_{\mathrm{s}} + \rho U_{\mathrm{n}} \cdot U_{\mathrm{s+ds}} \mathrm{dn} \hat{e}_{\mathrm{s+ds}} + \\ + p_{\mathrm{s}} \mathrm{dn} \hat{e}_{\mathrm{s}} + p_{\mathrm{s+ds}} \mathrm{dn} \hat{e}_{\mathrm{s+ds}} = 0, \quad \text{(C.1)}$$

Considering that $\hat{e}_{\mathrm{s}} = -\hat{e}_{\mathrm{s+ds}}$, the previous equation becomes

$$\rho U_{\mathrm{s}} \cdot U_{\mathrm{s}} \mathrm{dn} \hat{e}_{\mathrm{s}} - \rho U_{\mathrm{s+ds}} \cdot U_{\mathrm{s+ds}} \mathrm{dn} \hat{e}_{\mathrm{s}} + \rho U_{\mathrm{n}} \cdot U_{\mathrm{s}} \mathrm{dn} \hat{e}_{\mathrm{s}} - \rho U_{\mathrm{n}} \cdot U_{\mathrm{s+ds}} \mathrm{dn} \hat{e}_{\mathrm{s}} + \\ + p_{\mathrm{s}} \mathrm{dn} \hat{e}_{\mathrm{s}} - p_{\mathrm{s+ds}} \mathrm{dn} \hat{e}_{\mathrm{s}} = 0, \quad \text{(C.2)}$$

from which it follows

$$-\frac{\partial(\rho U_{\mathrm{s}}\cdot U_{\mathrm{s}})}{\partial s}\mathrm{dsdn}\hat{e}_{\mathrm{s}}-\frac{\partial(\rho U_{\mathrm{n}}\cdot U_{\mathrm{s}})}{\partial s}\mathrm{dsdn}\hat{e}_{\mathrm{s}}-\frac{\partial p_{\mathrm{s}}}{\partial s}\mathrm{dsdn}\hat{e}_{\mathrm{s}}=0. \tag{C.3}$$

If density is constant, it can be moved out of the derivatives:

$$-2\rho U_{\mathrm{s}}\frac{\partial U_{\mathrm{s}}}{\partial s}\hat{e}_{\mathrm{s}}-\rho U_{\mathrm{s}}\frac{\partial U_{\mathrm{n}}}{\partial s}\hat{e}_{\mathrm{s}}-\rho U_{\mathrm{n}}\frac{\partial U_{\mathrm{s}}}{\partial s}\hat{e}_{\mathrm{s}}-\frac{\partial p_{\mathrm{s}}}{\partial s}\hat{e}_{\mathrm{s}}=0. \tag{C.4}$$

The momentum balance along the n direction is

$$\rho U_{\mathrm{s}}\cdot U_{\mathrm{n}}\mathrm{ds}\hat{e}_{\mathrm{n}}+\rho U_{\mathrm{s}}\cdot U_{\mathrm{n+dn}}\mathrm{ds}\hat{e}_{\mathrm{n}}+\rho+U_{\mathrm{n}}U_{\mathrm{n}}\mathrm{ds}\hat{e}_{\mathrm{n}}+\rho U_{\mathrm{n}}U_{\mathrm{n+dn}}\mathrm{ds}\hat{e}_{\mathrm{n+dn}}+ \\ +p_{\mathrm{n}}\mathrm{ds}\hat{e}_{\mathrm{n}}+p_{\mathrm{n+dn}}\mathrm{ds}\hat{e}_{\mathrm{n+dn}}+\rho\mathrm{dnds}\frac{U_{\mathrm{s}}^2}{R}\hat{e}_{\mathrm{n}}=0, \tag{C.5}$$

Considering that $\hat{e}_{\mathrm{n}}=-\hat{e}_{\mathrm{n+dn}}$, the previous equation becomes

$$\rho U_{\mathrm{s}}\cdot U_{\mathrm{n}}\mathrm{ds}\hat{e}_{\mathrm{n}}-\rho U_{\mathrm{s}}\cdot U_{\mathrm{n+dn}}\mathrm{ds}\hat{e}_{\mathrm{n}}+\rho U_{\mathrm{n}}U_{\mathrm{n}}\mathrm{ds}\hat{e}_{\mathrm{n}}-\rho U_{\mathrm{n}}U_{\mathrm{n+dn}}\mathrm{ds}\hat{e}_{\mathrm{n}}+ \\ +p_{\mathrm{n}}\mathrm{ds}\hat{e}_{\mathrm{n}}-p_{\mathrm{n+dn}}\mathrm{ds}\hat{e}_{\mathrm{n}}+\rho\mathrm{dnds}\frac{U_{\mathrm{s}}^2}{R}\hat{e}_{\mathrm{n}}=0, \tag{C.6}$$

$$-\frac{\partial(\rho U_{\mathrm{s}}\cdot U_{\mathrm{n}})}{\partial n}\mathrm{dsdn}\hat{e}_{\mathrm{n}}-\frac{\partial(\rho U_{\mathrm{n}}\cdot U_{\mathrm{n}})}{\partial n}\mathrm{dsdn}\hat{e}_{\mathrm{n}}-\frac{\partial p_{\mathrm{n}}}{\partial n}\mathrm{dsdn}\hat{e}_{\mathrm{n}}+\rho\mathrm{dnds}\frac{U_{\mathrm{s}}^2}{R}\hat{e}_{\mathrm{n}}=0, \tag{C.7}$$

$$-\rho U_{\mathrm{s}}\frac{\partial U_{\mathrm{n}}}{\partial n}\hat{e}_{\mathrm{n}}-\rho U_{\mathrm{n}}\frac{\partial U_{\mathrm{s}}}{\partial n}\hat{e}_{\mathrm{n}}-\frac{\partial(\rho U_{\mathrm{n}}\cdot U_{\mathrm{n}})}{\partial n}\hat{e}_{\mathrm{n}}-\frac{\partial p_{\mathrm{n}}}{\partial n}\hat{e}_{\mathrm{n}}+\rho\frac{U_{\mathrm{s}}^2}{R}\hat{e}_{\mathrm{n}}=0. \tag{C.8}$$

Recalling the continuity equation, and assuming constant fluid density, it follows that

$$\frac{\partial U_{\mathrm{n}}}{\partial n}\hat{e}_{\mathrm{n}}=-\frac{\partial U_{\mathrm{s}}}{\partial s}\hat{e}_{\mathrm{s}}. \tag{C.9}$$

Substituting the previous equation in Equation C.8 we obtain

$$\rho U_{\mathrm{s}}\frac{\partial U_{\mathrm{s}}}{\partial s}\hat{e}_{\mathrm{s}}-\rho U_{\mathrm{n}}\frac{\partial U_{\mathrm{s}}}{\partial n}\hat{e}_{\mathrm{n}}-\rho\frac{\partial(U_{\mathrm{n}}\cdot U_{\mathrm{n}})}{\partial n}\hat{e}_{\mathrm{n}}-\frac{\partial p_{\mathrm{n}}}{\partial n}\hat{e}_{\mathrm{n}}+\rho\frac{U_{\mathrm{s}}^2}{R}\hat{e}_{\mathrm{n}}=0. \tag{C.10}$$

Combining Equation C.10 and Equation C.4 together leads to

$$-2\rho U_{\mathrm{s}}\frac{\partial U_{\mathrm{s}}}{\partial s}\hat{e}_{\mathrm{s}}-\rho U_{\mathrm{s}}\frac{\partial U_{\mathrm{n}}}{\partial s}\hat{e}_{\mathrm{s}}-\rho U_{\mathrm{n}}\frac{\partial U_{\mathrm{s}}}{\partial s}\hat{e}_{\mathrm{s}}-\frac{\partial p_{\mathrm{s}}}{\partial s}\hat{e}_{\mathrm{s}}+\rho U_{\mathrm{s}}\frac{\partial U_{\mathrm{s}}}{\partial s}\hat{e}_{\mathrm{s}}+ \\ -\rho U_{\mathrm{n}}\frac{\partial U_{\mathrm{s}}}{\partial n}\hat{e}_{\mathrm{n}}-\rho\frac{\partial(U_{\mathrm{n}}\cdot U_{\mathrm{n}})}{\partial n}\hat{e}_{\mathrm{n}}-\frac{\partial p_{\mathrm{n}}}{\partial n}\hat{e}_{\mathrm{n}}+\rho\frac{U_{\mathrm{s}}^2}{R}\hat{e}_{\mathrm{n}}=0, \tag{C.11}$$

and then

$$-\rho U_{\mathrm{s}}\frac{\partial U_{\mathrm{s}}}{\partial s}\hat{e}_{\mathrm{s}}-\rho U_{\mathrm{s}}\frac{\partial U_{\mathrm{n}}}{\partial s}\hat{e}_{\mathrm{s}}-\rho U_{\mathrm{n}}\frac{\partial U_{\mathrm{s}}}{\partial s}\hat{e}_{\mathrm{s}}-\frac{\partial p_{\mathrm{s}}}{\partial s}\hat{e}_{\mathrm{s}}-\rho U_{\mathrm{n}}\frac{\partial U_{\mathrm{s}}}{\partial n}\hat{e}_{\mathrm{n}}+$$
$$-\rho\frac{\partial\left(U_{\mathrm{n}}\cdot U_{\mathrm{n}}\right)}{\partial n}\hat{e}_{\mathrm{n}}-\frac{\partial p_{\mathrm{n}}}{\partial n}\hat{e}_{\mathrm{n}}+\rho\frac{U_{\mathrm{s}}^2}{R}\hat{e}_{\mathrm{n}}=0. \quad \text{(C.12)}$$

Recalling the definition of streamline, the velocity vector $\vec{v}\equiv U_{\mathrm{s}}\hat{e}_{\mathrm{s}}$ is tangent to the s direction, meaning $U_{\mathrm{n}}=0$, so the previous equation is re-written as

$$-\rho U\frac{\partial U_{\mathrm{s}}}{\partial s}\hat{e}_{\mathrm{s}}-\frac{\partial p}{\partial s}\hat{e}_{\mathrm{s}}-\frac{\partial p}{\partial n}\hat{e}_{\mathrm{n}}+\rho\frac{U_{\mathrm{s}}^2}{R}\hat{e}_{\mathrm{n}}=0, \quad \text{(C.13)}$$

which is expressed in its compact form

$$-U_{\mathrm{s}}\frac{\partial U_{\mathrm{s}}}{\partial s}\hat{e}_{\mathrm{s}}-\frac{1}{\rho}\nabla p+\frac{U_{\mathrm{s}}^2}{R}\hat{e}_{\mathrm{n}}=0, \quad \text{(C.14)}$$

with $\nabla\equiv\left(\frac{\partial p}{\partial s}\hat{e}_{\mathrm{s}};\frac{\partial p}{\partial n}\hat{e}_{\mathrm{n}}\right)$. Equation C.14 is the same as Equation 5.25 derived with a Lagrangian approach.

Appendix D

The equation

$$\int_{-\infty}^{\sigma} \left[1+\tan^2\beta(\vec{r})\right]^{1/2} \frac{d\beta(\vec{r})}{dy} dy = \int_{-\infty}^{\sigma} \frac{1}{\rho v^2(\vec{r})} \frac{\partial p(\vec{r})}{\partial n} dy, \tag{D.1}$$

treated in Chapter 5 is solved by means of the following substitution:

$$\kappa = \beta(\vec{r})$$
$$d\kappa = \frac{d\beta(\vec{r})}{dy} dy$$

and assuming that the streamline far upstream of the wire is straight, that is $\beta(y=-\infty)=0$. The left-hand side term becomes

$$\int_{0}^{\beta(y=\sigma)} \left[1+\tan^2\kappa\right]^{1/2} d\kappa = \int_{0}^{\beta(y=\sigma)} \left[1+\tan^2\beta(\vec{r})\right]^{1/2} d\beta(\vec{r}). \tag{D.2}$$

Considering that

$$1+\tan^2\beta(\vec{r}) = \frac{1}{\cos^2\beta(\vec{r})}, \tag{D.3}$$

it follows that

$$\int_{0}^{\beta(y=\sigma)} \left[1+\tan^2\beta(\vec{r})\right]^{1/2} d\beta(\vec{r}) = \int_{0}^{\beta(y=\sigma)} \frac{d\beta(\vec{r})}{\cos\beta(\vec{r})}. \tag{D.4}$$

The integral is now re-written as

$$\int_{0}^{\beta(y=\sigma)} \frac{d\beta(\vec{r})}{\cos\beta(\vec{r})} \frac{\cos\beta(\vec{r})}{\cos\beta(\vec{r})} = \int_{0}^{\beta(y=\sigma)} \frac{\cos\beta(\vec{r}) d\beta(\vec{r})}{\cos^2\beta(\vec{r})} = \int_{0}^{\beta(y=\sigma)} \frac{\cos\beta(\vec{r}) d\beta(\vec{r})}{1-\sin^2\beta(\vec{r})}. \tag{D.5}$$

Then the following substitution is operated:

$$q = \sin\beta(\vec{r})$$
$$dq = \cos\beta(\vec{r}) d\beta(\vec{r})$$

such that

$$\int_0^{\beta(y=\sigma)} \frac{\cos\beta(\vec{r}) d\beta(\vec{r})}{1-\sin^2\beta(\vec{r})} = \int_0^{\sin\beta(y=\sigma)} \frac{1}{1-q^2} dq. \tag{D.6}$$

The integrand of the left-hand side term is rearranged as follows:

$$\frac{1}{1-q^2} = \frac{1}{(1+q)(1-q)} = \frac{\mathscr{A}}{1+q} + \frac{\mathscr{B}}{1-q}, \tag{D.7}$$

where $\mathscr{A} = \mathscr{B} = 1/2$.
Therefore,

$$\int_0^{\sin\beta(y=\sigma)} \frac{1}{1-q^2} dq = \frac{1}{2} \int_0^{\sin\beta(y=\sigma)} \frac{1}{1+q} + \frac{1}{2} \int_0^{\sin\beta(y=\sigma)} \frac{1}{1-q} =$$
$$= \frac{1}{2} \left[\ln(1+q) - \ln(1-q)\right]_0^{\sin\beta(y=\sigma)}. \tag{D.8}$$

Equation D.1 becomes

$$\frac{1}{2} \left[\ln(1+\sin\beta(y=\sigma)) - \ln(1-\sin\beta(y=\sigma))\right] = \int_{-\infty}^{\sigma} \frac{1}{\rho v^2(\vec{r})} \frac{\partial p(\vec{r})}{\partial n} dy. \tag{D.9}$$

For small $\beta(\vec{r})$,

$$\sin\beta(\vec{r}) \approx \beta(\vec{r}), \tag{D.10}$$

so

$$\ln(1+\sin\beta(y=\sigma)) \approx \beta(y=\sigma), \tag{D.11}$$

and

$$\ln(1-\sin\beta(y=\sigma)) \approx -\beta(y=\sigma), \tag{D.12}$$

For the left-hand side of Equation D.9, it follows that

$$\frac{1}{2} \left[\ln(1+\sin\beta(y=\sigma)) - \ln(1-\sin\beta(y=\sigma))\right] \approx$$
$$\approx \frac{1}{2} \left[\beta(y=\sigma) - (-\beta(y=\sigma))\right] \approx \beta(y=\sigma). \tag{D.13}$$

For small angles, β is, thus, expressed as

$$\beta(y=\sigma) = \int_{-\infty}^{\sigma} \frac{1}{\rho v^2(\vec{r})} \frac{\partial p(\vec{r})}{\partial n} dy, \tag{D.14}$$

which is equal to Equation 5.37.

Appendix E

The uncertainty quantification of the correlation for the bending angle β_w (Equation 5.54) is presented in this appendix. The dimensional tolerances of the rod and the wire are considered (see table 3.2), as well as the uncertainty on the measured mean angle β_w.
The uncertainty $\delta\beta_w$ on the value predicted by the correlation is expressed as

$$\delta\beta_w = \left| \frac{\partial \beta_w}{\partial b} \delta b \right|, \tag{E.1}$$

where δb is the uncertainty on the exponent of the correlation, and $\frac{\partial \beta}{\partial f}$ is obtained deriving Equation 5.54 with respect to b:

$$\frac{\partial \beta_w}{\partial b} = \frac{h}{\phi_{pin}} \frac{\ln\left(\frac{\phi_w}{\phi_h}\right) \cdot \left(\frac{\phi_w}{\phi_h}\right)^b}{1 + \left[\frac{h}{\phi_{pin}} \left(\frac{\phi_w}{\phi_h}\right)^b\right]^2}, \tag{E.2}$$

being h, ϕ_{pin}, and ϕ_w the helicoid wire pitch, the pin diameter and the wire diameter of an arbitrary hexagonal bundle. The dimensions of the SEEDS-2 bundle are substituted in the previous equation, that is h=h, ϕ_{pin}=D and ϕ_w=D_w.
The δb term is determined by the uncertainty propagation formula as

$$\delta b = \sqrt{\left(\frac{\partial b}{\partial D_w} \delta D_w\right)^2 + \left(\frac{\partial b}{\partial D} \delta D\right)^2 + \left(\frac{\partial b}{\partial \overline{\beta}} \delta \beta_w\right)^2}, \tag{E.3}$$

where δD_w, δD and $\delta\beta_w$ are respectively the uncertainties on the diameter of the rod and wire of the hexagonal bundle of this research, and β_w the mean measured angle of bending. The partial derivatives $\frac{\partial b}{\partial D_w}$, $\frac{\partial b}{\partial D}$ and $\frac{\partial b}{\partial \beta_w}$ are obtained by deriving Equation 5.56 with respect to D_w, D, and β_w:

$$\frac{\partial b}{\partial D_w} = \frac{\ln\left(\frac{D}{h} \tan\beta_w\right)}{\ln\left(D_w/D_h\right)^2} \cdot \left[-\frac{P + D_w}{P D_w} + \frac{4\sqrt{3}P - 2\pi D_w}{2\sqrt{3}P^2 - \pi\left(D^2 + D_w^2\right)} \right], \tag{E.4}$$

$$\frac{\partial b}{\partial D} = \frac{1}{D \ln\left(D_w/D_h\right)} + \frac{\ln\left(\frac{D}{h} \tan\beta_w\right)}{\ln\left(D_w/D_h\right)^2} \left[-\frac{1}{P} + \frac{4\sqrt{3}P - 2\pi D}{2\sqrt{3}P^2 - \pi\left(D^2 + D_w^2\right)} \right], \tag{E.5}$$

$$\frac{\partial b}{\partial \beta_w} = \frac{1}{\ln(D_w/D_h)} \frac{1+\tan^2\beta_w}{\tan\beta_w}. \tag{E.6}$$

Equation E.1 is finally used to estimate the uncertainty on the angle predicted by the correlation derived in Chapter 5, which is equal to 5%.

Acknowledgements

I would like to thank my promotors Jan Leen Kloosterman and Martin Rohde for trusting me, four and a half years ago, when I was given the opportunity to do the PhD in the RPNM section. In particular, thanks to Martin the discussions we had in our (few) periodic meeting: his ability to trigger new questions in me was inversely proportional to the time he could allocate in his agenda. And he has also proven a funny travel companion in our trip to China.
Thanks to the partners of the SESAME project for their support and for the fun we had together during the countless dinners together. A special thank goes to Afaque, Daniele, and Henri for the help during these four intensive years. Thanks to Ferry who, in the first year, gave me the name of a handbook of hydraulics (I. E. Idel'chik), which has proven extremely useful.
A big thank goes to Malte, Reinier, and Ernst from the workshop, and to the technicians, John and Dick, with whom I spent a lot of time in the lab, sometimes also for working.
I am grateful to Dick, who has proven also a valuable friend and mentor during these years.
Thanks to my colleagues in Delft, in particular Marco and Fahad for their support during my attempts at improving my inability at programming, and with whom I shared a big part of my non-professional life as well.

Thanks to my parents, Lucia e Franco, for the effort they have always put in my education, thereby paving the road towards the PhD.
Vorrei inoltre ringraziare i miei nonni, in particolare Renzo, per avermi insegnato che le cose che non funzionano, come gli esperimenti, sono le piu' interessanti.

Lastly, thank you Laura for your perseverance in supporting me, especially during the first three years when the distance between Delft and Groningen seemed too much for everybody, but not for you.

List of publications

Journal papers

F.Bertocchi, M. Rohde, J. L. Kloosterman, "LDA measurements of coherent flow structures and cross-flow across the gap of a compund channel with two half-rods". *Nuclear Engineering and Design* **326** (2018), pp. 17-30.

F.Bertocchi, M. Rohde, J. L. Kloosterman, "Experimental Investigation on the Influence of Gap Vortex Streets on Fluid-Structure Interactions in Hexagonal Bundle Geometries". *International Journal of Heat and Fluid Flow* **79** (2019).

H. Dolfen, **F.Bertocchi**, M. Rohde, J. Degroote, "Vibrations in a 7-rod bundle subject to axial flow: Simulations and experiments". *Nuclear Engineering and Design* **353** (2019).

F. Roelofs, H. Doolaard, D. Dovizio, B. Mikuz, A. Shams, **F.Bertocchi**, M. Rohde, J. Pacio, I. Di Piazza, G. Kennedy, K. Van Tichelen, A. Obabko, E. Merzari, "Towards validated prediction with RANS CFD of flow and heat transport in a wire-wrapped fuel assembly". *Nuclear Engineering and Design* **353** (2019).

F.Bertocchi, M. Rohde, J. L. Kloosterman, "Understanding migratory flow caused by helicoid wire spacers in rod bundles: an experimental and theoretical study" (2019). *International Journal of Heat and Fluid Flow* **80** (2019).

F.Bertocchi, M. Rohde, D. De Santis, A. Shams, H. Dolfen, J. Degroote, J. Vierendeels, "Fluid-Structure Interaction of a 7-rods bundle: benchmarking numerical simulations with experimental data". *Nuclear Engineering and Design* **356** (2020).

Book chapters

M. Rohde, P. Planquart, C. Spaccapaniccia, **F.Bertocchi**, "Rod bundle and pool-type experiments in water serving liquid metal reactors". In: *Thermal Hydraulic Aspects of Liquid Metal Cooled Reactors*. Ed. by F. Roelofs. Woodhead Publishing Series in Energy, Elsevier. Ch. 3.1, pp. 49-82 (2019).

Conference papers

F.Bertocchi, M. Rohde, J. L. Kloosterman, "Experimental Study of the Onset Conditions for Cross-flow through the Gap between two Half Rods". In: *Proc. 17th International Topical Meeting on Nuclear Reactor Thermal Hydraulics* (NURETH 17). Xi'An, China (2017).

H. Dolfen, **F**.**Bertocchi**, M. Rohde, J. Vierendeels, J. Degroote, "Investigation of the gap vortex streets in densely packed tube arrays in axial flow using CFD and experiments". In: *Proc. 6th European Conference on Computational Mechanics* (ECCM 6) *7th European Conference on Computational Fluid Dynamics* (ECFD 7). Glasgow, UK (2018).

H. Dolfen, **F**.**Bertocchi**, M. Rohde, J. Vierendeels, J. Degroote, "Numerical investigation of vortex-induced vibrations of a bundle of cylinders in axial flow". In: *Proc. 9th International Symposium on Fluid – Structure Interactions Flow – Induced Vibrations & Noise* (FIV 2018). Toronto, Canada (2018).

H. Dolfen, **F**.**Bertocchi**, M. Rohde, J. Degroote, "Numerical simulations of vortex-induced vibrations in a 7-rod bundle compared to experimental data". *SESAME International Workshop*. Petten, The Netherlands (2019).

F.**Bertocchi**, M. Rohde, D. De Santis, A. Shams, H. Dolfen, J. Degroote, J. Vierendeels, "Fluid-Structure Interaction of a 7-rods bundle: benchmarking numerical simulations with experimental data". *SESAME International Workshop*. Petten, The Netherlands (2019).

F. Roelofs, H. Doolaard, D. Dovizio, B. Mikuz, A. Shams, **F**.**Bertocchi**, M. Rohde, J. Pacio, I. Di Piazza, G. Kennedy, K. Van Tichelen, A. Obabko, E. Merzari, "Towards validated prediction with RANS CFD of flow and heat transport in a wire-wrapped fuel assembly". *SESAME International Workshop*. Petten, The Netherlands (2019).

H. Dolfen, **F**.**Bertocchi**, M. Rohde, J. Degroote, "Fluid-Structure Interaction Simulations of the Vibrations of a Bundle of 7 Rods Induced by a Gap Vortex Street". In *Proc. 8th International Conference on Coupled Problems in Science and Engineering* (COUPLED 2019). Sitges, Spain (2019).

F. Roelofs, H. Dolaard, B. Mikuz, D. Dovizio, D. De Santis, A. Shams, **F**.**Bertocchi**, M. Rohde, K. Van Tichelen, S. Keijers, G. Kennedy, A. Batta, J. Pacio, P. Planquart, A. Obabko, L. Brockmeyer, E. Merzari, R. Vaghetto, Y. Hassan, D. Leonard, M. Martin, B. Jackson, M. Steer, M. Delchini, D. Pointer, "CFD and Experiments for Wire-wrapped Fuel Assemblies". In: *Proc. 18th International Topical Meeting on Nuclear Reactor Thermal Hydraulics* (NURETH 18). Portland, US (2019).

F.**Bertocchi**, M. Rohde, J. L. Kloosterman, "PIV measurements inside a wire-wrapped hexagonal rod bundle: from experiments to governing equations". In: *Proc. 18th International Topical Meeting on Nuclear Reactor Thermal Hydraulics* (NURETH 18). Portland, US (2019).

About the author

The author was born in Pisa (Italy) on 4$^{\text{th}}$ November, 1990 (although he prefers to regard Livorno as his native town). He finished his high school studies at Liceo Scientifico U. Dini in 2009. The same year he enrolled in the bachelor degree on Nuclear Engineering, Safety and Protection at the University of Pisa where he graduated on 4$^{\text{th}}$ March, 2013 with the thesis "Analysis of the structural response of a nuclear waste disposal during the impact of a commercial Boeing-747 aircraft". He continued the studies at the same university with the master degree on Nuclear Engineering. Between 2014 and 2015 he moved to SCK-CEN nuclear research centre (Mol, Belgium) where he did his master thesis project with title "CFD study of Polonium evaporation from LBE liquid mixture". He obtained his master degree on 20$^{\text{th}}$ July, 2015 and in September he became a PhD candidate on fluid-mechanics in the group of prof. Jan Leen Kloosterman, at Delft University of Technology. In October 2019 he was hired as consultant by the Licensing Team of the Nuclear Research and consultancy Group (NRG) in Arnhem.